# Defect Equilibria and Electrode Kinetics in $Pr_xCe_{1-x}O_{2-\delta}$ Mixed Conducting Thin Films: An *in-situ* Optical and Electrochemical Investigation

by

Jae Jin Kim

B.S. Materials Science and Engineering
Seoul National University, 2006

M.S. Materials Science and Engineering
Seoul National University, 2008
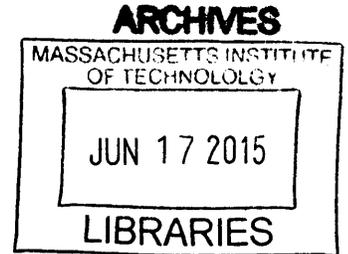
SUBMITTED TO THE DEPARTMENT OF MATERIALS SCIENCE AND ENGINEERING
IN PARTIAL FULFILLMENT OF THE REQUIREMENTS FOR THE DEGREE OF

DOCTOR OF PHILOSOPHY
IN MATERIALS SCIENCE AND ENGINEERING

AT THE
MASSACHUSETTS INSTITUTE OF TECHNOLOGY

JUNE 2015

Authored by **Signature redacted**

Jae Jin Kim
Department of Materials Science and Engineering
May 08, 2015

Certified by **Signature redacted**

Harry L. Tuller
Professor of Ceramics and Electronic Materials
Thesis Supervisor

Accepted by **Signature redacted**

Donald R. Sadoway
Chair, Departmental Committee on Graduate Students

1

Defect Equilibria and Electrode Kinetics in $Pr_xCe_{1-x}O_{2-\delta}$ Mixed Conducting
Thin Films: An *in-situ* Optical and Electrochemical Investigation
by
Jae Jin Kim

Submitted to the Department of Materials Science and Engineering
On May 08, 2015
in Partial Fulfillment of the Requirements for the Degree of
Doctor of Philosophy in Materials Science and Engineering

## ABSTRACT

An improved fundamental understanding of oxygen defect equilibria and transport kinetics in oxides is essential for achieving enhanced performance and longevity in many oxide-based practical applications. The ability to diagnose a material's behavior in a thin film structure under operating conditions (*in operando*), ideally *in situ*, is therefore of importance.

In this dissertation, a novel experimental technique capable of simultaneously performing *in situ* and *in operando* optical absorption and electrochemical impedance spectroscopy (EIS) measurements was developed and utilized, *for the first time*, over a range of temperatures and controlled atmospheres. The technique was applied to the $Pr_xCe_{1-x}O_{2-\delta}$ (PCO) model thin film system. PCO shows mixed ionic and electronic conducting (MIEC) characteristics at relatively high $pO_2$ regimes (e.g. air), which is beneficial for solid oxide fuel cells (SOFCs) cathode performance. The Pr impurity levels in PCO allow for optical transitions (2.0 – 3.3 eV), leading to the red coloration of oxidized samples. A change in the redox state of Pr results in a color change and so serves as a means of investigating the Pr oxidation state and thereby oxygen non-stoichiometry. $Pr^{4+}$ concentrations, derived independently from optical and electrochemical measurements, and their corresponding trends, were found to be self-consistent, confirming that the oxygen reduction enthalpy in thin film 10PCO is lower than that in the bulk. The derived extinction coefficient, $\varepsilon_{Pr^{4+}} = 6.37 \pm 0.05 \times 10^{-18}$ cm$^2$, can now be utilized to study defect equilibria of PCO or other relevant oxide films by optical means alone. The oxygen surface exchange reaction kinetics, driven by chemical and electrical driving forces, were investigated and correlated to each other, with the aid of the thermodynamic factor. The impact of surface chemistry and metal current collector on the reaction kinetics was discussed.

A specially designed cell structure enabled the extension of the oxygen diffusion pathway, allowing for the monitoring of color front migration in PCO films. Such optical color front motion experiments offer the opportunity for *in situ*, more rapid and reversible investigation of oxygen diffusion kinetics in thin films and open new opportunities to study materials' spatially distinguishable properties.

Thesis Supervisor: Harry L. Tuller

Title: Professor of Ceramics and Electronic Materials

# TABLE OF CONTENTS

5

# LIST OF PUBLICATIONS

*Thesis topic related publications*

Jae Jin Kim, S. R. Bishop, N. Thompson, D. Chen, H. L. Tuller, "*Investigation of nonstoichiometry in oxide thin films by simultaneous in situ optical absorption and chemical capacitance measurement: Pr doped ceria – case study*", Chem. Mater., 26, 1374-1379 (2014).

Jae Jin Kim, S. R. Bishop, N. J. Thompson, H. L. Tuller, "*Investigation of redox kinetics by simultaneous in situ optical absorption relaxation and electrode impedance measurements: Pr doped ceria thin films*", ECS Trans., 57, 1979-1984 (2013).

S. R. Bishop, J. Druce, Jae Jin Kim, J. Kilner, H. L. Tuller, "*Observation of surface impurities in $Pr0.1Ce0.9O2-\delta$ thin films following optical absorption relaxation measurements*", ECS Trans., 50, 35-38 (2013).

Jae Jin Kim, S. R. Bishop, N. Thompson, Y. Kuru, H. L. Tuller, "*Optically derived energy band gap states of Pr in ceria*", Solid State Ionics, 225, 198-200 (2012).

H. L. Tuller, S. R. Bishop, D. Chen, Y. Kuru, Jae Jin Kim, T. S. Stefanik, "*Praseodymium doped ceria: model mixed ionic electronic conductor with coupled electrical, optical, mechanical and chemical properties*", Solid State Ionics, 225, 194-197 (2012).

S. R. Bishop, Jae Jin Kim, N. Thompson, H. L. Tuller, "*Probing redox kinetics in Pr doped ceria mixed ionic electronic conducting thin films by in-situ optical absorption measurements*", ECS Trans., 45, 491-495 (2012).

S. R. Bishop, Jae Jin Kim, N. Thompson, H. L. Tuller, "*Defect chemistry and electrical properties of a $Pr-CeO_2$ solid solution: From nano- to micro-scale*", Mater. Res. Soc. Symp. Proc., Vol. 1331, DOI: 10.1557/opl.2011, (2011).

S. R. Bishop, Jae Jin Kim, N. Thompson, D. Chen, Y. Kuru, T. Stefanik, H. L. Tuller, "*Mechanical, electrical, and optical properties of $(Pr,Ce)O_2$ solid solutions: kinetic studies*", ECS Trans., 35, 1137-1144 (2011).

S. R. Bishop, D. Chen, Y. Kuru, Jae Jin Kim, T. S. Stefanik, H. L. Tuller, "*Measurement and modeling of electrical, mechanical, and chemical properties of a model mixed ionic electronic conductor: Pr doped Ceria*", ECS Trans., 33, 51 (2011).

*Other publications*

D. H. Kim, X. Y. Sun, N. M. Aimon, <u>Jae Jin Kim</u>, M. J. Campion, H. L. Tuller, L. Kornblum, F. J. Walker, C. H. Ahn, C. A. Ross, "*A three component self-assembled epitaxial nanocomposite thin film*", Adv. Funct. Mater., accepted. DOI: 10.1002/adfm.201500332 (2015).

N. H. Perry, <u>Jae Jin Kim</u>, S. R. Bishop, H. L. Tuller, "*Strongly coupled thermal and chemical expansion in the perovskite oxide system $Sr(Ti,Fe)O_{3-\alpha}$*", J. Mater. Chem. A., 3, 3602-3611 (2015).

W. Ma, <u>Jae Jin Kim</u>, N. Tsvetkov, T. Daio, Y. Kuru, Z. Cai, Y. Chen, K. Sasaki, H. L. Tuller, B. Yildiz, "*Vertically aligned nanocomposite $La_{0.8}Sr_{0.2}CoO_3/(La_{0.5}Sr_{0.5})_2CoO_4$ cathodes - electronic structure, surface chemistry and oxygen reduction kinetics*", J. Mater. Chem. A., 3, 207-219 (2015).

S. R. Bishop, D. Chen, J. Sheth, S. T. Misture, B. W. Sheldon, <u>Jae Jin Kim</u>, H. L. Tuller, "*Impact of size scale on electro-chemo-mechanical coupling properties in MIECs: Bulk and thin film $(Pr,Ce)O_{2-\delta}$*", ECS Trans., 61, 31-36 (2014).

W. C. Jung, <u>Jae Jin Kim</u>, H. L. Tuller, "*Fabrication of nanoporous Pt thin films: application as micro-SOFC electrodes*", <u>equal contribution</u>, J. Power. Sources, 275, 860-865 (2014).

Y. Zhang, <u>Jae Jin Kim</u>, D. Chen, H. L. Tuller, G. C. Rutledge, "*Electrospun polyaniline fibers as chemiresistive sensors for ammonia and nitrogen dioxide gases*", Adv. Funct. Mater., 24, 4005-4014 (2014).

J. Swallow, W. Woodford, Y. Chen, Q. Lu, <u>Jae Jin Kim</u>, D. Chen, Y. M. Chiang, W. C. Carter, B. Yildiz, H. L. Tuller, K. J. Van Vliet, "*Chemomechanics of ionically conductive ceramics for electrical energy conversion and storage*", Special Issue on Electrochemomechanics. J. Electroceram., 32, 3-27 (2014).

<u>Jae Jin Kim</u>, M. Kuhn, S. R. Bishop, H. L. Tuller, "*Cathodic and defect properties of $Ba_xSr_{1-x}Ti_{1-y}Fe_yO_{3-y/2+\delta}$ mixed conducting oxides*", Solid State Ionics, 230, 2-6 (2013).

M. Kuhn, <u>Jae Jin Kim</u>, S. R. Bishop, H. L. Tuller, "*Oxygen nonstoichiometry and defect chemistry of perovskite-structured $Ba_xSr_{1-x}Ti_{1-y}Fe_yO_{3-y/2+\delta}$ solid solutions*", Chem. Mater., 25, 2970-2975 (2013).

Y. Chen, W. C. Jung, Z. Cai, <u>Jae Jin Kim</u>, H. L. Tuller, B. Yildiz, "*Impact of Sr segregation on the electronic structure and oxygen reduction activity of $SrTi_{1-x}Fe_xO_3$ surfaces*", Energy Environ. Sci., 5, 7979-7988 (2012).

Y. Kuru, S. R. Bishop, <u>Jae Jin Kim</u>, B. Yildiz, H. L. Tuller, "*Chemomechanical properties and microstructural stability of nanocrystalline Pr-doped ceria: an in situ X-ray diffraction investigation*", Solid State Ionics, 193, 1-4 (2011).

Y. Kuru, S. R. Bishop, <u>Jae Jin Kim</u>, B. Yildiz, H. L. Tuller, "*Chemical Expansion and Frozen-in Oxygen Vacancies in Pr-doped ceria*", ECS Trans., 35, 1131 (2011).

# LIST OF FIGURES

11

14

# LIST OF TABLES

# ACKNOWLEDGEMENTS

As I complete my PhD study, I thankfully would like to acknowledge all individuals who have been given around me as great blessing.

First of all, it was my great honor to have Prof. Harry Tuller as my doctoral advisor. Through the past six years, I was blessed to experience his respectable philosophy of advising. He did not just convey his deep knowledge and insight of the field, but he led me to learn the way of thinking and rationalizing by giving questions and waiting for my answers with great patience. He has also repeatedly proven true concern for my personal life and professional development. It is through his advice and support that the research described in this thesis and my growth as a scientist were possible. I thankfully acknowledge the other members of my thesis committee, Prof. Caroline Ross, Prof. Jeffrey Grossman and Prof. Krystyn Van Vliet, for giving their time and constructive suggestion. Especially, I would like to express my gratitude to Prof. Van Vliet for the close collaboration in many projects relating to the interesting research topic, chemomechanics, and for her kind financial support for the last term.

I would like to thank my officemates and colleagues in the extended Tuller group: Di Chen, Johanna Engel, George Whitfield, Nicholas Thompson, Michael Campion, Changsub Kim, Nicola Perry, Melanie Kuhn, Kiran Adepalli, Dario Marrocchelli, Kunal Muhkerjee, Elisabeth Anderson, Dae Jin Yang, Anderson André Felix, Pedro Henrique Suman, Yener Kuru and Pyeong Seok Cho. They have shared their knowledge and experience and supported me in completing this work. Especially, I sincerely thank Sean Bishop and Woochul Jung for teaching me many important technical skills and advising me kindly in spite of my never-ceasing questions and demanding for their help. I am also indebted to Stuart Cook and Nikolai Tsvetkov for their ideas, techniques and analysis that have contributed towards piecing together this work. I also would like to thank Wen Ma, Yan Chen, Jessica Swallow, Prof. Bilge Yildiz for the close collaboration in the various projects.

My time on MIT has become bountiful, lively and peaceful with friends from Graduate Christian Fellowship (GCF), Cambridge Korean Presbyterian Church (CKPC), Citylife Church, Korean Graduate in DMSE, basketball team, swimming club and MIT choir. They gave me unforgettable memories and supported me during the past six years of up-and-downs.

I would like to express my respect and love to my parents and family members for their tireless and ceaseless support and love. I also thank my lovely daughter, Siyeon, for giving me endless source of motivation and joy.

I especially want to give my deep and sincere love and gratitude to my lovely wife, Hyunsoo, for her infinite understanding and encouragement. I am blessed to have her as a best friend and lifelong companion.

Finally, I want to give thanks to my God, my heavenly Father. "*Do not be terrified; do not be afraid of them. The LORD your God, who is going before you, will fight for you, as he did for you in Egypt, before your very eyes, and in the desert. There you saw how the LORD your God carried you, as a father carries his son, all the way you went until you reached this place.*" (Deuteronomy 1:29-31)

May 8th, 2015
Jae Jin Kim

17

# CHAPTER 1. INTRODUCTION

## 1.1 Motivation

The world's strong dependence on fossil fuels for its energy needs has seriously impacted the environment and quality of life. Combustion of coal, petroleum and natural gas is a major source of pollutants that contributes to the greenhouse effect, acid rain and health problems. Furthermore, fossil fuels are non-renewable, and therefore methods must be found which limit their use in the near future. As a consequence, new technologies for producing, storing and using renewable and environment-friendly energy sources are required.

Fuel cells are electrochemical devices that convert chemical energy directly into electrical energy with higher efficiency and lower emissions than conventional energy systems [1]. Contrary to batteries, fuel cells are not energy storage devices, but electrical generators by the electrochemical oxidation of the fuel and electrochemical reduction of the oxidant. The energy conversion process continues as long as the fuel and oxidant are provided to the system. There are a variety of fuel cell technologies, distinguished by materials utilized and their corresponding ion transport mechanisms, operating temperatures and fuels availability (Figure 1). Fuel cells are also attractive for their modular and distributed nature, and quiet operation [2]. The potential fuel cell applications ranges from battery replacement in small portable electronic devices, main or auxiliary power units in transportation, residential combined heat and power (CHP) units, to megawatt (MW) scale electrical power generation [3–7]. After the tragedy related to the nuclear power plants in Japan, large-scale distributed application of fuel cells has attracted more interest as an uninterrupted and safe power source for remote and stand-alone applications such as information technology companies, hospitals and airports.

| Interconnect / fuels | Graphite Carbon composite or metallic | | Graphite | Metallic | Cr or Ni alloys Lanthanum chromites |
|---|---|---|---|---|---|
| | $H_2$ only | $H_2$, $CH_3OH$ | $H_2$, External reformate | $H_2$, CO $CH_4$ | $H_2$, CO $CH_4$ |
| Anode | Pt, Ni | Pt | Pt | Ni alloy | Ni cermet |
| Electrolyte | Alkaline $OH^-$ | Polymer $H^+$ | Phosphoric Acid $H^+$ | Molten Carbonate $CO_3^{2-}$ | Solid Oxide $O^{2-}$ |
| Cathode | Ni | Pt | Pt | NiO | Lanthanum based compounds |
| Temperature | ~70°C | <80°C | ~200°C | ~650°C | (HT) 750-1000°C (IT-SOFC) 500----------750°C |

**Figure 1. Summary of the different types of fuel cells, including temperature of operation and material used. Reprinted from a reference [5].**

## 1.2 Solid oxide fuel cells (SOFCs)

### 1.2.1 Principles of operation and characteristics

Among the various types of fuel cells, solid oxide fuel cells (SOFCs) have received much attention due to several distinct advantages. The use of an oxide electrolyte provides chemical, thermal and mechanical stability compared to polymer based electrolytes and eliminates the corrosive and containment problems associated with liquid electrolytes. As a consequence, in certain modes of operation, SOFCs have demonstrated the longest lifetime among fuel cell systems. For example, a 100 kW SOFC cells fabricated by Siemens-Westinghouse has successfully produced power for more than 20,000 h with minimal degradation in performance [8]. Oxygen ion conduction in oxide electrolyte is thermally activated, and its magnitudes only approach that of liquid electrolytes at high temperatures (>800 °C). Therefore, the operation of SOFCs has, in the past, been limited to the high temperature range between 800 °C and 1000 °C, which has both advantages and disadvantages. In this temperature region, C-C bonds break easily and thus some hydrocarbons can be directly utilized at the anode [9]. In this way, SOFCs provide flexibility of fuel choice, allowing a variety of hydrocarbons fuels such as natural gas to be utilized. Furthermore, high temperature operation ensures fast transport and electrochemical reaction kinetics, thus minimizing the irreversible losses due to electrode kinetics and ohmic resistances. Therefore, high temperature SOFCs generally provide the highest conversion efficiency compared to the other types of fuel cells [10].

20
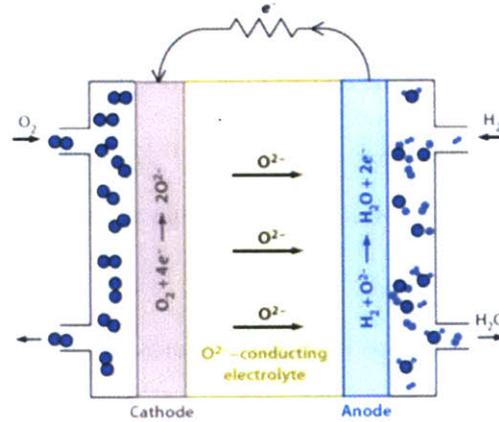
**Figure 2. Schematic diagram of a solid oxide fuel cell (SOFC) showing the oxygen ion conducting electrolyte, the electrodes and electrode reactions, and the direction of electron and ion flow. Reprinted from a reference [11].**

The fundamental building block of SOFCs is an electrochemical cell, which consists of two electrodes separated by an ionic conducting electrolyte (e.g. oxygen ion conductor). The first reported fuel cell using a ceramic oxide electrolyte was developed by Baur and Preis in 1937 [12]. The operation of SOFCs, including half-cell reactions, is summarized in Figure 2. A fuel such as hydrogen or hydrocarbon ($C_mH_n$) gas is directed to the anode and an oxidant, typically oxygen, to the cathode. At the cathode side, oxygen in the oxidant is reduced to the oxygen ion ($O^{2-}$), with electrons provided from the interconnect, which is then incorporated into the electrolyte. The electrolyte serves as a barrier to gas diffusion, but permits oxygen ions to migrate towards the anode side, preventing direct chemical combustion. At the anode side, oxygen ions react with the fuel to form water and, if there are carbon-containing fuels, carbon dioxide. During this oxidation reaction, electrons are released and travel through the external load [2]. The driving force for the overall cell reaction (Equation (1)) is the chemical potential difference of oxygen between two electrodes. This can be expressed by the Nernst equation using oxygen partial pressures (Equation (2)).

$$H_2 + \frac{1}{2} O_2 \leftrightarrow H_2O \tag{1}$$

$$E_{eq} = \frac{RT}{nF} \ln \frac{pO_2 \ (at \ cathode)}{pO_2 \ (at \ anode)} = V_{oc} \tag{2}$$

21

where $E_{eq}$ is the equilibrium voltage (or Nernst voltage) at standard pressure (1 atm) at a specific operating temperature, $R$ is the gas constant, $T$ is the temperature, $n$ (=4) is the number of electrons transferred, $F$ is Faraday's constant (96,500 C/mol), and $pO_2$ is the partial pressure of oxygen. Theoretically, $E_{eq}$ is the same as the open circuit voltage, $V_{OC}$, which is the voltage when no current flows through the external circuit.

In reality, $V_{OC}$ decreases by leakage mechanisms across the electrolyte, which originate from poor sealing, cracks along the electrolyte, or partial electronic conduction. Also, the various polarization mechanisms lead to the decrease of $V_{OC}$, the magnitude of which is proportional to the amount of flowing current. Therefore, the voltage output, $V_{operating}$, is equal to the ideal Nernst potential minus the total loss.

$$V_{operating} = V_{OC} - V_L - \eta_{tot} = V_{OC} - V_L - (\eta_{act} + \eta_{ohm} + \eta_{diff}) \qquad (3)$$

where $V_L$ is the loss in the voltage due to leaks across the electrolyte, $\eta_{act}$ is the activation overpotential due to slow electrode reactions, $\eta_{ohm}$ is the overpotential due to ohmic resistances in the cell, and $\eta_{diff}$ is the overpotential due to mass diffusion limitations [13].

A common way of displaying the performance of a fuel cell is by plotting the voltage and the output power density ($P = V \cdot I$) against the current density, as in Figure 3. At specific operation point, in general, one of the polarization mechanisms becomes the dominant process. Typical performance curves like Figure 3 can often be identified by concave up, linear, and concave down curvature of the activation, ohmic, and concentration polarization dominant regions, respectively. The power output goes through a roughly parabolic curve giving maximal power output ($P_{max}$) at certain operation point because the voltage decreases monotonically as the current increases.
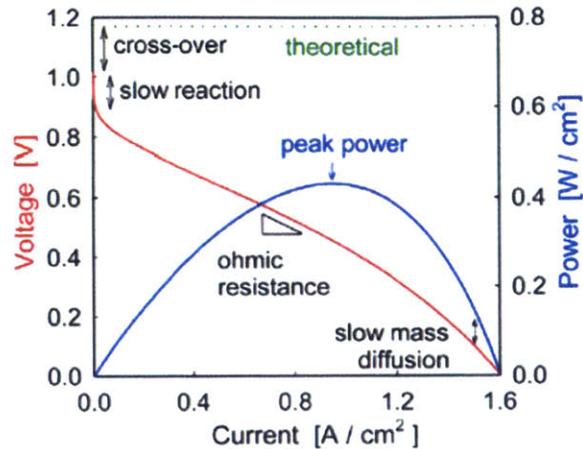
**Figure 3. Schematic fuel cell polarization (voltage vs. current density) and power density curves. Reprinted from a reference [2].**

### 1.2.2 Technical challenges of SOFCs

Even though high operating temperatures offer several advantages as indicated above, they also contribute to degradation problems related to accelerated reactions between adjacent cell components and sealing difficulties. These drawbacks contribute to higher cost and reduced lifetimes of SOFC systems [10]. As a consequence, significant efforts have been devoted to the development of intermediate temperature (500 - 700 °C) SOFCs (IT-SOFCs). The system cost can be significantly reduced by lowering the operating temperature because less expensive materials in interconnects and heat exchangers can be utilized. For instance, when the operating temperature is decreased to below 600 °C, low-cost metallic materials such as ferritic stainless-steels can be utilized for the interconnect and construction materials. This allows both the stack and balance-of-plant to be cheaper and more robust. In addition, lower temperature operation affords more rapid start-up and shut-down and reduced corrosion rates of metallic components. Lower operation temperatures also increase the durability of SOFC systems by reducing performance degradation due to interdiffusion or reaction between individual components.

However, because transport processes in the electrolyte and the electrode kinetics are mostly thermally activated, operation at lower temperature creates a number of materials problems that are associated with the increase in the electrolyte resistance and in the electrode polarization. Both factors

23

cause a reduction of the cell voltage and the output power. There are two main approaches to achieve lower operation temperature, while still obtaining comparable performance to the higher temperature operation. One is decreasing the thickness of the electrolyte so that the area specific resistance (ASR) of the system can be reduced. For example, decreasing the conventional yttria stabilized zirconia (YSZ) electrolyte thickness based on MEMS techniques has recently been applied towards accommodating very thin-film electrolytes [14]. Another is developing new materials systems with enhanced characteristics at lower temperature, in other words, finding alternative electrolyte materials with higher ionic conductivity and electrode materials with minimized polarization resistance at lower operating temperatures. Cathode materials, in particular, have been receiving a great deal of attention given that oxygen incorporation at the cathode is often considered as the key factor limiting performance of IT-SOFCs [15].

*1.2.3 The cathode in SOFCs*

<u>Cathode Reactions</u>

The oxygen reduction reaction at the cathode can be written as follows: (see also Figure 2)

$$O_{2(g)} + 4\,e' + 2\,V_O^{\cdot\cdot} \rightarrow 2\,O_O^X \tag{4}$$

where $V_O^{\cdot\cdot}$ is a doubly positive charged oxygen vacancy, $e'$ is an electron and $O_O^X$ represents an oxygen ion in the cathode or electrolyte lattice. The overall reaction comprises a number of steps such as chemisorption, dissociation, diffusion and incorporation into oxygen vacancies. In general, one may distinguish three possible paths for the cathodic reaction, that is, the electrode surface path, the bulk path and the electrolyte surface path (See Figure 4) [16]. Oxygen gas molecules adsorb on the surface of either the electrode or the electrolyte and diffuse to a "three phase boundary" (TPB) where gas phase, electrode and electrolyte are in contact. At this electrochemically active region, oxygen is incorporated as $O^{2-}$ ion into oxygen vacancy site of the electrolyte lattice. If electrons could be provided by the electrolyte or ionized oxygen species could diffuse along the electrolyte surface, the incorporation zone would be broadened.

*electrode surface path*    *bulk path*    *electrolyte surface path*
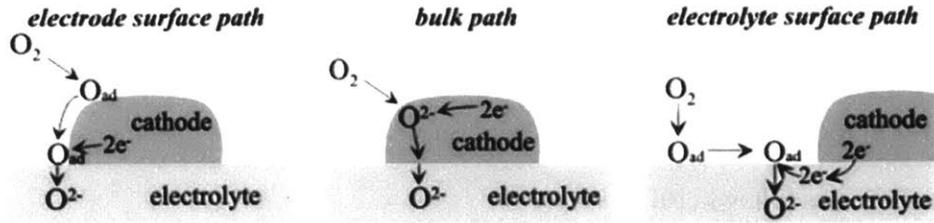
**Figure 4. Sketches of the three reaction paths of the oxygen reduction and incorporation reaction and some possible rate-determining steps. Modification of the paths (e.g., adsorption of a molecular rather than an atomic species or diffusion along the cathode/electrolyte interface) and a combination of electrode and electrolyte surface paths (adsorption on cathode and surface diffusion onto the electrolyte surface) are also possible. Reprinted from a reference [16].**

The bulk pathway becomes possible only if the electrode material itself is an oxide ion conductor in addition to supplying electrons. In this case of a mixed ionic and electronic conducting (MIEC) electrode, oxygen incorporation is not restricted to the TPB zone, but the whole surface of the electrode can be active to the reaction. The incorporated $O^{2-}$ ions then diffuse through the bulk of the electrode material towards the interface between electrode and electrolyte, followed by ion transfer across this interface. In other words, the generation and transport of oxygen ions are associated with the electrode polarization. Therefore, in order to optimize the structure and the composition of electrodes for good performance at lower operation temperature, the oxygen surface exchange rate ($k$) and the oxygen chemical diffusion coefficient ($D_{chem}$) must be considered. The characteristic resistance, $R_{chem}$, describing the chemical contributions to the cell impedance is introduced by the Adler/Lane/Steele (ALS) model as shown in Equation (5) [17].

$$R_{chem} = \frac{RT}{2F^2} \sqrt{\frac{\tau}{(1 - \varepsilon)a\, C_0^2\, D_{chem}\, k}} \tag{5}$$

where $\tau$, $\varepsilon$, and $a$ are tortuosity, fractional porosity, and internal surface area/unit volume, respectively, $C_0$ is the surface concentration of oxygen.

Reducing the operation temperature leads to significant challenges in materials selection, especially for the cathode material, given the high activation energy (often > 1.5 eV) of the oxygen reduction reaction [16]. The critical requirements for enhanced performance and long-term operation of the SOFC cathode can be summarized as follows [10]:

(1) High electronic conductivity

(2) High oxygen ionic conductivity for MIEC materials

(3) High electrocatalytic activity for the oxygen reduction reaction

(4) Porosity to facilitate transport of the oxygen to the cathode/electrolyte interface

(5) Chemical compatibility with neighboring cell components (primarily the electrolyte)

(6) Chemical stability – no phase changes during operation

(7) Dimensional stability – thermal/chemical expansion coefficient (TEC/CEC) comparable to that of the electrolyte and stable porosity

Noble metals or electronically conducting oxides can be utilized as cathode materials, because they are chemically stable at the high SOFC operating temperature. However, noble metals such as platinum are too expensive for practical application, while silver is too mobile at high temperatures. Therefore, a great deal of effort has been directed towards developing transition-metal oxides as SOFC cathodes materials. Materials investigated in detail during recent decades include $La_{1-x}Sr_xMnO_{3-\delta}$ (LSM), $La_{1-x}Sr_xFeO_{3-\delta}$ (LSF), $La_{1-x}Sr_xCoO_{3-\delta}$ (LSC), $La_{1-x}Sr_xCo_{1-y}Fe_yO_{3-\delta}$ (LSCF), $Ba_{1-x}Sr_xCo_{1-y}Fe_yO_{3-\delta}$ (BSCF), etc.

LSM shows high electronic conductivity (200 – 300 S/cm at 900 °C) and well-matched TEC with that of YSZ [18]. While it exhibits high catalytic activity for oxygen reduction only at relatively high temperatures (> 800 °C), it suffers from the formation of undesired reaction products such as $La_2Zr_2O_7$ with YSZ at those high temperatures [19]. Furthermore, the very low ionic conductivity ($10^{-7}$ S/cm at 900 °C) of LSM causes the oxygen reduction reaction to be restricted to the TPB region, leading to slow

electrode kinetics. Therefore, many efforts have been focused on increasing the active TPB regions by adopting porous electrodes or composite structures with materials exhibiting high ionic conductivities.

Instead of combining an electronic and ionic conductor, a single-phase MIEC material can be considered as an alternative strategy towards the application to IT-SOFCs. As discussed above, MIEC electrodes in SOFCs can utilize the entire electrode surface for the reduction of oxygen as opposed to only the TPB region, thereby increasing the area of the active reaction sites and improving the kinetics at lower temperatures than 700 °C. In this context, there have been many research efforts to develop MIEC cathode materials by replacing Mn with other elements such as Co and Fe. LSF, LSC, and LSCF fall into this group of materials. Introducing iron seems to provide promising electrocatalytic properties to LSF electrodes, enhancing oxygen diffusion and surface exchange processes [20]. The LSC electrodes show excellent electronic conductivity up to 1,600 S/cm at 800 °C [21]. However, these materials tend to react with YSZ and their TECs do not match with that of YSZ. Therefore, ceria-based electrolytes must be used, or buffer layers, such as ceria or $(La,Sr)(Ga,Mg)O_3$, between the electrode and the YSZ electrolyte are needed [22]. In order to adjust the TEC and increase the chemical stability of LSC cathodes, LSCF is now being highly investigated [23]. LSCF has a total conductivity of 230 S/cm at 900 °C, while the oxygen ionic conductivity is about 0.2 S/cm [24]. However, increasing substitution of Fe for Co results in reduced electronic conduction.

BSCF has recently received special attention as a SOFC cathode material [25]. Barium was initially introduced into $SrCo_{1-x}Fe_xO_{3-\delta}$ (SCF), a potential oxygen permeation membrane, to suppress the phase transformation from cubic perovskite into the vacancy-ordered Brown-millerite phase at reduced temperature and low oxygen partial pressure [26]. BSCF materials show excellent oxygen surface exchange and diffusion properties. However, BSCF reacts with the widely used electrolytes such as YSZ or GDC ($Gd_{1-x}Ce_xO_{2-\delta}$). Also, it exhibits sensitivity to $CO_2$ by forming carbonate surface layers as well as a gradual phase transformation into an hexagonal perovskite phase between 850 and 900 °C [27,28].

## 1.3 Oxygen nonstoichiometry and transport kinetics in oxide materials

After examining the required characteristics for SOFC cathode materials, as listed above, one concludes that a fundamental understanding of both oxygen nonstoichiometry and transport kinetics is essential when attempting to design and develop highly performing MIEC cathode materials. For example, the ionic conductivity is dependent on both the charged oxygen defect concentration and migration behavior, while electrons generated during oxygen defect generation by reduction contribute to enhanced electronic conductivity. Furthermore, this same process leads to valency changes in the transition metal or rare earth ions within the MIEC materials, and corresponding changes in lattice constant (chemical expansion). This may lead to stresses sufficient to support crack initiation and/or delamination, impacting the device's long term stability. Furthermore, under the operating conditions of these devices, i.e. elevated temperatures and oxygen partial pressures ranging from highly oxidizing to highly reducing, device properties and performance are inevitably impacted by these thermodynamic and kinetic properties. The ability to diagnose a material's behavior under operating conditions (*in operando*), ideally *in situ*, is therefore of importance.

The diffusion coefficient ($D$) and surface exchange coefficient ($k$) are parameters that quantify the rate of the bulk and surface reactions, respectively. Both parameters can be understood based on the relationship between the flux of the species ($j$) and the driving force that causes the flux. The driving force, for example, is reflected in the chemical potential gradient of the diffusing species. The diffusion coefficient ($D$) is defined as the proportionality constant between the diffusion flux and the negative gradient in chemical activity or concentration in Fick's first law (Equation (6)). On the other hand, the surface exchange coefficient ($k$) is defined as the constant of proportionality between the surface reaction flux and the perturbation of the diffusing species' concentration (Equation (7)).

$$j_O = -D_O \frac{\partial C_O}{\partial x} \tag{6}$$

$$j_O = -k_O(C_{O,atmosphere} - C_{O,surface}) \tag{7}$$

There are three fundamental experimental techniques for studying oxygen ion transport kinetics depending on how the gas-solid reaction is driven [29]. As depicted in Figure 5 (a), the oxygen reduction (left side) and oxidation (right side) reactions (Equation 4) are driven electrochemically by an applied electrical potential gradient. This also accounts for ion motion within the solid electrolyte, while electrons are supplied via an external circuit through the current collectors. An oxygen tracer experiment is depicted in Figure 5 (b). Here, no chemical or electrical potential gradients exist, but rather one monitors the incorporation reaction of oxygen gas molecules at the material's surface by the random exchange in isotope composition with time. Lastly in Figure 5 (c), a chemical driving force is generated by making step changes in the $pO_2$ in the gas phase leading to oxygen incorporation into the solid for increasing $pO_2$ or oxygen loss upon decreasing $pO_2$. For case (c) where oxygen stoichiometry changes are induced, electrons must be simultaneously transported and so the effective diffusivity, known as the chemical diffusivity, is impacted by both the diffusivity of ions and electronic charge carriers. These conceptually different experiments yield three oxygen surface exchange and diffusion coefficients as listed in Table 1.
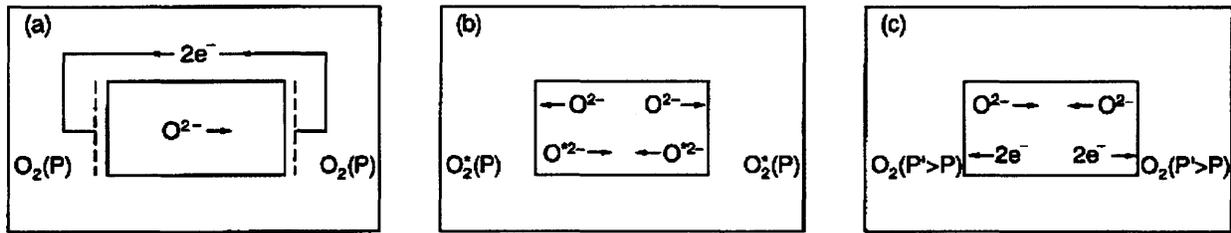


Figure 5. The three basic experiments for oxygen transport coefficients. Reprinted from a reference [30].

Table 1. Oxygen surface exchange and diffusion coefficients from different experiments.

| | Driving force | Transport coefficients |
|---|---|---|
| Electrical experiment | Electrical potential | $k_{elec}$ $D_{elec}$ |
| Tracer experiment | Tracer chemical potential | $k_{tracer}$ $D_{tracer}$ |
| Chemical experiment | Oxygen chemical potential | $k_{chem}$ $D_{chem}$ |

## 1.4 Oxide thin films

### Dense thin film electrodes as a model system

Porous structured electrodes are conventionally used in SOFCs, thereby providing easy diffusion paths for gas molecules and maximized active surface area for the targeted reaction. However, due to the complexity in morphology of the porous structure, a mechanistic understanding of the electrochemical reaction and a quantitative investigation of the materials' intrinsic properties are difficult to be achieved. Dense thin films, with geometrically well-defined, simple and reproducible structure, are therefore instead being studied as model electrodes [31]. For example, the path of the oxygen reduction reaction (Figure 4) could be examined by normalizing the electrode polarization resistance with respect to electrode geometry such as surface area, film thickness, triple phase boundary length (TPBL) and surface roughness [32]. Furthermore, the thin film structure enables one to investigate more readily the correlation between electrochemical reactivity and electrode microstructure given that compositional variations, crystallographic orientation and grain size can be controlled in the film by varying deposition conditions including background gas composition/pressure, kinetic energy of deposited particles and crystallographic orientation/temperature of the substrate, etc. Thin film oxides are also becoming more practically relevant given that many applications are tending towards the use of thinner structures, for example, in the fields of $\mu$-SOFC [3,14,33,34], chemical sensors [35] and memristors [36].

### Pulsed laser deposition (PLD)

Among various vacuum based physical vapor deposition (PVD) techniques used to fabricate thin film structures, pulsed laser deposition (PLD) has been widely used to prepare high quality thin films of many different materials, after achieving successful growth of chemically complex high Tc superconducting films in the late 80's [37]. In this technique, a high power pulsed laser beam is utilized to supply energy to target materials thereby inducing a vapor plume which is made to impinge on a nearby substrate surface [38]. Rapid increases in target surface temperature (up to about $10^3$ °C) enables quite

precise transfer of chemical composition from multi-component target materials onto nearby substrates [39]. Furthermore, multilayers and/or films with compositional variations can be easily fabricated by the PLD technique by changing target materials, upon which the laser beam strikes, with the aid of a computer-controlled target holder while maintaining vacuum and gas conditions [40].

## *1.5 Characterization tools for oxygen nonstoichiometry and transport kinetics in thin films*

### *1.5.1 Limitation of conventional techniques*

Specific examples of experimental methods, utilized for investigating oxygen nonstoichiometry and transport kinetics in oxide materials, include electrical conductivity, dilatometry, thermogravimetric analysis (TGA), coulometric titration, X-ray diffraction (XRD) and oxygen isotope tracer measurements, the latter using secondary ion mass spectrometry (SIMS). Deviations in oxygen stoichiometry can be monitored by measuring changes in experimentally measurable properties such as conductivity, sample dimensions, mass and lattice parameter, while reaction kinetics can be investigated by monitoring the time dependent relaxation of these quantities between equilibrium states.

Each experimental technique has its own merits and specific advantages. However, many of these exhibit limitations, especially when applied to thin film structures. For example, electrical conductivity measurement data must be interpreted with a confirmed defect model. Additionally values for the mobilities of the electronic and ionic charge carriers are needed to convert conductivity values to defect concentrations, and even when these are known for bulk specimens, they may differ in thin films. Furthermore, surface exchange kinetics derived from electrical conductivity relaxation (ECR) measurements are likely to be affected by the catalytic activity of the metal current collector. While TGA and coulometric titration directly measure changes in oxygen content ($\Delta\delta$), upon oxidation or reduction, a reference value $\delta_{ref}$ at a well-defined thermodynamic state is needed in order to establish $\delta$ (T, $pO_2$). Given limited sensitivity of TGA and dilatometry, these methods are generally inappropriate for monitoring changes in mass and dimensions for thin film structures. Oxygen isotope tracer measurements

allow the clear deconvolution of surface exchange and diffusion coefficients using quenched diffusion profiles, however the measurement is time consuming, utilizes expensive instrumentation, is destructive and cannot be performed *in-situ*.

## 1.5.2 Electrochemical impedance spectroscopy (EIS)

Electrochemical impedance spectroscopy (EIS) is a widely applied technique for studying both the electrical transport properties of bulk materials and the electrochemical reaction at interfaces [41]. Experimentally, a sinusoidal perturbation (e.g. $v(t) = V \cdot \sin(\omega t)$) with small amplitude $V$ is applied to the system, and the amplitude and phase of the corresponding response (e.g. $i(t) = I \cdot \sin(\omega t + \theta)$) are measured as a function of angular frequency, $\omega$. The most important merit of EIS is that the total impedance of a material can be separated into a number of frequency dependent components. For example, the electrical resistance and capacitance of a polycrystalline oxide can be deconvoluted into the contributions from grains, grain boundaries, and electrodes. Each transport process can often be modeled by parallel resistor-capacitor networks, represented as semicircles in the complex impedance plane (see Figure 6) [42]. The diameter of each semicircle is a measure of the resistance ($R$) while the inverse of the frequency in radians/sec at the peak of the semicircle gives the time constant, $\tau = \omega_o^{-1} = RC$. If time constants associated with the different processes in a system differ by orders of magnitude, the semicircles are not overlapped, as in Figure 6. However, overlapping semicircles are commonly obtained, so fitting procedures are required for extracting the corresponding $R$ and $C$ values.
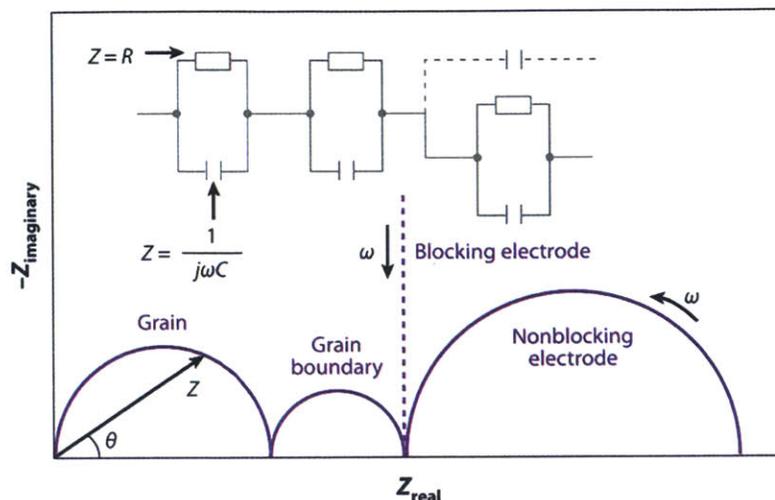
**Figure 6. Complex plane plot of typical impedance spectra for a solid with grain boundaries and either blocking (dashed line) or partially (non) blocking electrodes. The electrical circuit analog is shown with definitions of impedance for a resistor and a capacitor. Reprint from a reference [42].**

## 1.5.3 Optical spectroscopy

Optical spectroscopic techniques using visible, ultraviolet and infrared light can provide independent routes to the investigation of a large variety of physical and chemical process in solids, which are sometimes not accessible by other conventional techniques [43,44]. Light absorptivity in the spectra is correlated with the concentration of the species responsible for the absorption. In addition to investigation of thermodynamic properties, kinetic processes also can be studied by monitoring changes in spectral shape with time following a change in e.g. temperature or atmosphere. Optical characterization techniques benefit from the ability to readily achieve *in situ* and contact-free measurements, and with high spatial resolution, due to the local nature of the interaction of electromagnetic radiation with solid matter.

While optical absorption resulting from electronic transitions within rare earth and transition metal oxides are widely studied [43,45–53], relatively few studies report its use to investigate defect thermodynamics and redox kinetics. An example where this has been successfully done has been in the study of oxygen surface incorporation and chemical diffusion kinetics in Fe doped $SrTiO_3$ single crystals ([Fe] = 0.03 to 0.29 mol%) in which Fe acted as a *color indicator* [54–60]. The introduction of $Fe^{4+}$ ions into $SrTiO_3$ creates two broad absorption bands centered at 2.2 and 2.9 eV in the visible. Time and spatial

33

resolved optical absorption spectra were recorded as a function of temperature and $pO_2$. The absorption spectral data were correlated with the equilibrium concentration of $Fe^{4+}$ and finally oxygen vacancy and $Fe^{3+}$ concentration. Other examples of similar studies for single crystals include $Fe^{3+}$, $V^{4+}$, $Ce^{3+}$ and $Mn^{3+}$ in YSZ [61,62], $Mn^{5+}$ in $YAlO_3$ [63] and $Ni^{3+}$ in $SrTiO_3$ [64].
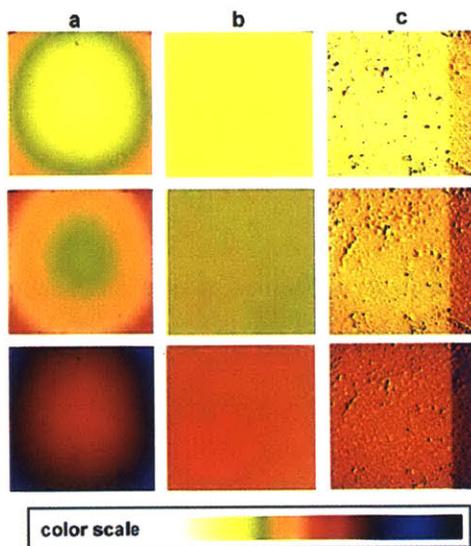


**Figure 7. In situ optical absorption images of oxygen incorporation in Fe-SrTiO₃ single crystal through diffusion-controlled (a), surface-reaction controlled (b), or (blocking) grain boundary controlled processes (c). The time sequence is from top to bottom after a stepwise increase in the oxygen partial pressure. At t=0 and t=1, the profiles are in accord with the colors given at the very left and the very right side of the scale which represents the increasing concentration of Fe⁴⁺ ions. Reprint from a reference [59].**

## *1.6 (Pr,Ce)O₂₋δ fluorite model cathode system (PCO)*

### *1.6.1 Defect chemistry and transport model of PCO*

In recent studies by Bishop et al., measurements of oxygen non-stoichiometry and electrical conductivity performed on bulk PCO were reported, and on this basis, a defect equilibrium model was developed [65,66]. Unlike fixed valent acceptor doped or undoped $CeO_2$, multivalent doping using $Pr^{4+/3+}$ ($Pr_{1-x}Ce_xO_{2-\delta}$ ; denoted 100x·PCO) leads to a pronounced mixed ionic electronic conductivity (MIEC) at high oxygen partial pressure ($pO_2 \sim$ air), a key property of many advanced SOFC cathode materials [67]. The ionic conductivity arises from the formation of oxide ion conducting oxygen vacancies (acceptor

behavior), and, for high enough Pr concentration ($\geq 5$ mol%), the electronic contribution exists due to small polaron hopping of electrons between Pr cations. The key defect reactions describing the reduction of PCO and the exchange of electrons between empty $Pr^{4+}$ acceptor states and the conduction band, written in Kröger-Vink notation, are given by.

$$O_O^X \leftrightarrow 2e' + V_O^{\cdot\cdot} + 1/2O_2(g) \tag{8}$$

$$Pr_{Ce}^X + e' \leftrightarrow Pr_{Ce}' \tag{9}$$
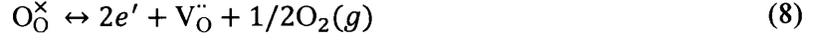
where $Pr_{Ce}^X$, $Pr_{Ce}'$, $e'$, $O_O^X$, and $V_O^{\cdot\cdot}$ are tetravalent Pr and trivalent Pr on cerium sites, electrons in the ceria conduction band, oxygen on an oxygen site, and an oxygen vacancy, the latter with net positive charge of two. In the superscripts, $\times$, *prime* and *dot* represent net charges of zero, -1 and +1 respectively. Equations (8) and (9) are written in a two-step process, whereby, electrons are generated upon reduction, followed by their drop down into the lower Pr acceptor level. Therefore, considering the Pr contribution, the reduction reaction in PCO can be rewritten as below and followed by the corresponding mass action equation.

$$2Pr_{Ce}^X + O_O^X \leftrightarrow 2Pr_{Ce}' + V_O^{\cdot\cdot} + 1/2O_2(g) \tag{10}$$
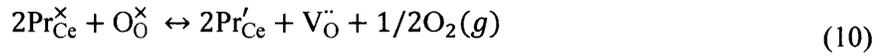
$$\frac{[Pr_{Ce}']^2[V_O^{\cdot\cdot}]pO_2^{1/2}}{[Pr_{Ce}^X]^2[O_O^X]} = k_{r,Pr}^{\circ}\exp\left(\frac{-H_{r,Pr}}{kT}\right) \tag{11}$$

In the equilibrium equation, $k_{r,Pr}^{\circ}$ is a pre-exponential term and $H_{r,Pr}$ is the enthalpy for the reaction. Previously, $H_{r,Pr}$ in $Pr_{0.1}Ce_{0.9}O_{2-\delta}$ thin films was found to be lower than that in the bulk case [68]. The oxygen nonstoichiometry $\delta$ is defined by

$$\delta = [V_O^{\cdot\cdot}]/[Pr_xCe_{1-x}O_2] \tag{12}$$

where $[Pr_xCe_{1-x}O_2]$ is the concentration of PCO in #/cm³. The condition for charge neutrality is given by

$$[Pr_{Ce}'] = 2[V_O^{\cdot\cdot}] \tag{13}$$

with the understanding that the concentrations of holes, reduced Ce, and oxygen interstitials are negligibly small under the investigated conditions at $pO_2$s in the vicinity of air, relevant for SOFC cathode operation. Mass and site conservation reactions for PCO are given by

$$[Pr'_{Ce}] + [Pr^x_{Ce}] = [Pr_{Ce}]_{total} = x[Pr_xCe_{1-x}O_{2-\delta}] \tag{14}$$

### 1.6.2 Cathodic activity of PCO thin film electrodes

The electrode polarization resistance of PCO dense thin film electrodes, deposited onto yttria-stabilized zirconia (YSZ), was investigated by Chen et al [69]. Electrochemical impedance spectroscopy (EIS) measurements with varying geometries showed that the electrode impedance was independent of electrode thickness and inversely proportional to electrode area, which pointed to oxygen surface exchange limited kinetics, rather than bulk diffusion limitations. The characteristic thickness ($L_C = D/k$) is defined as the ratio of the oxygen self-diffusion coefficient ($D$) and the corresponding surface exchange coefficient ($k$), and above this thickness, mass transport through the electrode becomes the dominant rate limiting process relative to the surface exchange reaction [70]. The characteristic thickness ($L_C$) of PCO, calculated by using the oxygen diffusion coefficient derived from an analysis of electrical conductivity measurements and the electrical surface exchange coefficient, is $\sim10^3$ $\mu$m at 550 - 670 °C, which given typical film thickness of 100s of nanometers, confirms surface exchange controlled kinetics. As shown in Figure 8 (a), the electrode performance of PCO is comparable with that of several high performance cathode materials and demonstrates the suitability of PCO as a potential cathode material. This becomes especially interesting given PCO's natural compatibility with ceria-based solid electrolytes, given its identical fluorite structure, excellent lattice match, and similar chemistry. In addition, the relatively large measured values of the electrode capacitance ($\sim10^{-2}$ Fcm$^{-2}$), typical for chemical capacitances (see below), are indicative of a high degree of nonstoichiometry, as reported for other thin film MIEC systems [32,71].
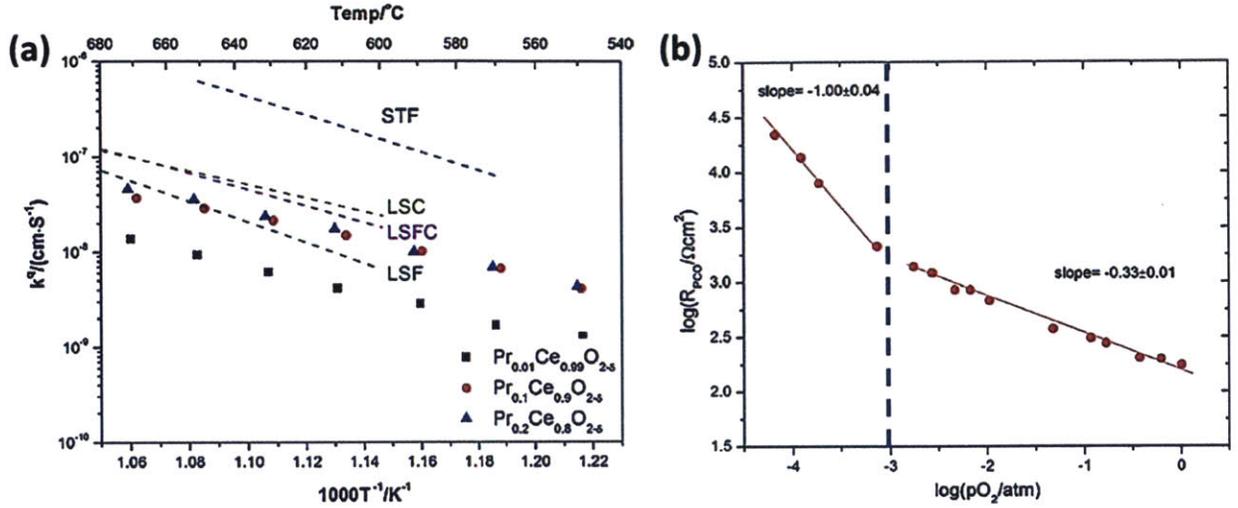
**Figure 8. (a) Temperature dependence of the electrical surface exchange coefficient ($k^q$, $k_{elec}$ in this thesis) of PCO thin film electrodes compared with other dense thin-film MIEC electrodes fabricated by PLD: LSF (La$_{0.6}$Sr$_{0.4}$FeO$_{3-\delta}$), LSFC (La$_{0.6}$Sr$_{0.4}$Fe$_{0.8}$Co$_{0.2}$O$_{3-\delta}$), LSC (La$_{0.6}$Sr$_{0.4}$CoO$_{3-\delta}$) and STF (SrTi$_{0.5}$Fe$_{0.5}$O$_{3-\delta}$). (b) pO$_2$ dependence of area specific resistance (R$_{PCO}$) of 10PCO at 670 °C. The pO$_2$ at which an apparent transition in rate limiting mechanism occurs is indicated by the vertical dashed line. Reprinted from a reference [69].**

*1.6.3 Chemical capacitance (C$_{chem}$) and defect chemistry model of thin films*

The chemical capacitance ($C_{chem}$) is related to the chemical storage capacity of a material under an applied electrical potential. In the PCO system, this is reflected in the formation and annihilation of electro-active species such as $V_O^{\cdot\cdot}$ and $Pr'_{Ce}$ [68,72,73]. $C_{chem}$ is expressed as

$$C_{chem} = -\frac{8q^2 V_{film}}{kT}\left(pO_2 \frac{\partial[V_O^{\cdot\cdot}]}{\partial pO_2}\right) \tag{15}$$

Then, the oxygen vacancy concentration in the film can be calculated at each pO$_2$ by integrating Equation (15) with respect to pO$_2$ as

$$[V_O^{\cdot\cdot}](pO_2) = \frac{kT}{8q^2 V_{film}}\int C_{chem}\, dlnpO_2 + [V_O^{\cdot\cdot}](pO_2^\circ) \tag{16}$$

where $pO_2^\circ$ is a reference oxygen pressure at which $[V_O^{\cdot\cdot}]$ is known. In the case of the PCO system, the ability to extract reliable reference values for $[V_O^{\cdot\cdot}](pO_2^\circ)$ directly from measurements of $C_{chem}$ has been demonstrated by Chen et al [68]. This is possible when the mass balance and electroneutrality relations

37

take on the approximations described in Equations (17) or (18) when either nearly all of the Pr ions are oxidized to $Pr^{4+}$ (i.e. high $pO_2$) or when nearly all the Pr ions are reduced to $Pr^{3+}$.

$$[Pr_{Ce}^{\times}] \approx [Pr_{Ce}]_{total} \tag{17}$$

$$[Pr_{Ce}'] = 2[V_0^{\cdot\cdot}] \approx [Pr_{Ce}]_{total} \tag{18}$$

Under these circumstance, $[V_0^{\cdot\cdot}]$ could be extracted directly from an experimental measurement of $C_{chem}$, by using Equation (19) and (20) for the conditions described in Equation (17) and (18), respectively [68].

$$C_{chem} = \frac{4}{3} \frac{q^2 V_{film}}{kT} [V_0^{\cdot\cdot}] \tag{19}$$

$$C_{chem} = \frac{q^2 V_{film}}{kT} ([Pr_{Ce}]_{total} - 2[V_0^{\cdot\cdot}]) \tag{20}$$

Values of $\delta$, where the approximation given in Equation (17) and (18) is not valid, can be calculated by using Equation (16) and utilizing $[V_0^{\cdot\cdot}](pO_2^{\circ})$ obtained by Equation (19) or (20). It is worth noting that Equation (15) and thus Equation (16) are valid only for spatially uniform concentrations of defects. This condition is satisfied for the PCO films studied here, since surface oxygen exchange, as opposed to chemical diffusivity, limits oxygen transport in and out of the film, leading to rapid and uniform redistribution of defects within the film [69].

## 1.7 Objectives of the research

While it is recognized that the defect equilibria, electronic and ionic transport properties and surface exchange parameters in oxides play key contributing roles in the performance of SOFC electrolytes and electrodes, permeation membranes, solid state batteries, gas sensors, etc., there are strikingly few materials where a complete picture of these properties exists. This is even more true when one considers thin films for which substrate-film interactions, high-surface- or interface-to-volume ratios (e.g. grain boundaries) are believed to modify the above properties. The key objectives of this study are to introduce novel means for investigating defect equilibria, and key kinetic processes in thin oxide MIEC films in an *in-site* fashion and correlate these findings with SOFC cathode performance. This is expected to have an important impact on research in the field, since it will allow investigators to more effectively isolate and examine the various factors contributing to electrode performance. Towards these ends, I focus on the following in my thesis:

1. Investigate the optical absorptivity (i.e. color change) of PCO thin films, and correlate it with defect chemical properties.

2. Investigate the defect equilibria of PCO thin films by simultaneous *in situ* optical absorption and EIS measurements.

3. Determine the extinction coefficient of the $Pr^{4+}$ color center and correlate it with oxygen nonstoichiometry

4. Investigate surface exchange reaction kinetics of PCO thin films by simultaneous *in situ* optical absorption and EIS measurements.

5. Investigate the correlation between surface chemistry, nature of current collector and consequent electrochemical reactivity.

6. Demonstrate ability to study chemical diffusion in PCO thin films by color front motion.

7. Investigate means for correlating chemically and electrically derived surface exchange reactions.

# CHAPTER 2. EXPERIMENTS

## 2.1 Sample Preparation

### 2.1.1 Powder synthesis; Pechini method

The Pechini-based sol-gel process was used in the preparation of PCO powders [74]. The following starting materials were utilized: cerium (III) nitrate hexahydrate, 99.99% (Sigma Aldrich), praseodymium (III) nitrate hydrate, 99.9% and ethylene glycol (Alfa Aesar) and citric acid anhydrous (Fisher Scientific) to fabricate 1, 10, and 20 mol% PCO (1PCO, 10PCO, and 20PCO, respectively). Aqueous solutions of metal nitrates were mixed together by stirring, followed by addition of citric acid and ethylene glycol. The resultant mixtures were heated to 80 ~ 100 °C until polyesterification resulted in a gel. After drying in an oven at 110 °C, the as-obtained powder was prefired at 300 or 450 °C for 4 h in air, followed by calcination at 700 °C for 3h.

### 2.1.2 Deposition of PCO thin films by PLD

Thin films of pure $CeO_2$, 1PCO, 10PCO and 20PCO were prepared by means of pulsed laser deposition (PLD) (Neocera Inc., Beltsville, ML). The dense oxide targets, used for deposition, were prepared by uniaxially pressing ~18 g of the above powders in a cylindrical stainless steel die of 1-3/16" diameter at 23 MPa for 90 seconds. After pressing, the targets were sintered at ~1450 °C under a $N_2$ atmosphere. The relative density of sintered targets were 81 ~ 86 %. The single crystal substrates used in this study were (0001) oriented sapphire, (001) oriented YSZ (8 mol% $Y_2O_3$ stabilized zirconia) and (001) oriented MgO, supplied by MTI Corporation (Richmond, CA). These substrates exhibited optical transparency and only small changes in refractive index over the wavelength region of this study. After reaching the base pressure (5 ~ 8.5 × $10^{-6}$ Torr) in the PLD chamber, the substrates were heated to 500 °C or 700 °C. The actual substrate temperature was calibrated by attaching additional temporary thermocouples on the sample surface. A Coherent (Santa Clara, CA) COMPex Pro 205 KrF eximer laser, emitting at a wavelength of 248 nm, was used for ablating the target materials. The typical parameter

configuration was 400 mJ/pulse and a 8 or 10 Hz laser repetition rate. In order to reveal clean and stoichiometric surfaces, pre-ablation of the target material with 2000 to 3000 pulses was performed before every deposition. The oxygen pressure was maintained at 10.0 mTorr during deposition, followed by post deposition annealing at the deposition temperature in 6 - 7 Torr of oxygen pressure in the same PLD chamber to facilitate complete oxidation of the films.

### 2.1.3 Deposition of MgO thin films by RF sputtering

For the experiment monitoring color front motion, an approximately 500 nm thick cover layer of MgO was deposited by reactive RF magnetron sputtering (Kurt J. Lesker, Clairton, PA). Before deposition, the substrate stage was heated to 350 °C for ~1 hour under mechanical pumping in order to clean the stage. After reaching the base pressure of $< 5 \times 10^{-6}$ Torr using a cryogenic pump (Cryotorr 8, CTI Cryogenics, Chelmsford, MA), the substrate was heated to 300 °C by halogen lamps located behind the substrate. A deposition pressure of 20 mTorr with $Ar : O_2 = 90 : 10$ was maintained using mass flow controllers (1179A) operated with a 647C process controller (MKS instruments, Wilmington, MA). An Advanced Energy RFX-600 power supply (Fort Collins, CO) provided RF power of 100 W during 2 hours of deposition.

## 2.2 Physical characterization

### 2.2.1 X-ray diffraction

X-ray diffraction (XRD) measurements were performed on synthesized powders and deposited films using a Panalytical Multipurpose Diffractometer (Westborough, MA), to obtain information on crystal phase and preferential orientation. The diffractometer was used in a theta-two theta reflection arrangement with monochromated Cu Kα ($\lambda = 1.541$ Å) X-ray radiation and an Open Eulerian Cradle sample stage. Diffraction patterns were analyzed using the software package HighScore (Panalytical, Westborough, MA) and compared with standards from the ICCD powder diffraction file.

## 2.2.2 Atomic force microscopy

The surface roughness, morphology and grain size of PCO films were characterized by a Vecco Metrology Nanoscope IV Scanned Probe Microscope Controller with a Dimension 3100 SPM (Santa Barbara, CA). The z-axis limit of the microscope was sometimes reduced from 8 to 1 μm in order to improve the resolution of the surface micrographs. Micrographs were analyzed to determine the root mean square (RMS) surface roughness and grain size using Vecco's Nanoscope software (version 5.12r3).

## 2.2.3 Optical transmission spectroscopy

Transmittance spectra of as-prepared and quenched undoped ceria and PCO films were recorded with the aid of a Cary 500i UV-Vis-NIR Dual-Beam Spectrophotometer (Agilent, Santa Clara, CA). The thin film stage was used with the blank stage as a reference. The transmittance of the films was investigated over the wavelength range of 200 to 800 nm.

## 2.2.4 X-ray photoelectron spectroscopy

X-ray photoelectron spectroscopy (XPS) measurements were performed in order to estimate the surface cation composition using a Perkin-Elmer PHI-5500 ESCA Spectrometer with monochromated Al Kα (1486.65 eV) X-ray radiation under a base pressure of $10^{-9}$ Torr equipped with a charge neutralizer system. All the XPS measurements were performed at 45° photoelectron takeoff angle configuration. The probing depths for Ce 3d, Pr 3d, and Bi 4f were estimated to be 3, 3, and 6 nm, respectively. The quantitative analysis of the Ce 3d, Pr 3d, and Bi 4f XPS spectra was performed using Multipack 9.0 software. Sputter etching was carried out by the EX05 $Ar^+$ ion gun. Sputter etching was carried out with 2 kV ion beam energy and 1 μA beam current on the area of $2 \times 2$ mm$^2$. A sputtering rate of around 1.7 nm/min was estimated based on the amount of sputtering time needed to completely remove a PCO layer of known thickness.

*2.2.5 Auger electron spectroscopy*

Auger electron spectroscopy (AES) (Physical Electronics Model 700 scanning nanoprobe) was used to identify lateral heterogeneities in cation compositions at the film surfaces with high spatial resolution. Electron beam settings of 20 keV and 10 nA were used for both SEM imaging and Auger electron excitation. The Ce MNN, Pr MNN, and Bi NNN Auger emissions were measured for quantifying the surface cation composition of 10PCO films. The sampling depths of these Auger electrons are ~4.0 nm for both Ce MNN and Pr MNN and ~2.5 nm for Bi NNN, estimated based on 3 times the inelastic mean free path of photoelectrons. The smoothing and differentiation of the AES spectra collected were carried out using the Savitsky-Golay algorithm. Quantification of the AES differential spectra is performed using peak-to-peak intensities of the tight-scans of the noted emissions from the constituent cations. We used the standard sensitivity factors (Physical Electronics Inc., 2011) for the chemical quantification with AES, and the sensitivity factors for these emissions in the PCO films may vary from the provided standards. Therefore, rather than the absolute values of the surface chemical content, the qualitative trends should be taken into account regarding the AES results.

*2.2.6 Wavelength dispersive X-ray spectroscopy*

In order to investigate the Pr concentration in the PCO thin films, wavelength dispersive X-ray spectroscopy (WDS) measurements were performed by using a JEOL-JXA-8200 Superprobe (JEOL, Peabody, MA) with highly sensitive WDS analyzing crystals and detectors. The standards used for Ce, Pr and O were $CePO_4$, $PrPO_4$ and $Fe_2O_3$, respectively.

*2.2.7 Scanning electron microscopy*

The surfaces of PCO films were viewed by scanning electron microscopy (SEM) to investigate cracks and other microstructural features. The microscope was a Helios Nanolab 600 Dual Beam Focused Ion Beam Milling System (FIB) (FEI, Hillsboro, Oregon). Improved resolution was achieved by using

magnetic immersion electron optics. In order to avoid charging effects, a carbon conductive coating (~5 nm) was applied to the film surfaces. Samples were attached to an aluminum stub by carbon tape.

## 2.3 Ex-situ optical absorption measurement

Undoped ceria and PCO thin films, investigated by *ex situ* transmittance measurements, were deposited by the PLD technique onto (0001) oriented single crystal sapphire substrates (10 × 10 × 0.5 mm$^3$, both-sides polished; MTI Corporation, Richmond, CA). In order to investigate difference in transmittance spectra of reduced and oxidized samples, they were heated in a quartz tube to 600 °C, in a 0.1% CO/CO$_2$ gas mixture (pO$_2 \approx 10^{-19}$ atm), for 8-10 hours. Rapid quenching to room temperature was achieved by opening the upper half of the split furnace while maintaining a flow of reducing gas. The quench rate was ~27 °C/min from 600 °C to ~100 °C.

## 2.4 Joint in-situ optical and EIS measurements

### 2.4.1 Measurement setup

A novel experimental arrangement was designed to enable the simultaneous *in situ* measurement of both optical absorption and electrochemical impedance spectroscopy (EIS), as shown in Figure 9. While one half of the thin film specimens supported on YSZ single crystal substrates were used for *in situ* optical measurements, the other half were simultaneously utilized for EIS measurements with either symmetric cells of PCO/YSZ/PCO or asymmetric cells of PCO/YSZ/Ag. Optical transmittance measurements were performed by passing a monochromated beam of light (532 nm), or scanning a wide range of wavelengths (420 nm – 560 nm), through the supported PCO films and YSZ substrate. The substrates were held vertically in specially designed quartz tubes that were placed into a split furnace, allowing the light beam to pass through the sample uninterrupted. A beam splitter reflected part of the beam to a photodetector prior to passing through the sample, as illustrated in Figure 9, to remove instantaneous and long-term variations in light source intensity. The probe beam was mechanically

chopped and detected using photodetectors connected to lock-in amplifiers, thus isolating the transmitted light from background radiation. The glass band-pass filters (FGB37, 335-610 nm or FGS900, 315-710 nm) were placed right before the photodetectors in order to minimize blackbody radiation transmitted from the hot furnace.
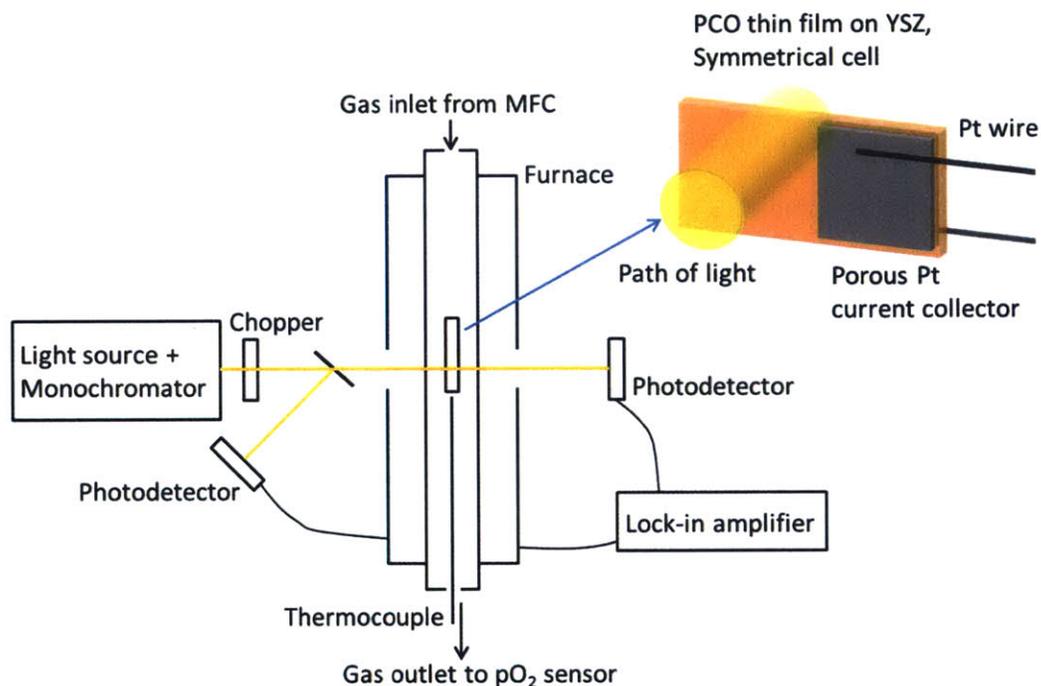


**Figure 9. Schematic diagram of the experimental setup for simultaneous *in situ* optical absorption and electrochemical impedance spectroscopy (EIS) measurements. Reprinted from a reference [75].**

## 2.4.2 Cell preparation

10PCO thin films, investigated by joint *in-situ* optical and EIS measurements, were deposited by PLD onto (001) oriented single crystal YSZ (8 mol% $Y_2O_3$ stabilized zirconia) substrates ($10 \times 5 \times 0.5$ $mm^3$; MTI Corporation, Richmond, CA), as listed in the Table 1. The transparent YSZ substrates, polished both sides, were used in the optical transmittance measurements and also served as the electrolyte for EIS measurements. All samples were grown with the same deposition conditions, in the same PLD chamber (Chapter 2. Experiments), with the aim of achieving similar film thicknesses (determined by surface profilometry, KLA-Tencor P-16+ stylus profiler) and microstructures. In order to simultaneously perform

both optical and EIS measurements on a single sample, one half of the PCO coated wafer was covered both sides by electrical current collectors while the other half was contact-metal free. An Ag counter electrode was sometimes painted on the opposite side of the YSZ wafer to form an asymmetrical PCO/YSZ/Ag electrochemical cell, by using Ag paste (SPI supplies, West Chester, PA). Alternatively, symmetrical cells of the type PCO/YSZ/PCO were prepared and characterized. The samples were mounted into a specially designed sample holder, which supports the sample in a vertical orientation and enables contact with the Pt electrical leads and thermocouple (see Figure 9 and Figure 10 (b)).

For the impedance studies, a variety of current collectors were prepared (Table 1). For Samples I (left in Figure 10 (a)), porous Pt thin layers (~200 nm) were deposited onto the surfaces of PCO films by reactive sputtering [76]. $PtO_x$ was first deposited and subsequently annealed at 650 °C in air in order to reduce Pt oxide to Pt. This reduction step results in uniform porous Pt structures which can serve as gas permeable current collectors [76]. The reactive sputtered porous Pt was chosen due to its better adhesion to the oxide film than metal contact coatings prepared with Pt or Au paste alone. This feature was important given that the sample was held vertically and required connection with the Pt electrical wires emanating from the sample holder. The Pt wires of the sample holder were directly attached to the porous Pt layer of the sample and then held in place by the applications of Pt paste, which was annealed at 700 °C. However, several trials, including the annealing step for Pt paste at high temperatures, were required to ensure good contact.

In order to avoid this problem for Sample II, after preparing the porous Pt layer as in Sample I, additional Pt wires were anchored by use of ceramic paste (Heat resistance inorganic adhesive, Aron Alpha, West Jefferson, OH) at the edge of the substrate (center in Figure 10 (a)). Then, Pt paste was applied between the Pt wires and the porous Pt layer. Finally, Pt wires attached to the sample and one from the sample holder were connected to each other. Three samples in Sample II were prepared at the same time following all the same fabrication steps, including deposition of 10PCO film by PLD and preparation of current collector and counter electrode. This was designed to minimize differences in thermal treatment history and exposure to contamination. The individual samples were then used for joint

*in-situ* optical and EIS measurements at one of the three temperatures of measurement (550 °C, 600 °C and 650 °C).

Because the Pt wire was well secured by ceramic paste for Sample III, only Pt paste was used for the current collector, eliminating one annealing step for the reactive sputtered Pt layer. In addition, as little ceramic paste was applied as possible (right in Figure 10 (a)). To examine the possible role of aging, two samples in the Sample III series were prepared at the same time. One sample was annealed during 5 cycles of sequential $pO_2$ step change at 600 °C while the other remained as-prepared as a reference.
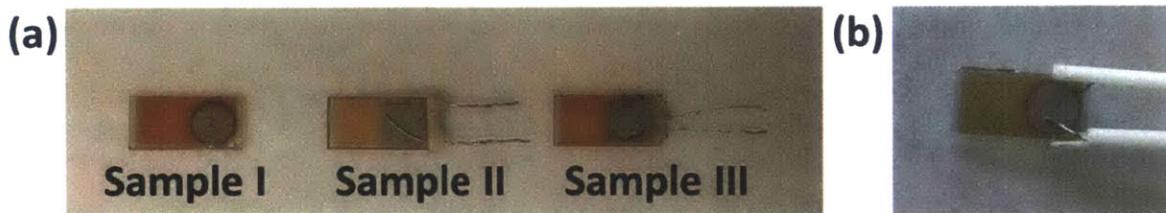


**Figure 10. Photographs of (a) Sample I, Sample II and Sample III and (b) Sample I supported by the sample holder.**

**Table 2. Samples used in joint *in-situ* optical and EIS measurement.**

| Sample set | Cell structure | PCO film thickness | Counter electrode for asymmetric cell | Current collector for PCO electrode | Ceramic paste |
|---|---|---|---|---|---|
| Sample I | Symmetric | $256 \pm 8$ nm | Not applicable | Reactive sputtered Pt + Pt paste (700 °C annealed) | × |
| Sample II | Asymmetric/ Symmetric | $260 \pm 9$ nm | Ag paste | Reactive sputtered Pt + Pt paste (650 °C annealed) | ✓ |
| Sample III | Symmetric | $254 \pm 16$ nm | Not applicable | Pt paste (700 °C annealed) | ✓ |

*2.4.3 Measurement condition*

The electrochemical impedance spectroscopy (EIS) measurements, covering the frequency range from 5 ~ 20 mHz to 65 ~ 70 kHz with an AC amplitude of 20 ~ 30 mV and zero DC bias, were performed using a combination of Solarton 1260 impedance analyzer and 1286 potentiostat/galvanostat or the ModuLab system (Solartron Analytical) in conjunction with the FRA 1 MHz (2055A) Frequency Response Analyzer module. Zview software (Scribner Associates) was used to fit the data and construct

equivalent circuits to analyze the impedance data. The oxygen partial pressure within the quartz tube was controlled by preparing Ar-$O_2$ (sometimes, $N_2$-$O_2$) and $H_2$-$H_2O$-Ar (sometimes, $H_2$-$H_2O$-$N_2$) gas mixtures with the aid of mass flow controllers (MKS instruments, Wilmington, MA) and monitored by a YSZ Nernst type oxygen sensor in an external furnace.

### 2.5 Color front motion measurement

#### 2.5.1 Cell preparation

A specially designed cell structure, as shown in Figure 11, was designed in order to provide an extended oxygen diffusion pathway. 10PCO thin films, investigated for color front motion measurements, were deposited by PLD onto a (001) oriented single crystal MgO or a (0001) oriented single crystal $Al_2O_3$ substrate ($10 \times 5 \times 0.5$ mm$^3$, one-side polished; MTI Corporation, Richmond, CA). Then, a MgO transparent oxygen diffusion barrier was deposited by RF sputtering onto the entire surface of the 10PCO film. To enable oxygen ingress into the PCO film, either the MgO cover layer and PCO film were scribed with a razor blade (see Figure 11), or the MgO substrate was cleaved along a preferred crystallographic direction to generate a clean and sharp edge.
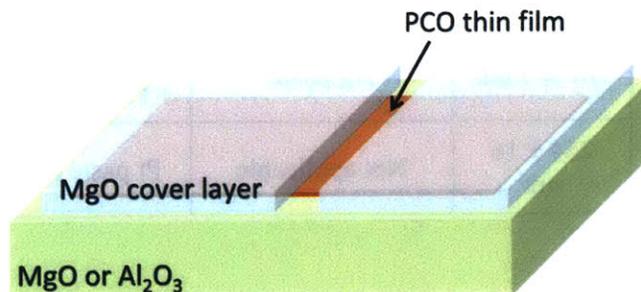


**Figure 11. Schematic of a sample design for color front motion.**

#### 2.5.2 Measurement set-up

A custom-designed heater stick [77] was utilized for the experiment. As shown in Figure 12 (a), the heater stick consists of screen-printed gold contacts and Au–Pt thermocouple at the top side and Pt-

heater lines at the bottom side of an alumina substrate, respectively. The dielectric ink is screen-printed as a shield layer. The sample with the structure of MgO/10PCO/substrate, described above (section 2.5.1), was mounted on the shield layer with Ag paste in order to ensure good thermal contact. An additional S-type thermocouple was placed on the sample surface with a point contact of Ag paste. The device's temperature was controlled by a custom-designed temperature controller, achieving up to 600 °C with maximum heating and cooling rates of ~20 °C/s in air. The temperature distribution was found to be uniform with small variance (< 4 °C), measured by an infrared thermal camera. Its small size (510 mm × 6 mm × 0.6 mm) enabled the use of a small volume chamber, and therefore made it possible to achieve a short working distance for the optical microscope as well as rapid changes in gas atmosphere. The former is particularly difficult to achieve with typical commercial furnaces.

Optical micrographs were collected using a Dino-lite microscope (Premier2-AD-7013MTL) with fixed exposure time and were saved as lossless, 8 bit-per-pixel, portable network graphics (PNG) files. In order to correct for drift of the microscope with respect to the sample during the measurements, the images were first registered using the image registration toolkit in Matlab (MATLAB and Statistics Toolbox Release 2015, The MathWorks, Inc., Natick, MA) with the first image in the series acting as the target coordinate system. In order to facilitate this process, the images are first converted from the RGB color scale to grayscale with a 1:1:1 weighting of the RGB intensity values. This weighting could be further optimized in the future to better extract the red tones contributed to the image by the $Pr^{4+}$.
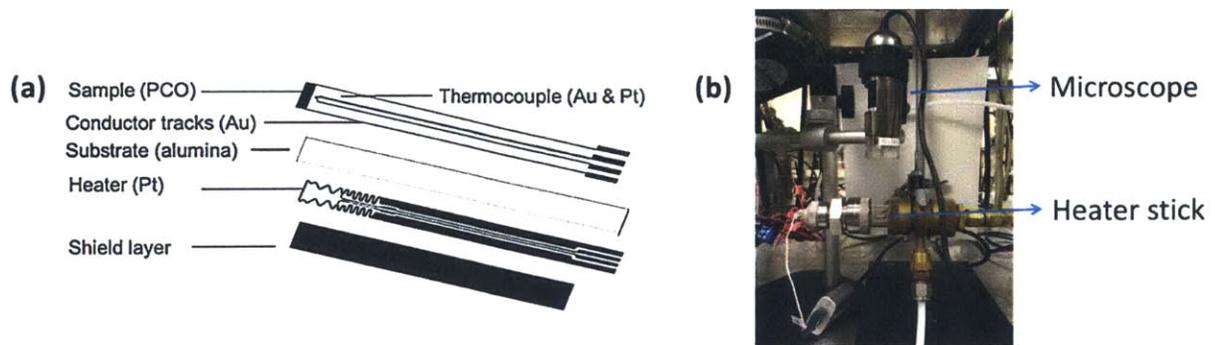


Figure 12. (a) Structure of the heater stick. Reprint from a reference [77] (b) Photo of the experimental setup for investigating color-front motion.

## 2.5.3 Measurement condition

Isothermal color front motion in 10PCO film was recorded upon rapid $pO_2$ change between 1000 ppm $H_2$/Ar and 100% $O_2$. Optical microscope images were taken in a short time interval just before and after $pO_2$ changes to capture any sudden changes. Then images were taken every 20 or 30 minutes until a new equilibrium condition was reached. The oxygen partial pressure within the quartz tube was controlled by preparing $N_2$-$O_2$ and $H_2$-Ar gas mixtures with the aid of mass flow controllers (MKS instruments, Wilmington, MA) and monitored by a YSZ Nernst type oxygen sensor in an external furnace.

# CHAPTER 3. RESULTS

## 3.1 Physical/chemical characterization of PCO powder and thin films

### 3.1.1 PCO powders

The XRD spectra of $Pr_xCe_{1-x}O_{2-\delta}$ (x=0.01, 0.1 and 0.2) powders synthesized in this study are shown in Figure 13. The results indicate that the powders are single cubic fluorite phase.
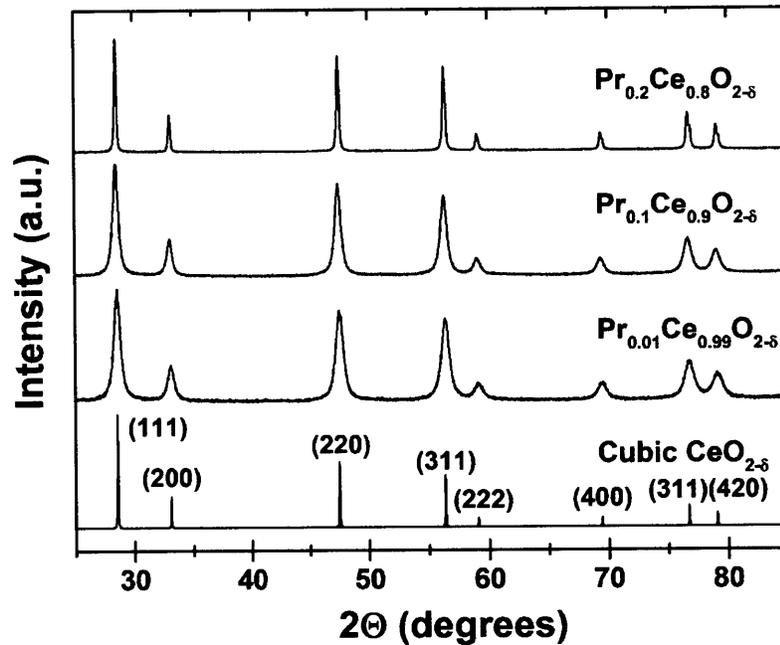


**Figure 13. XRD patterns of synthesized $Pr_xCe_{1-x}O_{2-\delta}$ (x=0.01, 0.1 and 0.2) powders in this study and reference of undoped cubic ceria (PDF# 34-394).**

### 3.1.2 PCO thin films

Figure 14 shows the XRD spectra of 10PCO thin films deposited on (a) YSZ (001), (b) $Al_2O_3$ (0001) and (c) MgO (001) single crystal substrates by pulsed laser deposition. The deposition temperature was 700 °C for YSZ and $Al_2O_3$ substrates and 500 °C for MgO substrates. Other deposition conditions were identical. The results indicate that 10PCO films on YSZ and MgO substrates are polycrystalline fluorite phase with highly (100) oriented texture, while 10PCO films on $Al_2O_3$ substrates shows two preferential

orientations of (111) and (100). There is no evidence of amorphous films, or diffraction peaks other than the ones in the cubic fluorite phase.

From wavelength dispersive X-ray spectroscopy (WDS) measurements, the Pr concentration in 10PCO thin films was found to be $9.7 \pm 0.3\%$, close to the nominal value of 10%.
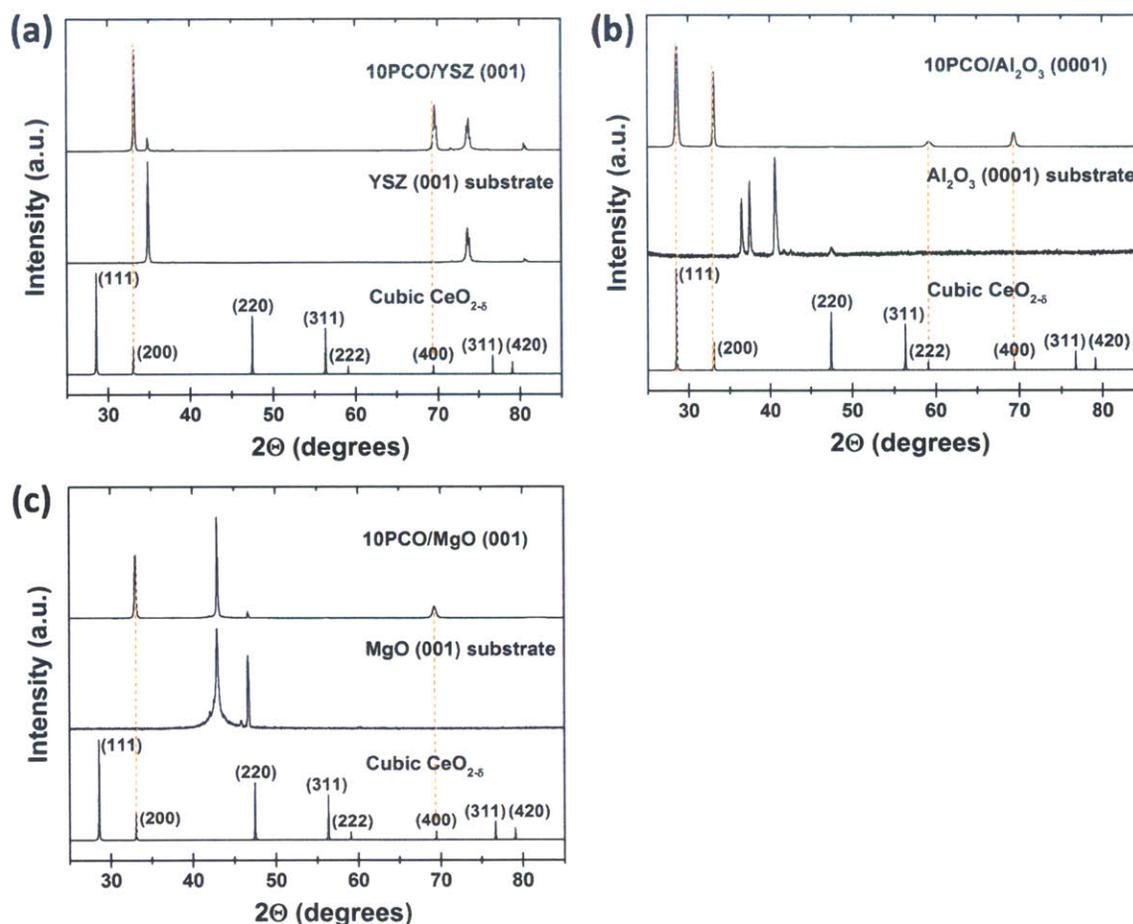


Figure 14. XRD patterns of $Pr_{0.1}Ce_{0.9}O_{2-\delta}$ (10PCO) thin films deposited on (a) a YSZ (001), (b) a $Al_2O_3$ (0001) and (c) a MgO (001) single crystal substrates by pulsed laser deposition at 700 °C for YSZ and $Al_2O_3$ substrates and at 500 °C for MgO substrates. Reference XRD pattern of undoped cubic ceria (PDF# 34-394) is also displayed for comparison.

## 3.2 Ex-situ optical transmittance measurement results of PCO thin films

Figure 15 shows the transmittance spectra of as-prepared undoped ceria and PCO thin films with different Pr doping concentrations covering the UV-visible range (300-800 nm). All films show a strong drop in transmission below about 340 nm, consistent with the band gap of $CeO_2$. At longer wavelengths, the pure ceria and 1PCO thin films exhibit a sharp increase in transmission that saturates. On the other hand, with increasing wavelength the 10PCO and 20PCO both show a gradual increase in transmission, with 20PCO being shallower, ultimately reaching a saturated transmission above about 650 nm. The oscillations in transmission are associated with light interference from film geometry. Film thicknesses of 240 nm, 300 nm, 280 nm and 280 nm for undoped ceria, 1PCO, and 10PCO and 20PCO, respectively were measured. The frequency of geometrically related oscillations in transmittance is clearly larger for the thicker 1PCO as compared to ceria, confirming them to be *thickness fringes* [78].
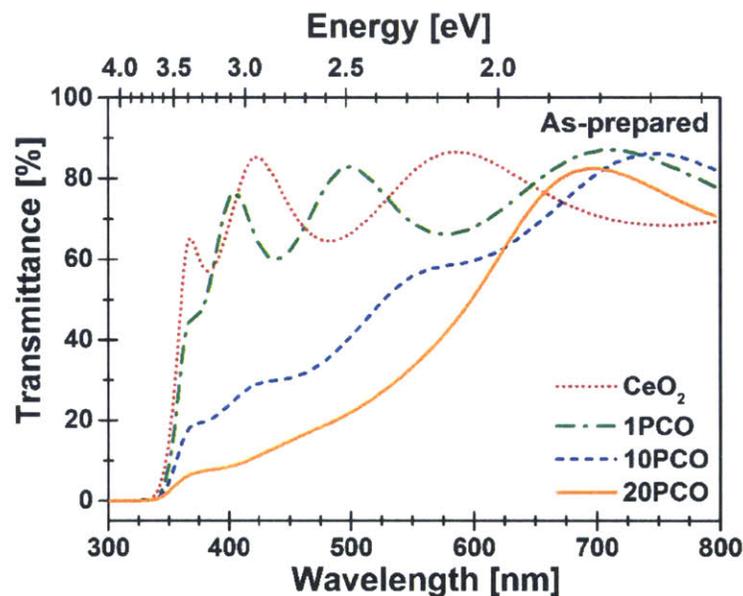


**Figure 15. Transmittance spectra of as-prepared (oxidized) undoped ceria and PCO thin films on a $Al_2O_3$ (0001) substrate.**

53

Figure 16 (a) and (b) show change in the transmittance spectra of 10PCO and 20PCO, respectively, upon reducing treatment. Due to the low absorption of 1PCO, 10PCO and 20PCO are examined for optical transmission as a function of reducing and oxidizing heat treatments. Reduced films were prepared by annealing the films at 600 °C in a 0.1% CO/CO$_2$ gas mixture (pO$_2 \approx 10^{-19}$ atm) for 8-10 hours, followed by rapid quenching to room temperature. While the undoped ceria thin film showed no visual color change, nor change in transmittance spectrum following reduction, both 10PCO and 20PCO thin films showed a dramatic color change from red to transparent, consistent with suppressed absorption from 350 nm to 600 nm after reduction.
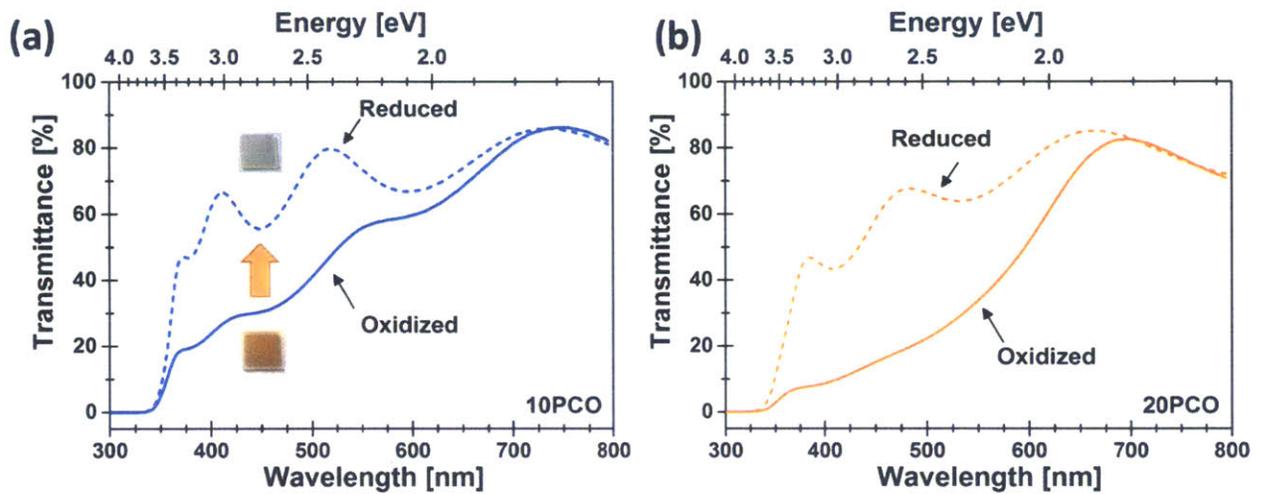


**Figure 16. Transmittance spectra of as-prepared (oxidized) and reduced thin films with different Pr doping concentration of (a) 10PCO and (b) 20PCO on a Al$_2$O$_3$ (0001) substrate.**

### 3.3 Joint in-situ optical and EIS measurement results for PCO thin film

### 3.3.1 in-situ optical transmittance measurement results

Figure 17 to Figure 19 show the time dependent transmittance, following stepwise changes in pO$_2$ for Sample I at 600 °C, Sample II at four different temperatures (550 °C to 700 °C) and Sample III at 600 °C, respectively. Transmitted light intensity was recorded while the 10PCO thin films were reduced from the initial 0.21 ~ 1 atm pO$_2$ and then oxidized again in a stepwise manner at given temperatures. For Sample I and II, the 10PCO thin films were reduced at highly reducing condition (pO$_2 \leq 10^{-18}$) where all

Pr ions become $Pr^{3+}$. The transmittance recorded at this condition was used for determining the optical absorption coefficient of the sample, i.e. $Pr^{4+}$ color centers, discussed later.

Consistent with the ex-situ quenching experiment described in the previous chapter, 10PCO thin films become more transparent when reduced, and more colored, or absorbing, when oxidized. As illustrated in Figure 17 and Figure 19, the changes in transmittance upon $pO_2$ change are reversible, given sufficient time to equilibrate. Following rapid step changes in $pO_2$, the film absorption varies with time before reaching a new equilibrium state. From the transmitted light intensity at each equilibrium state, the absorption coefficient for $Pr^{4+}$ color centers can be determined as discussed later. In addition, the optical relaxation upon $pO_2$ step changes enables one to extract the oxygen surface exchange reaction constant from these kinetics.
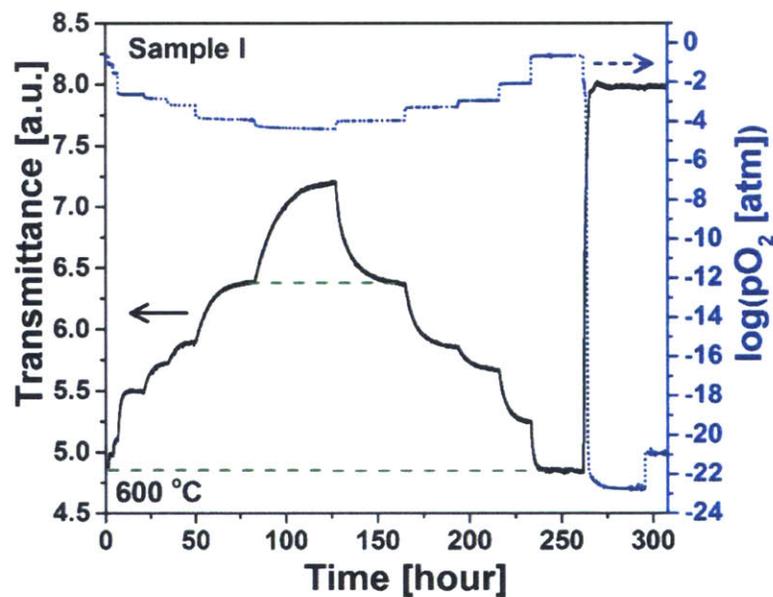


**Figure 17. Plot of transmittance and log oxygen partial pressure versus time at 600 ºC for Sample I. Redrawn from a reference [75].**
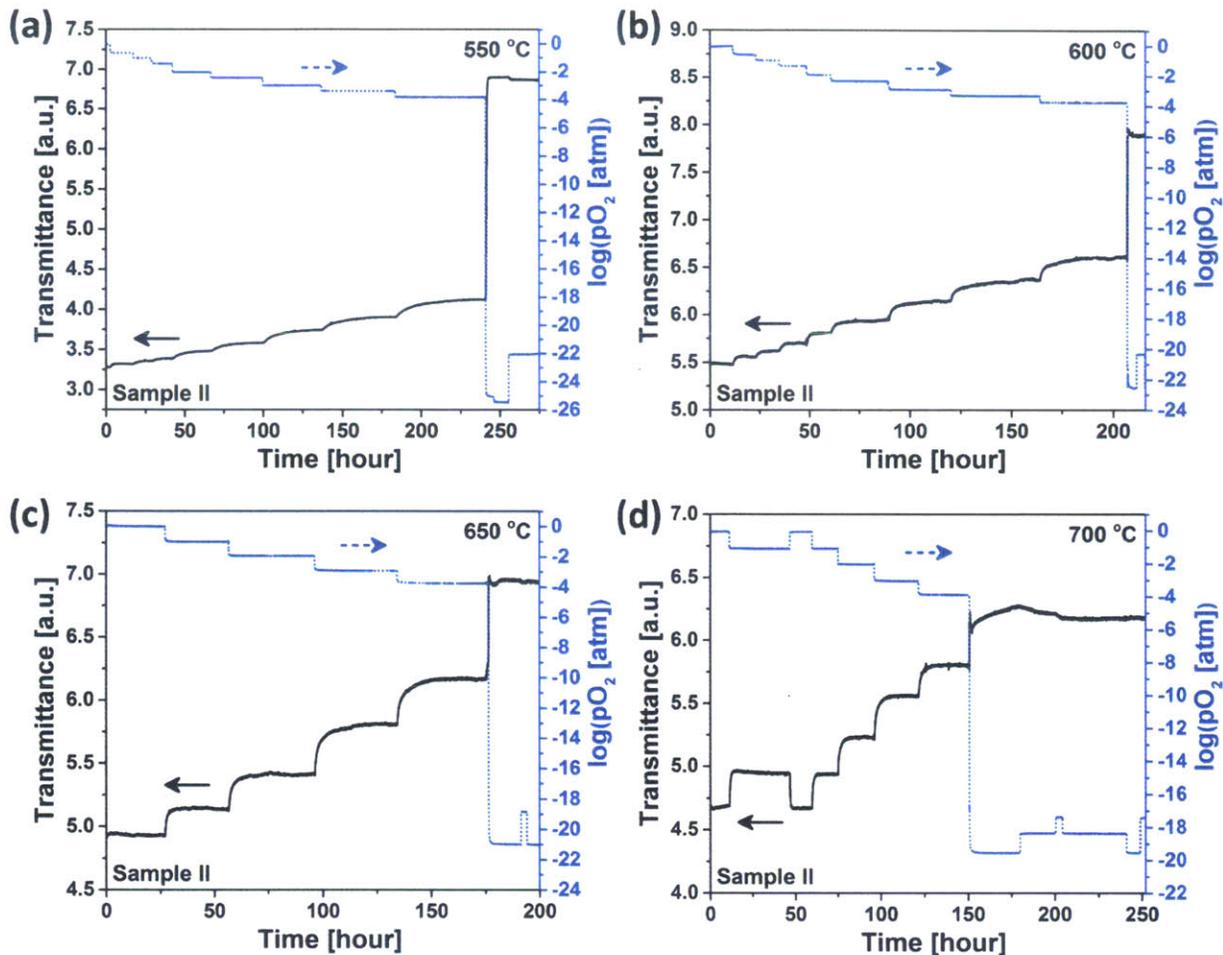
**Figure 18.** Plot of transmittance and log oxygen partial pressure versus time at 550 °C (a), 600 °C (b), 650 °C (c) and 700 °C (d) for Sample II.
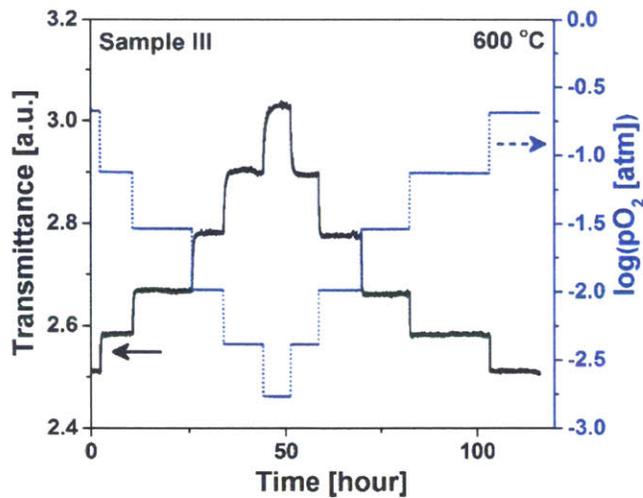


**Figure 19.** Plot of transmittance and log oxygen partial pressure versus time at 600 °C for the 5th annealing cycle of Sample III. Transmittance changes upon the same sequence of pO₂ step changes during other cycles showed similar behavior.

56

_Determination of chemical oxygen exchange coefficient, $k_{chem}$_

Figure 20 (a) shows the isothermal changes in transmitted light intensity for a 10PCO thin film following a rapid step change in $pO_2$. As the film is reduced, it becomes more transparent, which is consistent with decreasing $Pr^{4+}$ concentration, as discussed later. One observes that the equilibration time for the change in optical transmittance is much longer than the time required for establishment of the new $pO_2$ value, thus confirming that the transient behavior in absorption is solely related to the controlling reduction kinetics of the thin film specimen. Most of the transient data collected in this study showed similar behavior.

In Chen et al.'s study, the surface exchange reaction was determined to be the rate determining step in the reduction and oxidation kinetics of PCO thin films [69]. In addition, the characteristic thickness ($L_C$ = $D/k$, for definition, see section 1.6.2) of PCO, estimated to be $\sim 10^3$ μm at 550 - 670 °C, is much thicker than the PCO thin film thicknesses (< 500 nm) used in this study. Considering surface exchange controlled kinetics, relaxations in the concentration of optical absorbing centers ($Pr^{4+}$) following a $pO_2$ step change can be modeled as follows [79].

$$\frac{A_t - A_O}{A_f - A_O} = 1 - \exp\left(-\frac{t}{\tau}\right) \tag{21}$$

where $A_t$, $A_O$ and $A_f$ are absorbance due to $Pr^{4+}$ at any given time (t), initial time, and final time, respectively. Given that the transmitted light intensity decreases exponentially proportional to absorbance of the light absorbing media, Equation (21) can be expressed as below.

$$\frac{\ln(I_t) - \ln(I_O)}{\ln(I_f) - \ln(I_O)} = 1 - \exp\left(-\frac{t}{\tau}\right) \tag{22}$$

where $I_t$, $I_O$ and $I_f$ are the transmitted light intensities at any given time (t), initial time, and final time, respectively. After rearranging Equation (22) and plotting as a function of time, the time constant, $\tau$, can be extracted.

$$\ln\left(1 - \frac{\ln(I_t/I_O)}{\ln(I_f/I_O)}\right) = -\frac{t}{\tau} \tag{23}$$

Figure 20 (b) illustrates a plot of the above expression for the $pO_2$ step change condition shown in Figure 20 (a). The data are well fitted to a linear relationship, with slope equal to $-1/\tau$. The chemical surface exchange coefficient, $k_{chem}$, is obtained from the following relation [79].

$$k_{chem} = \frac{l}{\tau} \qquad (24)$$

where $l$ is the thickness of film.
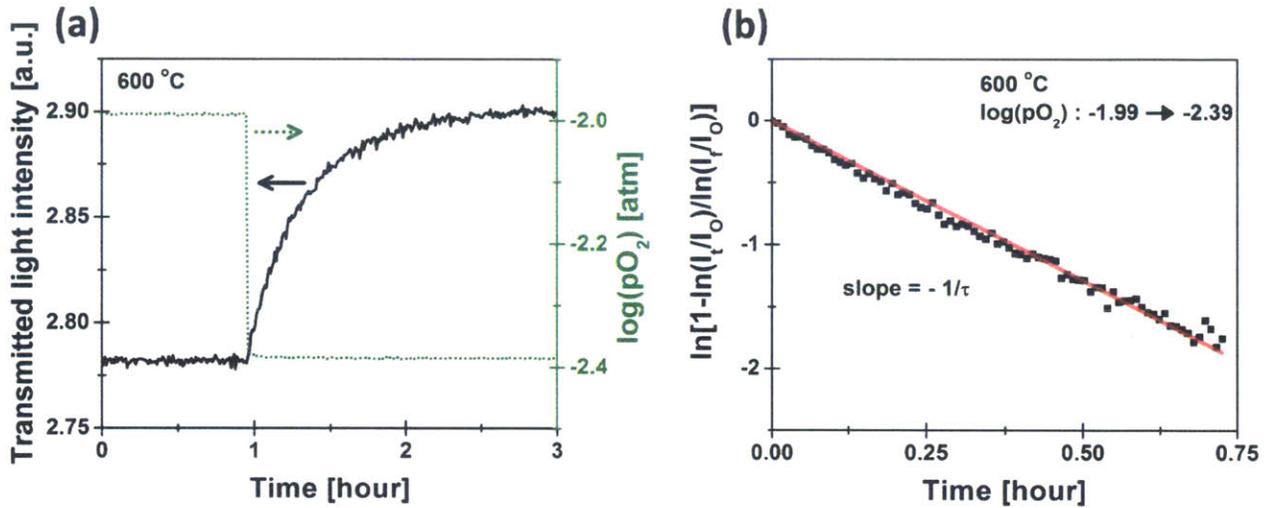


Figure 20. (a) Transmitted light intensity change upon the $pO_2$ step change from 0.01 atm to 0.004 atm at 600 °C and (b) method for extracting time constant $\tau$ from relaxation data in (a). The slope is $-1/\tau$.

Figure 21 to Figure 24 show the $k_{chem}$ values for Sample I at 600 °C (Figure 21), for Sample II at 550 °C - 650 °C (Figure 22 and Figure 23) and for Sample III at 600 °C (Figure 24). For all samples, the transmitted light intensity was recorded while the 10PCO thin films were reduced from the initial high $pO_2$ and then oxidized again in a stepwise manner. As mentioned before, for the experiments dealing with Sample II, three samples were prepared at the same time, with a different sample used at each temperature to avoid any time-dependent change in reaction kinetics due to subsequent annealing at different temperatures. Generally speaking, $k_{chem}$ shows a positive $pO_2$ dependence; i.e. $k_{chem}$ increases with increasing $pO_2$. This can be expressed by a power law dependence with $m$ as follows.

$$k_{chem} = k_{chem}^0 p_{O_2}^m \qquad (25)$$

58

For Sample I, $k_{chem}$ shows a strong pO$_2$ dependency with $m = 0.66 \pm 0.06$ during the reduction step for pO$_2$s above $10^{-3}$ atm. On the other hand, $k_{chem}$ obtained during re-oxidation shows a weaker pO$_2$ dependency ($m = 0.27 \pm 0.00$) with smaller magnitudes than the ones obtained during the reduction steps, but the data converge at lower pO$_2$. For Sample II, as shown in Figure 22 and Figure 23 (a), during the reduction step at 600 °C and 650 °C, $k_{chem}$ shows a weak pO$_2$ dependency in the measured pO$_2$ range, while the initial strong pO$_2$ dependency of $k_{chem}$ ($m = 0.49 \pm 0.11$) at 550 °C becomes weak in the lower pO$_2$ regime. On the contrary, during oxidation steps (Figure 23 (b)), $k_{chem}$ at 600 °C and 650 °C shows a stronger pO$_2$ dependency ($m = \sim 0.37$) but $k_{chem}$ at 550 °C is only weakly dependent on pO$_2$. The values of $k_{chem}$ generally become larger at higher temperature (Figure 23). At each temperature, $k_{chem}$ during oxidation steps are generally larger or comparable to ones obtained during reduction steps (Figure 22). For Sample III (Figure 24), $k_{chem}$ during oxidation is about one order of magnitude larger than the one during reduction, while their pO$_2$ dependency is similar ($m = 0.50 \sim 0.55$).
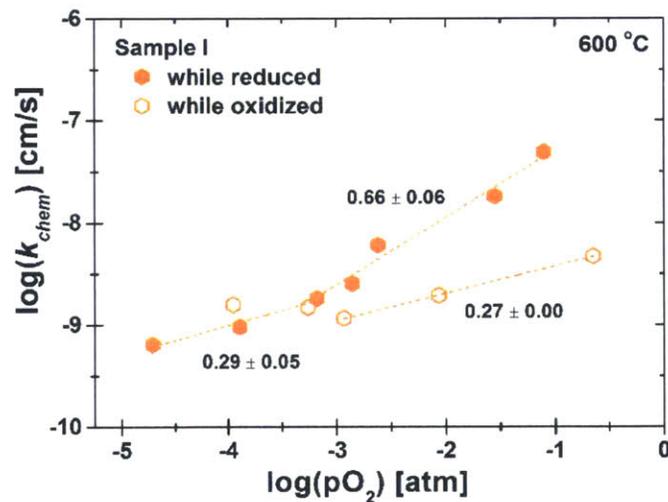


**Figure 21. Plot of $k_{chem}$ from optical relaxation versus pO$_2$ for Sample I at 600 °C. The 10PCO film was reduced and then oxidized. $k_{chem}$ values are plotted using the final pO$_2$ value for each relaxation step.**

59
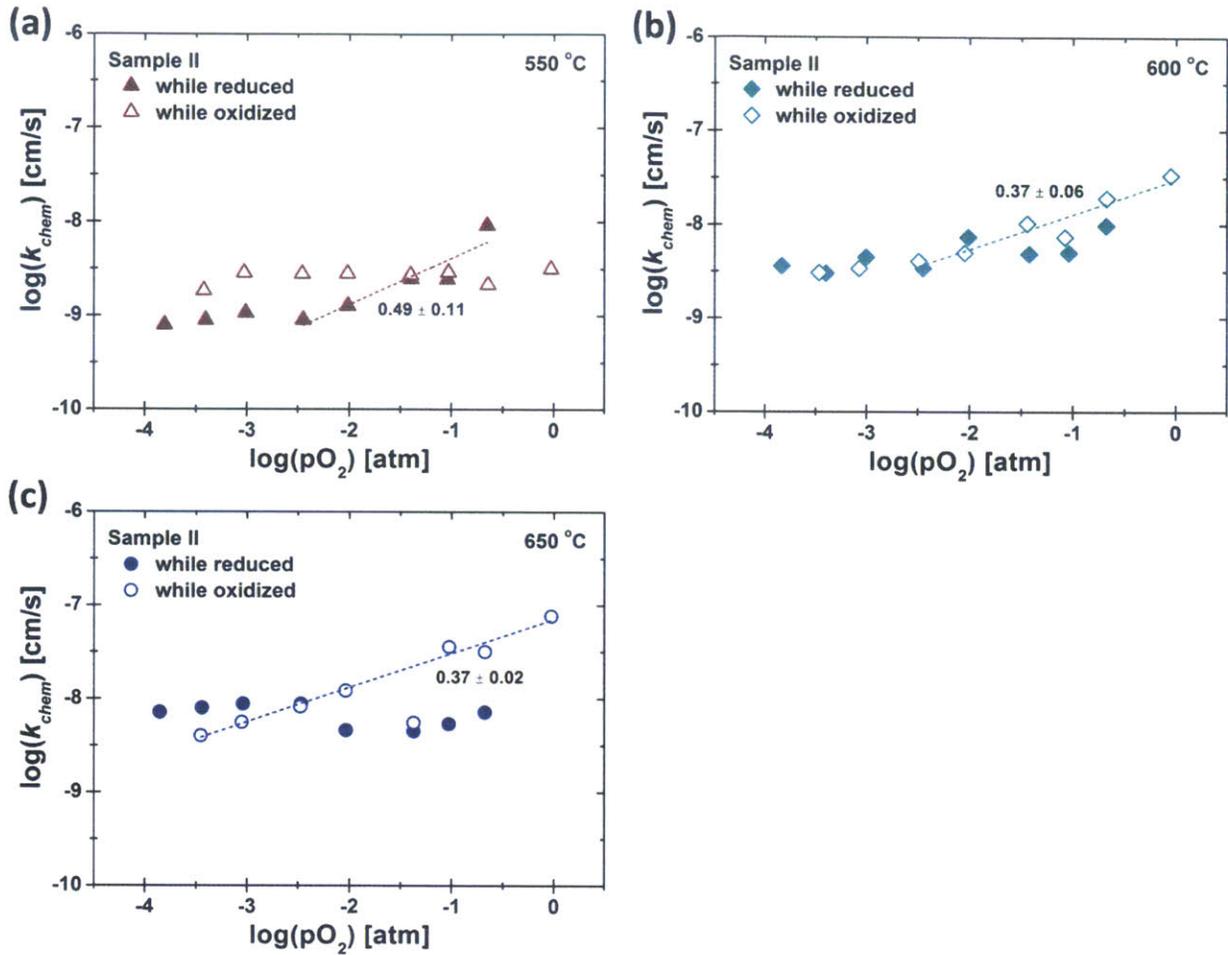
**Figure 22.** Plot of $k_{chem}$ from optical relaxation versus pO2 for sample II at 550 °C (a), 600 °C (b) and 650 °C (c). The 10PCO film was reduced and then oxidized. $k_{chem}$ values are plotted using the final pO2 value for each relaxation step.
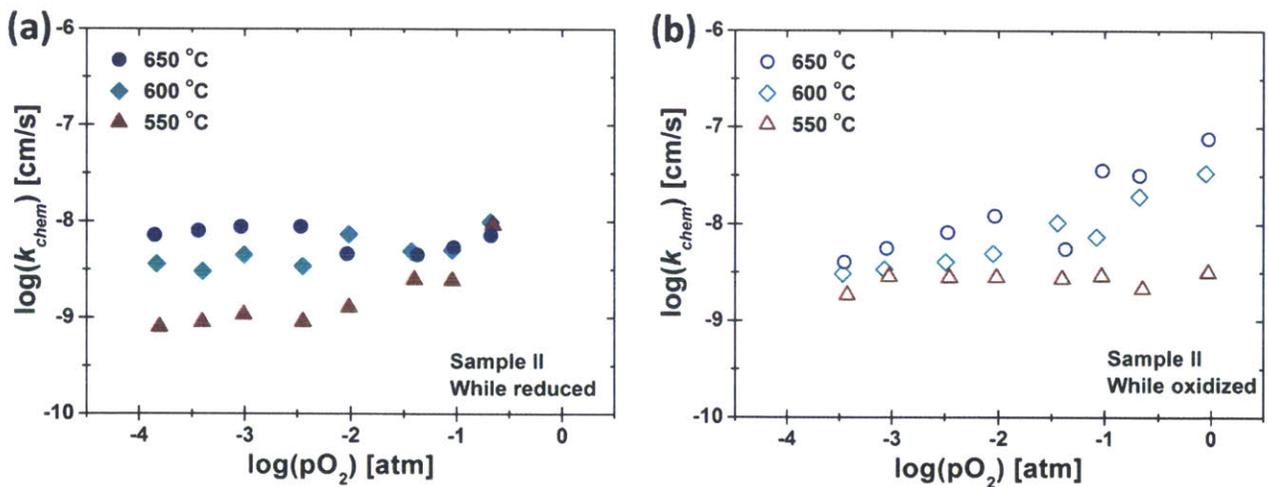


**Figure 23.** Plot of $k_{chem}$ from optical relaxation versus pO2 for sample II (a) while the 10PCO film was reduced and (b) while it was re-oxidized at 550 °C, 600 °C and 650 °C. $k_{chem}$ values are plotted using the final pO2 value for each relaxation step.
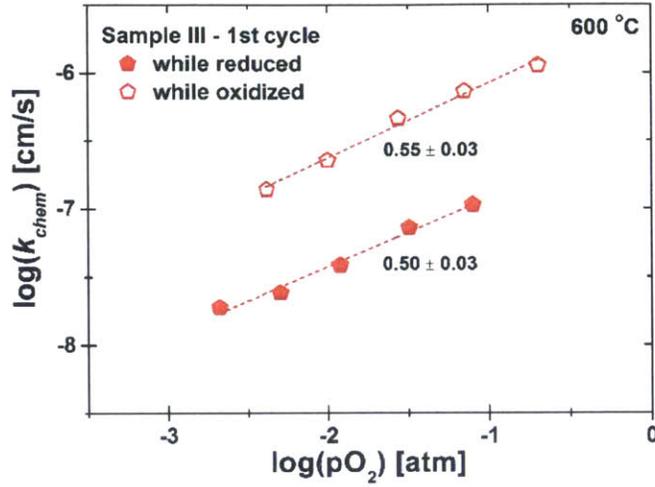
**Figure 24. Plot of $k_{chem}$ from optical relaxation versus $pO_2$ for sample III from 1st cycle of reduction-oxidation at 600 °C. $k_{chem}$ values are plotted using the final $pO_2$ value for each relaxation step.**

### 3.3.2 in-situ EIS results

Figure 25 (a) shows typical impedance spectra obtained for the symmetric cell, 10PCO/YSZ/10PCO (Sample I and III), at 600 °C in air. As shown in the inset, the spectra are represented by a resistor in series with an $R//Q$ circuit ($R//Q$: a resistor in parallel with a constant phase element [CPE]). CPEs are used to take into account any inhomogeneities in the electrodes resulting in "depressed" arcs not well represented by ideal capacitors [67]. An equivalent capacitance was derived from the CPE using the treatment discussed in Reference [80]. The impedance of a constant phase element is given by

$$Z = \frac{1}{Q(i\omega)^n} \tag{26}$$

from which the capacitance is derived using the following equation.

$$C = Q\omega_{max}^{n-1} = (R^{1-n}Q)^{\frac{1}{n}} \tag{27}$$

The equivalent circuit fits are observed to represent the data well. As discussed by Chen et al. [69], $R_1$ reflects the series YSZ ohmic contribution to the overall cell impedance and $R_2$ is the electrode resistance at the PCO/gas interface, limited by oxygen surface exchange kinetics. Lastly, $CPE_2$ is the chemical capacitance ($C_{chem}$) of the PCO film. Typical phase angles for the CPE impedance were $88.6 \pm 1.1$ degrees and thus $CPE_2$ demonstrates near ideal capacitance. Additionally, the relatively large $C_{chem}$

61

values (e.g. 3-35 mF/cm$^2$) are indicative of chemical capacitance, as reported for other thin film MIEC systems [32,68,71].

As shown in Figure 25 (b), the additional arc ($R_3//CPE_3$) between the offset resistance and the large semicircle at low frequencies appeared for the asymmetric cell, 10PCO/YSZ/Ag (Sample II). It shows a pO$_2$ dependent change and is characterized by an activation energy of 0.96 ± 0.01 eV, which is close to literature values (1.02 ~ 1.20 eV) of Ag/YSZ cell when atomic oxygen bulk diffusion through the solid silver is considered as the rate-determining process [81]. In addition, when the symmetric cell with Ag/YSZ/Ag structure was tested, one semicircle with similar shape appeared. It could therefore be attributed to the Ag counter electrode/gas/YSZ electrolyte interface. It should be mentioned that the fitting of the experimentally obtained impedance spectra with the modeled equivalent circuit became difficult when semicircles from PCO and Ag counter electrodes in the complex plot were comparable in the size and overlapped considerably at certain pO$_2$s and temperatures (Figure 26). In some cases, better fitting could be obtained by fitting the semicircles separately. For example, the semicircle from the Ag counter electrode was first fitted with a resistor in series with an R//Q circuit (the circuit model in the inset of Figure 25 (a)). Then, by fixing obtained values for the offset resistance and R and Q for the semicircle from the Ag counter electrode, all the data were fitted with a resistor in series with two R//Q circuits (the circuit model in the inset of Figure 26), in order to extract the R and Q values for the semicircle from PCO electrode. The final fitting result, obtained by following this procedure, is compared with the experimental data in Figure 26. In order to eliminate this kind of fitting difficulty, the use of a reference electrode is recommended, thereby minimizing potential fitting errors.
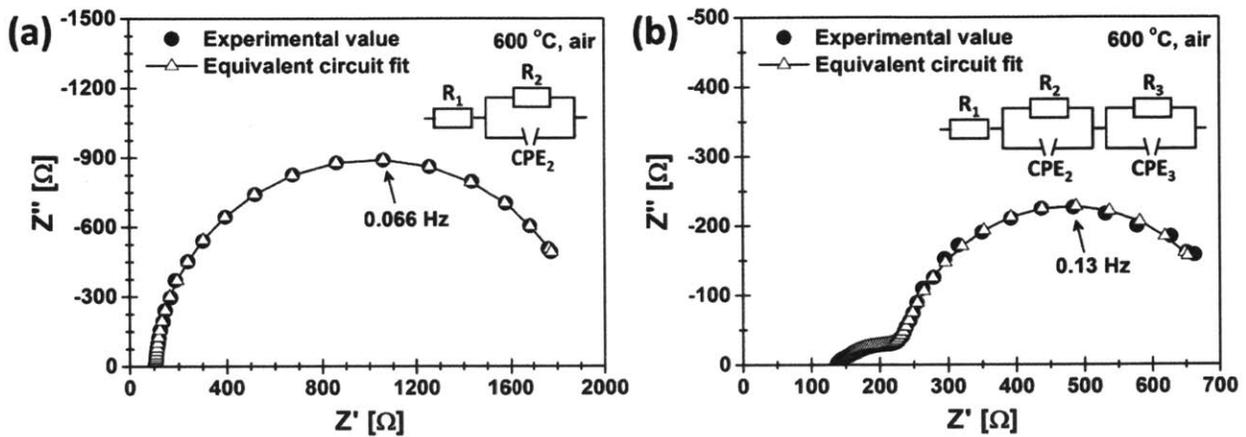
**Figure 25.** Typical impedance spectra in air at 600 °C from (a) symmetric cell PCO/YSZ/PCO and (b) asymmetric cell PCO/YSZ/Ag, with variables defined in the text.
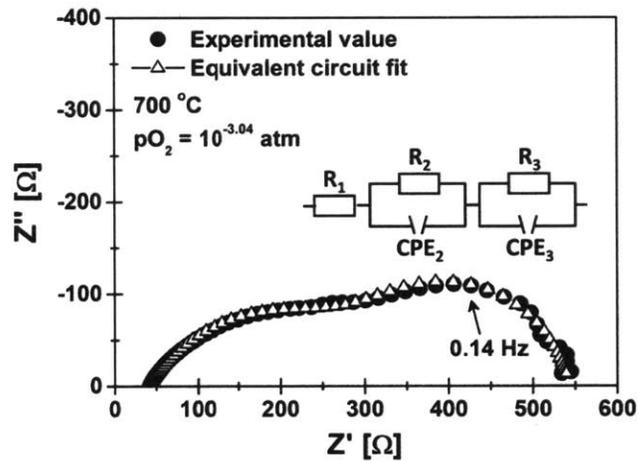


**Figure 26.** Impedance spectra at 700 °C and $\log(pO_2)$ = -3.04 atm obtained from the asymmetric cell PCO/YSZ/Ag, with variables defined in the text.

### *Chemical capacitance ($C_{chem}$) of 10PCO thin film electrode*

In Figure 27, the experimentally obtained $C_{chem}$ values are plotted as a function of $pO_2$. In Figure 27 (a), the filled and empty hexagons indicate $C_{chem}$ values obtained from Sample I, while the sample was being reduced and oxidized, respectively. The filled dots in Figure 27 (b) represent $C_{chem}$ values obtained from Sample II measured at 550 °C – 700 °C, while the empty dots in Figure 27 (c) indicate $C_{chem}$ values obtained from Sample III during 5 time cycles of $pO_2$ step change at 600 °C. The solid curve represents

the calculated values of $C_{chem}$ based on Equation (15) using $[V_O^{\bullet\bullet}]$ values from the defect model with the thermodynamic parameters from Chen et al.'s work [68]. Good agreement between values from the present work and the predicted values is observed for all the Samples, showing that the volume specific $C_{chem}$ values, thermodynamic quantities, do not vary between samples.
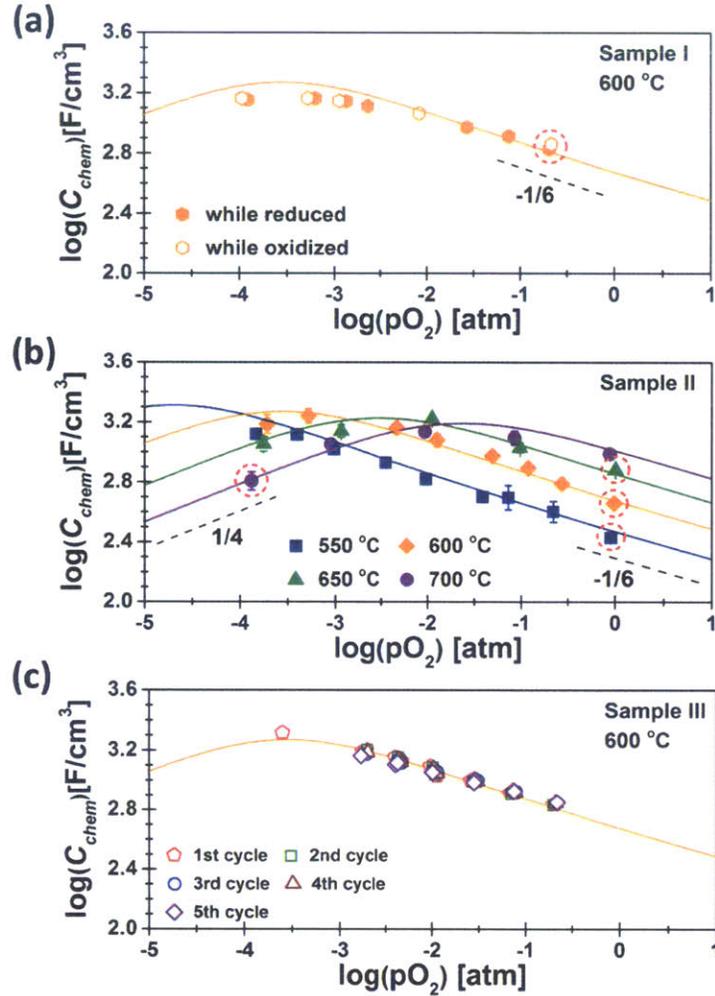


**Figure 27. Isothermal dependence of volume-specific $C_{chem}$ on $pO_2$ for Sample I at 600 °C (a), for Sample II at 550 °C, 600 °C, 650 °C and 700 °C (b) and for Sample III at 600 °C (c). The -1/6 and 1/4 indicate the slopes expected at low $pO_2$ and high $pO_2$ where Equation (17) and (18) are valid, respectively [68]. The red dotted circles indicate capacitances used to derive absolute stoichiometry using Equation (19) and (20). Solid lines represent modeled data from reference [68].**

Following the approach discussed above and in Reference [68], oxygen non-stoichiometry values ($\delta$) for the PCO thin films were extracted from experimentally obtained values for $C_{chem}$ by utilizing Equation (15). The absolute stoichiometry was calculated by using Equation (19) for 550 °C to 650 °C

64

and Equation (20) for 700 °C at pO$_2$ where Equation (17) and (18) are valid, respectively (as indicated

with the red dotted circles in Figure 27). $\delta$ was then used to calculate the Pr$^{4+}$ ion concentration by

Equation (28) obtained by substitution of Equation (13) into Equation (14).

$$[Pr_{Ce}^{\times}] \approx [Pr_{Ce}]_{total} - 2[V_O^{\cdot\cdot}] \qquad (28)$$

The filled and empty dots in Figure 28 show $\delta$ and the Pr$^{4+}$ ion concentration extracted from $C_{chem}$,

respectively, for Sample I (a) and Sample II (b). These results are compared with values calculated by

using a defect model (solid and dotted lines) [68]. The present data agree well with both the magnitude

and temperature/pO$_2$ dependence predicted by the defect model.
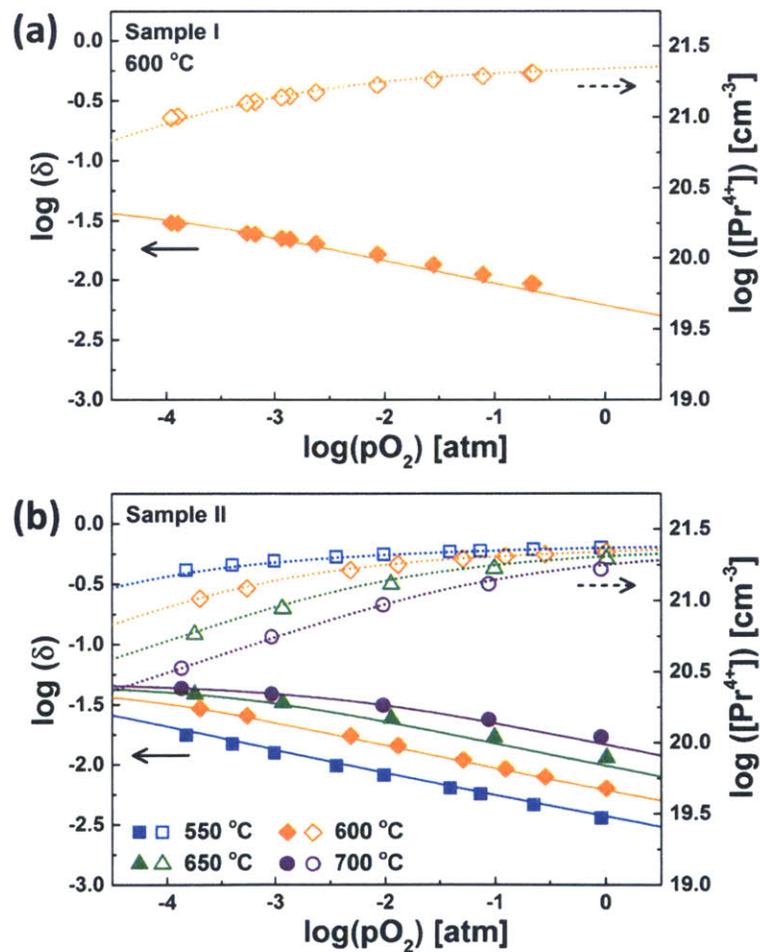


**Figure 28. Nonstoichiometry ($\delta$) and Pr$^{4+}$ ion concentration [Pr$^{4+}$] derived from $C_{chem}$ for Sample I at 600 °C (a) and for Sample II at 550 °C, 600 °C, 650 °C and 700 °C (b). Solid and dotted lines represent modeled data from reference [68].**

*Electrical oxygen exchange coefficient ($k_{elec}$) of 10PCO thin film electrode*

When the surface exchange reaction is the limiting process, the electrical surface exchange coefficient, $k_{elec}$, can be extracted from the measured electrode resistance as follows [29].

$$k_{elec} = \frac{kT}{4e^2 R_s C_O}$$
(29)

where $k$, $T$, $e$, $R_S$ and $C_O$ are Boltzmann constant, temperature, electron charge, area specific resistance (ASR) and total concentration of lattice oxygen ($5.036 \times 10^{22}$ cm$^{-3}$ used in this calculation), respectively.

Figure 29 (a) and (b) show the $pO_2$ dependence of the electrode resistance measured for Sample I and the corresponding $k_{elec}$. The slope, $m$ in the Equation (25), for log $k_{elec}$ vs log $pO_2$ plot, is $1.01 \pm 0.06$ at lower $pO_2$ ($< 10^{-3}$ atm) and $0.29 \pm 0.03$ at higher $pO_2$ ($>10^{-2}$ atm), pointing to a change in reaction mechanism. Overall, there is an approximately a three orders of magnitude change in ASR over the $pO_2$ range examined. This change in $pO_2$ dependence agrees well with Chen et al.'s previous work [69], even given differences in the current collector material; Pt for this work and Au for Chen et al.'s work. The electrode resistance and corresponding $k_{elec}$ values at given $pO_2$s at this temperature (600 °C) changed little during the reduction – oxidation cycle.

Figure 30 and Figure 31 show the $pO_2$ dependence of the electrode resistance and corresponding $k_{elec}$ values for Sample II at 550 °C, 600 °C and 650 °C. Generally, $k_{elec}$ becomes higher when temperature increases, indicating that the governing reaction kinetics are thermally activated. Interestingly, contrary to Sample I, $k_{elec}$ of Sample II goes through maximum values at $pO_2 = 10^{-2} \sim 10^{-3}$ atm, showing negative $pO_2$ dependence at higher $pO_2$ ($m = -0.64 \sim -0.94$) and positive $pO_2$ dependence at lower $pO_2$ ($m = 0.65 \pm 0.06$). This negative $pO_2$ dependence of $k_{elec}$ is also found for Sample III ($m = -0.71 \pm 0.09$) as shown at Figure 32. The $k_{elec}$ maximum shifted to lower $pO_2$ when temperature decreased from 650 °C to 550 °C. In general, $k_{elec}$ at a given $pO_2$ appears to be insensitive to whether obtained during a given reduction or oxidation cycle at each of the temperatures.
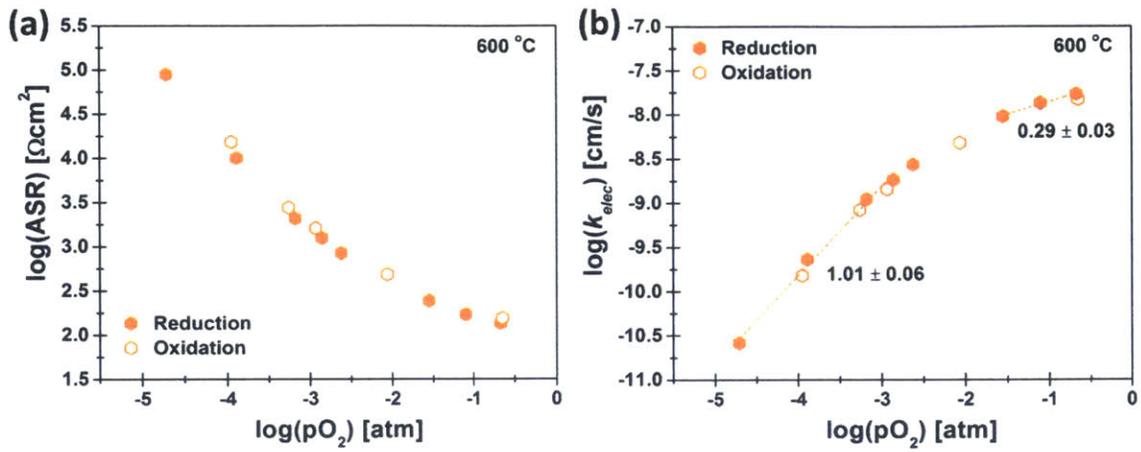
**Figure 29.** Plot of (a) ASR and (b) corresponding $k_{elec}$ derived from EIS measurements versus $pO_2$ for Sample I at 600 °C.
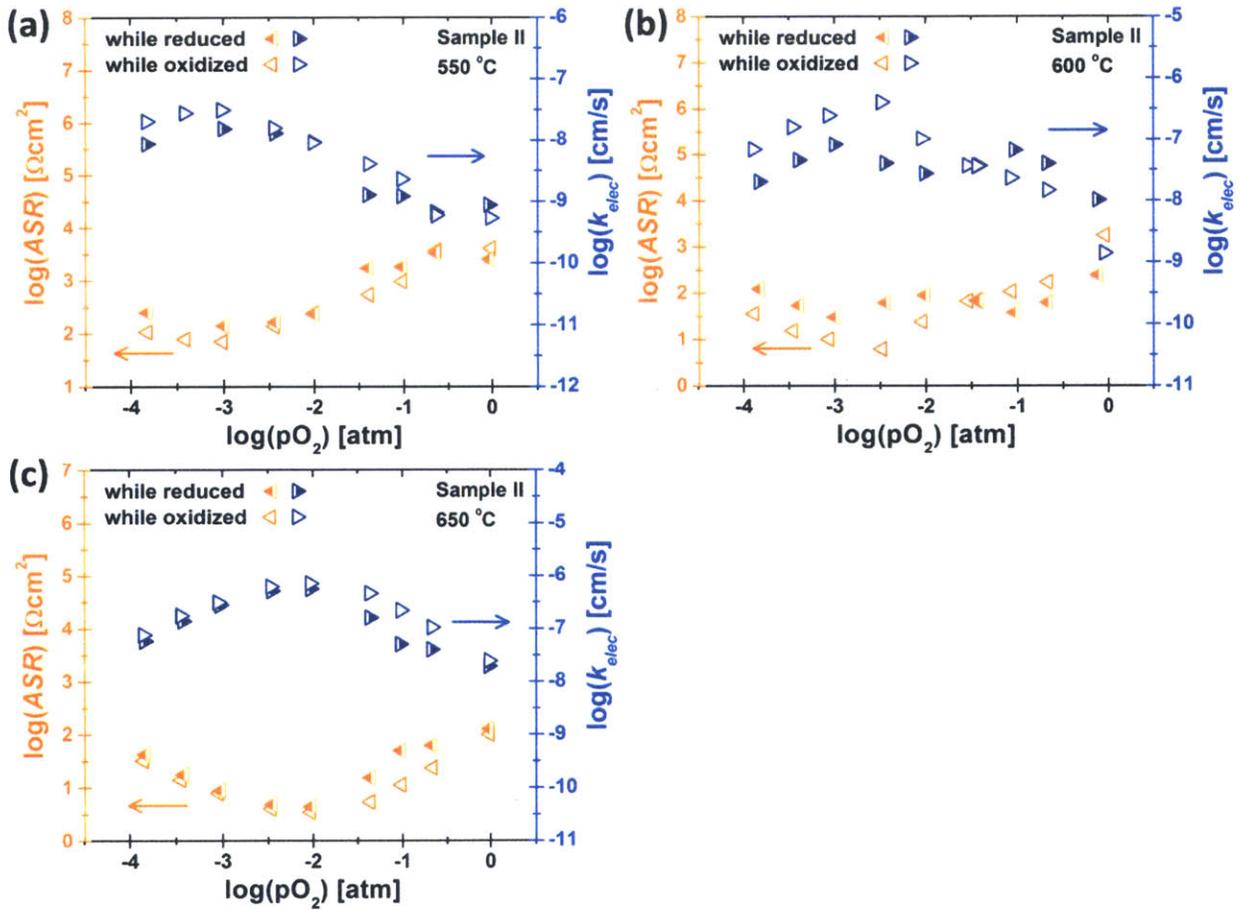


**Figure 30.** Plot of ASR and corresponding $k_{elec}$ derived from EIS measurements versus $pO_2$ for sample II at 550 °C (a), 600 °C (b) and 650 °C (c).
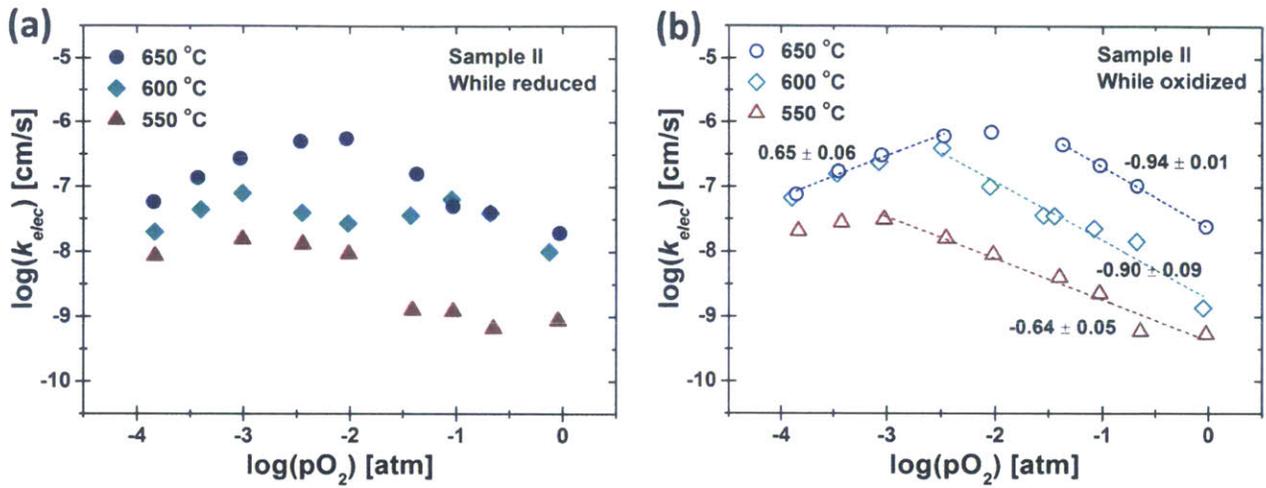
**Figure 31.** Plot of $k_{elec}$ from EIS measurements versus $pO_2$ for sample II (a) while the 10PCO film was being increasingly reduced and (b) while it was being increasingly re-oxidized at 550 °C, 600 °C and 650 °C.
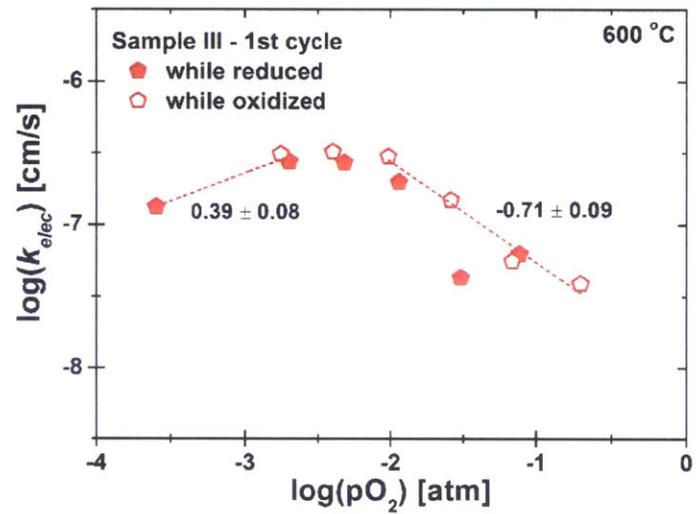


**Figure 32.** Plot of $k_{elec}$ from EIS measurements versus $pO_2$ for sample III from 1st cycle reduction-oxidation at 600 °C.

### 3.3.3 Time dependent change of $k_{chem}$ and $k_{elec}$

Time dependent changes in $k_{chem}$ and $k_{elec}$ were investigated with Sample III by using joint *in situ* optical and EIS measurements. Maintaining the temperature at 600 °C, the sample was subjected to 5 reduction-oxidation cycles. One cycle consists of the reduction and the subsequent oxidation between 0.21 atm and $10^{-3}$ atm of $pO_2$. One step change in $pO_2$ is ~33% of the initial $pO_2$ value. Figure 33 shows the measured $k_{chem}$ from each cycle. For all cycles, $k_{chem}$ from the oxidation step is larger in magnitude than the one from the reduction step. This might be explained by noting that oxygen incorporation into the oxide lattice during oxidation is generally known to require less energy than oxygen vacancy formation requiring the breaking of ionic bonds during the reduction reaction. As summarized in Figure 34 (a), $k_{chem}$ during reduction step increases from the 1$^{st}$ cycle to the 2$^{nd}$ cycle, then $k_{chem}$ for 3$^{rd}$ cycle becomes similar as the one for the 1$^{st}$ cycle. Eventually, $k_{chem}$ decrease slightly during the 4$^{th}$ and 5$^{th}$ cycles by a factor of 3~4 times compared to the one with the largest magnitude (2$^{nd}$ cycle). On the other hand, $k_{chem}$ during oxidation step keeps decreasing in magnitude from the 1$^{st}$ to the 5$^{th}$ cycle by about a factor of 5 (Figure 34 (b)). The power law dependence of $k_{chem}$ with $pO_2$ shows similar positive values ($m = 0.44 \sim 0.61$) for both reduction and oxidation steps (Figure 34). In the case of $k_{elec}$, as shown in Figure 35 and Figure 36, the decrease from values in the 1$^{st}$ cycle to ones in the 5$^{th}$ cycle is a factor of $1.5 \sim 2.5$, which is a relatively smaller change than the ones observed for $k_{chem}$, while all cycles of reduction-oxidation show a negative $pO_2$ dependence ($m = -0.66 \sim -0.76$) in the high $pO_2$ regime while $k_{elec}$ reaches a maximum at around $10^{-2.5}$ atm.
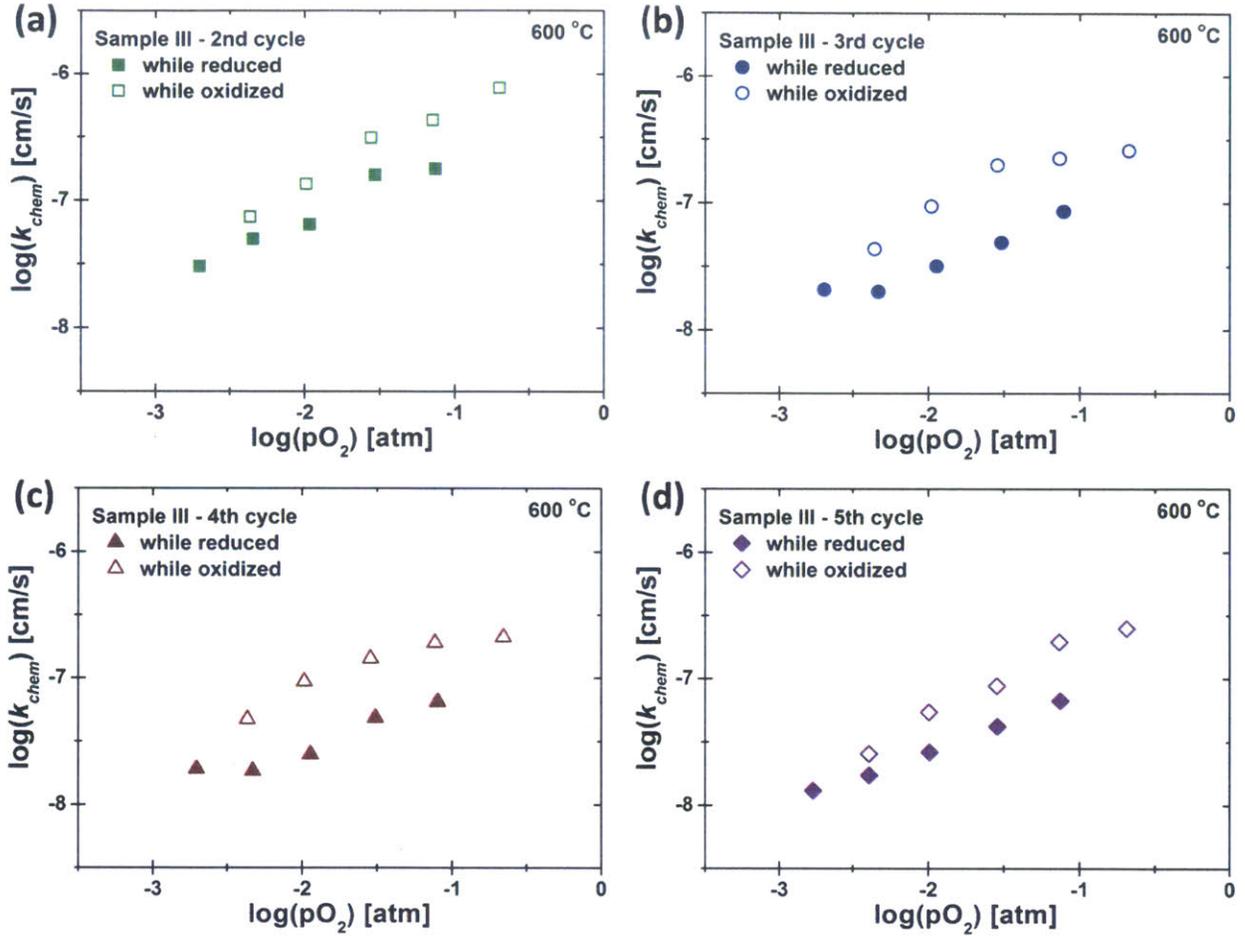
**Figure 33.** Plot of $k_{chem}$ from optical relaxation versus pO$_2$ for sample III at 600 °C from 2$^{nd}$ to 5$^{th}$ annealing cycle (a ~ d). $k_{chem}$ values are plotted using the final pO$_2$ value for each relaxation step.
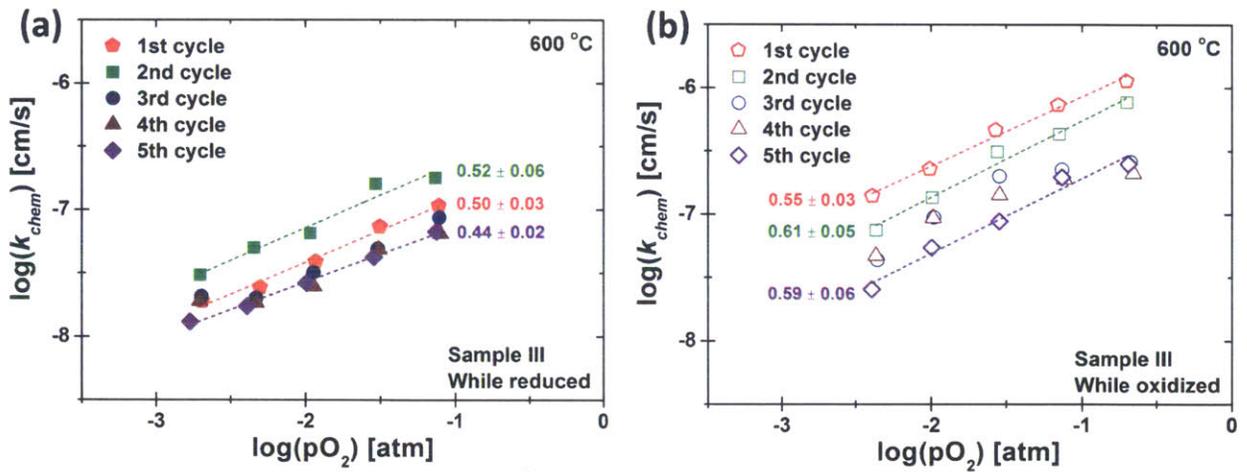


**Figure 34.** Plot of $k_{chem}$ from optical relaxation versus pO$_2$ for sample III during sequential annealing cycles with pO$_2$ step change at 600 °C. $k_{chem}$ values are plotted using the final pO$_2$ value for each relaxation step.
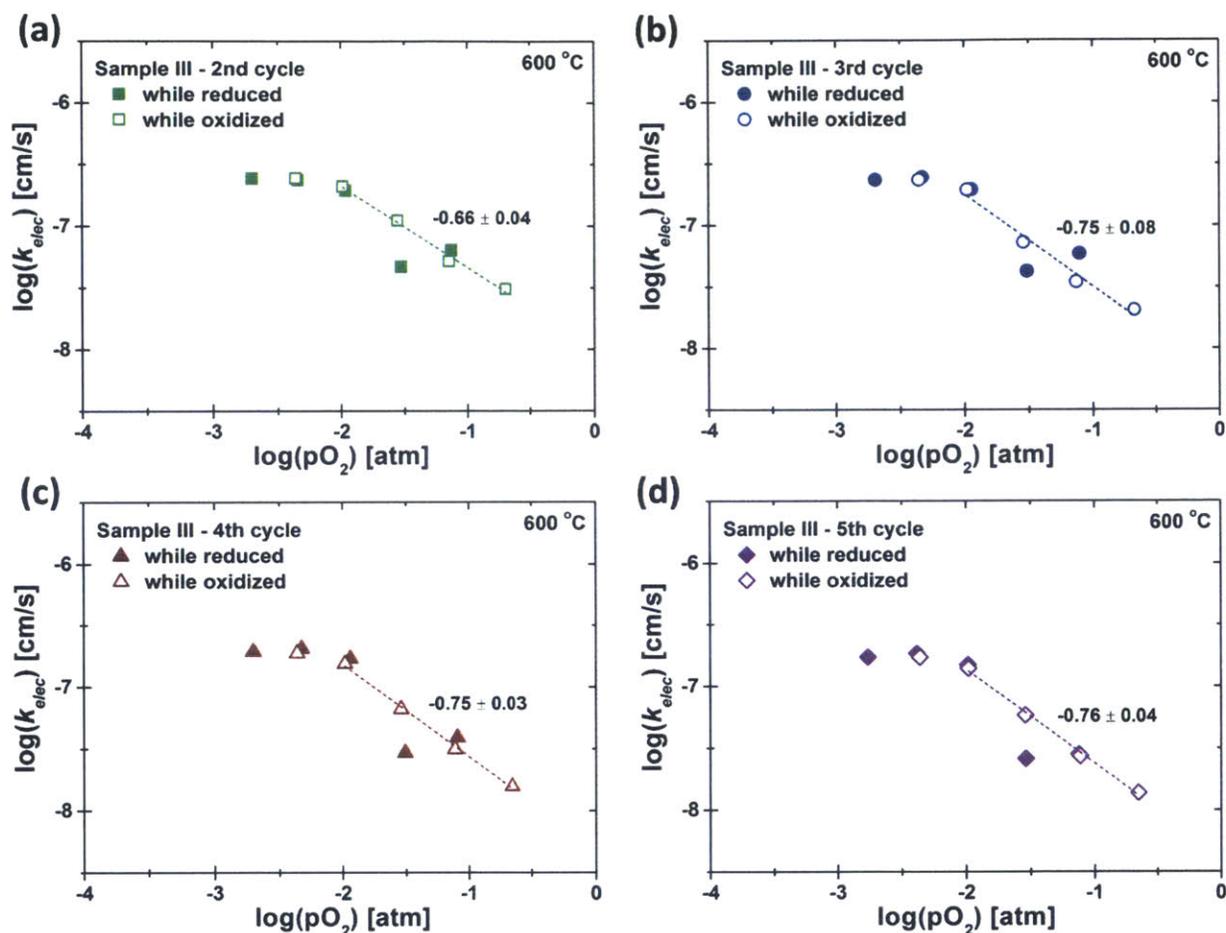
**Figure 35.** Plot of $k_{elec}$ from EIS measurement versus pO2 for sample III at 600 °C from 2nd to 5th annealing cycle (a ~ d).
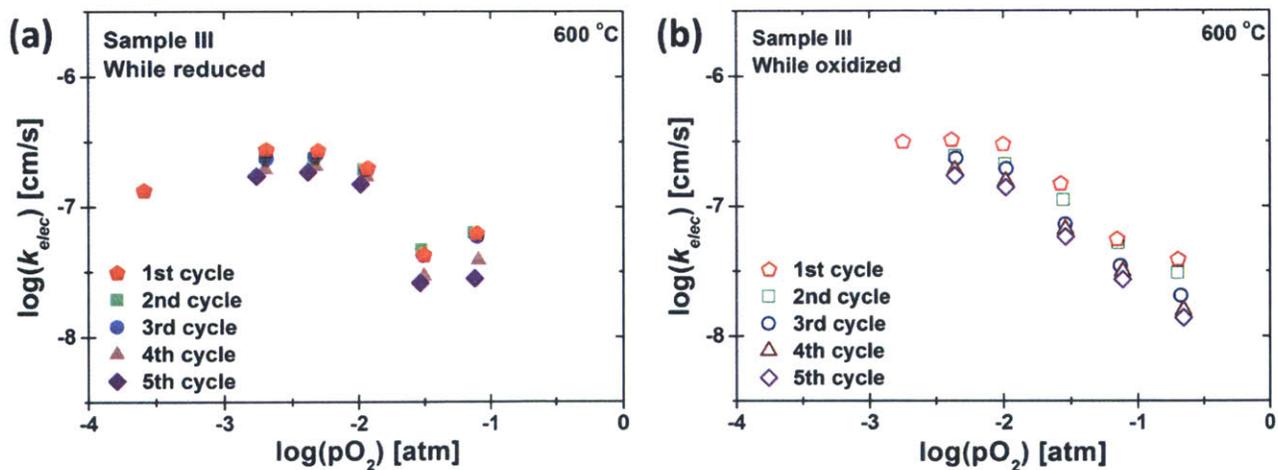


**Figure 36.** Plot of $k_{elec}$ from EIS measurement versus pO2 for sample III during sequential annealing cycles with pO2 step changes at 600 °C.

### 3.4 Surface chemical and morphological properties of PCO thin films

#### 3.4.1 XPS results

##### Impurities on the PCO surface

The chemical composition of an as-deposited 10PCO film and of Sample I, II and III, which were annealed at 600 °C for joint *in situ* optical and EIS measurement, was investigated by means of XPS, known to be extremely sensitive to the near-surface region (Table 3). No specific impurity (other than carbon) was found on the as-deposited PCO film, with only peaks for carbon and oxygen obtained, as normally present on samples exposed to the atmosphere (Figure 37). However, an appreciable amount of Na and Si was found on the surface of Samples I and II which were used for joint *in situ* optical and EIS measurement. Surprisingly, no peaks relating to Ce and Pr were found at the surface of Sample II, while peaks for C and O were intense, indicating high concentration of carbonate related impurities at the surface (Figure 37). The Na1s peak is usually accompanied by strong Auger peak, Na KLL peak. In the XPS spectra shown in Figure 37, it appears at ~492 eV, given that its binding energy results from the kinetic energy (990 eV [82]) and the work function of the instrument (~5 eV) subtracted from the excitation energy (1487 eV). Contrary to Sample I and II, a considerable amount of Bi was found on the PCO film surface of Sample III, while Na and Si impurities were not detected (Figure 38). The Bi (4f$_{7/2}$) peak in XPS spectra is found around 159 eV, very close to the position of the Bi peak in Bi oxide, 159.2 eV. For metallic Bi, the peak position is significantly lower, 157 eV. Therefore, it can be concluded that Bi exists in its oxide form.

In order to find out the origin of the impurities, XPS measurements were performed on the pastes/inks used when preparing the sample for EIS measurements; platinum, silver and ceramic pastes/inks. The impurities found are summarized in Table 4. A large amount of Na was found in the Ag paste, while Bi and Na were found in the reactive Pt paste. In order to compare with the reactive Pt paste used in this study, other types of Pt paste (nominally pure Pt paste) was also investigated. In the nominally

pure Pt paste, Bi and Na were still found, but lower amounts compared to the reactive Pt paste. From the ceramic paste, Si and Na were found.
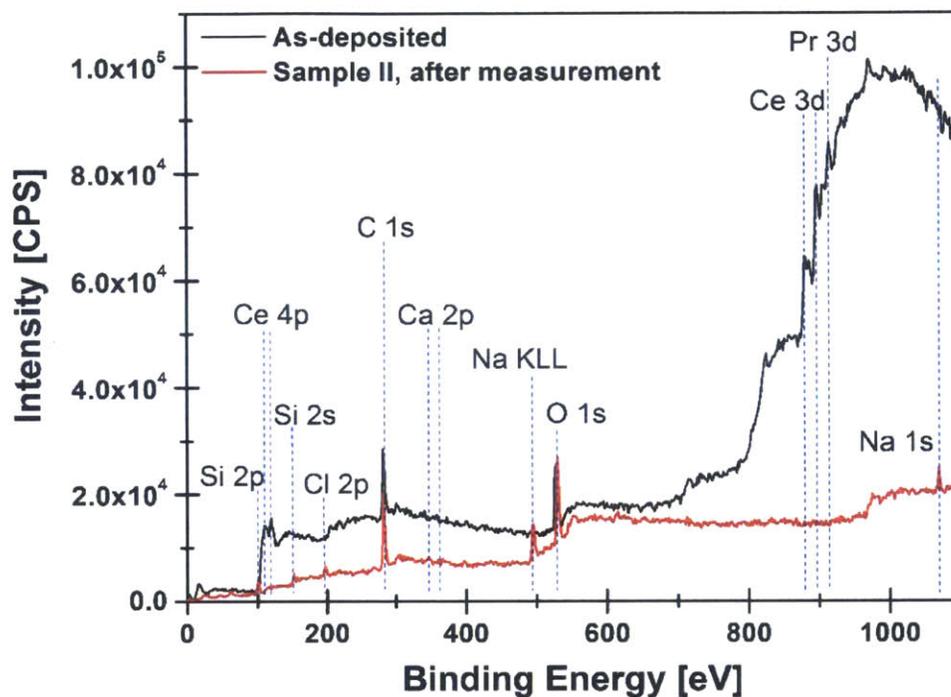


**Figure 37. XPS spectra for annealed PCO film of Sample II at 600 °C for joint *in situ* optical and EIS measurement.**

**Table 3. Chemical composition (cations) obtained from as-deposited 10PCO film, Sample I, II and III after annealing for joint *in situ* optical and EIS measurements. The unit for atomic concentration is percentage.**

|             | Ce   | Pr   | Bi   | Na   | Si   | Ca   | Pr/(Pr+Ce) |
|-------------|------|------|------|------|------|------|------------|
| As-deposited| 73.0 | 27.0 | -    | -    | -    | -    | 0.27       |
| Sample I    | 21.5 | 8.8  | 2.1  | 15.0 | 52.6 | -    | 0.29       |
| Sample II   | -    | -    | -    | 51.0 | 34.0 | 15.0 | -          |
| Sample III  | 50.0 | 18.0 | 32.0 | -    | -    | -    | 0.26       |
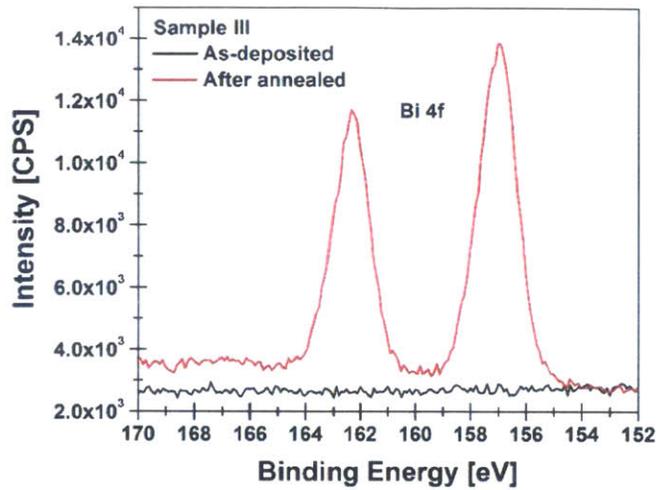
**Figure 38. Bi spectra for as-deposited and annealed PCO films of Sample III after 5 cycles of reduction-oxidation at 600 ºC.**

**Table 4. Chemical composition (cations) obtained from pastes used in this study for sample preparation. The pure Pt paste was investigated for comparison. The unit for atomic concentration is percentage.**

|  | Ag | Pt | Si | Na | Bi |
|---|---|---|---|---|---|
| Ag paste | 85.0 | - | - | 15.0 | - |
| Reactive Pt paste | - | 76.0 | - | 9.0 | 15.0 |
| Ceramic paste | - | - | 50.0 | 50.0 | - |
| Pure Pt paste | - | 96.0 | - | 1.0 | 3.0 |
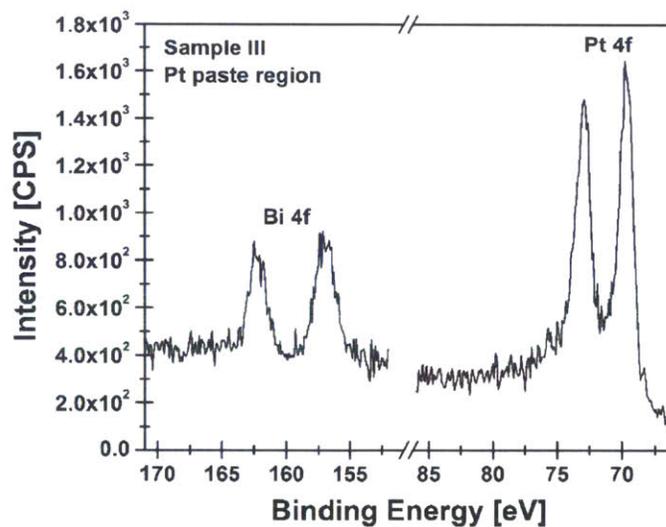


**Figure 39. Pt and Bi spectra at the Pt paste region for the annealed PCO film of Sample III after 5 cycles of reduction-oxidation at 600 ºC.**

74

*Bi diffusion from Pt paste*

The depth profile of the chemical composition (Figure 40 (a)), generated by sputtering the sample surface, confirms that Bi exists at the surface. The atomic concentration of Bi reaches approximately 65 % at the surface and drops to about zero after removal of approximately 0.9 nm of the surface layer. However, the Bi concentration never reaches zero following further sputtering. At this moment, the origin of a very small Bi trace even after sputtering is unclear. It might come from Bi surface migration from unsputtered to sputtered regions during measurement, which sometimes happens for carbon. The Pt paste, which was applied as a current collector for EIS measurements on half of the PCO surface, was revealed as the Bi source. In addition to the fact that Pt paste contains Bi (Figure 39 and Table 4), the position dependent chemical composition profile across the sample shows that the atomic concentration of Bi decreases from 60 % near the Pt paste region (~0.94 mm apart) to 20 % far from Pt paste region (~3.84 mm apart) (Figure 40 (b)).
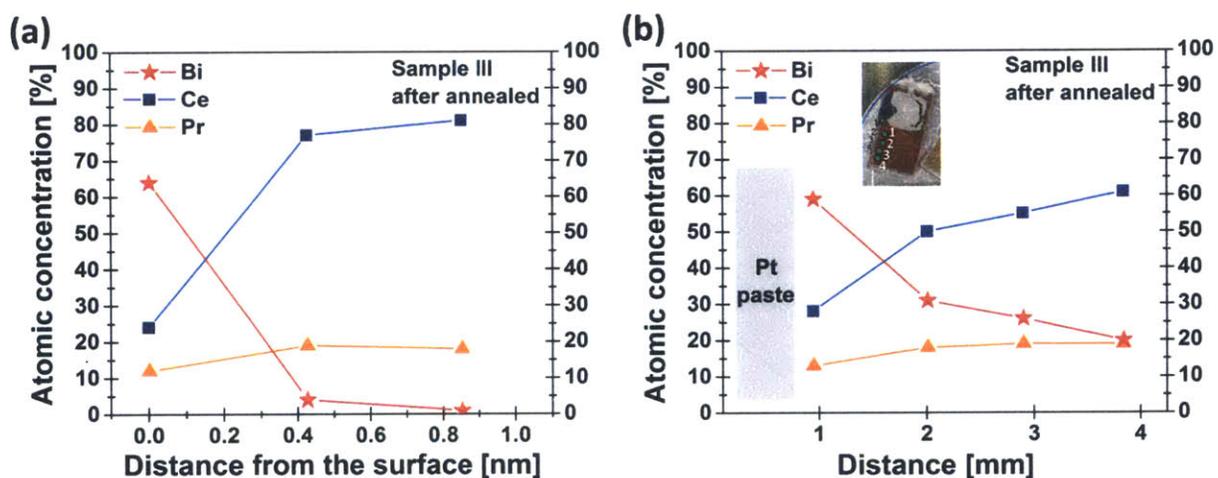


**Figure 40. Compositional depth (a) and position (b) profile of the chemical composition obtained by XPS from Sample III after annealed for 5 cycles of reduction-oxidation at 600 °C.**

*Chemically etched surface*

The surfaces of Sample II and III were chemically etched with aqueous acid solutions. Only the open surface used for the optical measurements was subjected to chemical etching. After being etched in HCl solution (0.14 M) for 20 seconds, most of the Bi, Na and Ca was successfully removed (Table 5).

Interestingly, for Sample II, the Pr, Ce and Bi peaks, not visible before, appeared, while Si still remained, showing ~89% of atomic concentration. After Sample II was etched in HF solution (1 : 9 = HF : DI water) for 30 seconds, the Si peaks disappeared in the XPS spectra while small traces of F were observed. After etching, the ratio of Pr to (Pr+Ce) was ~0.15.

**Table 5. Chemical composition (cations) obtained from Sample II and III after acid etching. The unit for atomic concentration is percentage.**

|  | Etchant | Ce | Pr | Bi | Na | Si | Ca | Pr/(Pr+Ce) |
|---|---|---|---|---|---|---|---|---|
| Sample II | HCl | 0.4 | 1.5 | 2.7 | 6.5 | 89.0 | - | 0.79 |
|  | HF | 85.0 | 15.0 | - | - | - | - | 0.15 |
| Sample III | HCl | 80.3 | 19.7 | < 0.5 | - | - | - | 0.20 |

*Pr segregation on the PCO thin film surface*

The chemical composition analysis by XPS revealed that the ratio of Pr to (Pr + Ce) is 0.26 ~ 0.32 at the film surface, considerably higher than the nominal value, 0.10, for the film. Interestingly, the as-deposited film also shows Pr segregation near the surface. The depth profile of the ratio of Pr to (Pr + Ce) showed that Pr-rich layer is approximately 10 nm thick.
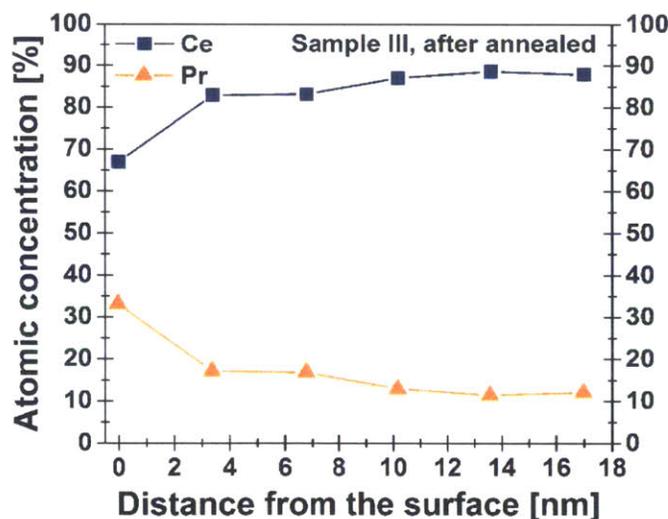


**Figure 41. Depth dependent ratio of Pr to (Pr + Ce) obtained from Sample III after annealed for 5 cycles of reduction-oxidation at 600 °C.**

*3.4.2 AFM results*

The surface morphological characteristics of the films were investigated by atomic force microscopy (AFM). Areas of $1 \times 1$ $\mu m^2$ and $5 \times 5$ $\mu m^2$ were scanned at several points of the sample to insure that the images represent the film's properties well. A root-mean-square (RMS) surface roughness was calculated after averaging several different measurements on the same film.

The 10PCO thin film deposited at 700 °C onto a YSZ single crystal substrate, depicted in Figure 42, shows very flat and a highly smooth surface with a RMS surface roughness of 0.70 ± 0.30 nm. The grain sizes were estimated to fall within the range of 20 - 40 nm. As shown in Figure 42 (b) for a wider area, the as-deposited film has a mainly particle-free surface. On the other hand, the surface of the 10PCO thin film of Sample II (Figure 43), annealed during joint *in situ* optical and EIS measurement at 600 °C, is covered with particles, and its RMS surface roughness increases to 4.13 ± 1.38 nm. After being etched in HF solution (1: 9 = HF : DI water) for 30 seconds, the RMS surface roughness (3.77 ± 0.13 nm) of Sample II is not altered much, while its morphology shows a distinct change (Figure 44).

Interestingly, the surface of Sample III shows a position dependent morphology as shown in Figure 45. At an area close to the Pt paste region, applied as current collector for EIS measurement, patch-like features with approximately 200 nm width and 5 nm height appear, with a RMS surface roughness of 0.79 ± 0.46 nm. On the other hand, at regions far from the Pt paste, smaller particles with smaller width (20 ~ 50 nm) but larger height (10 ~ 20 nm) are observed, with the RMS surface roughness increasing to 2.08 ± 1.31 nm. The middle region combines morphological characteristics of the two ends, with a RMS surface roughness (1.66 ± 0.97 nm) that also falls between the two end values.
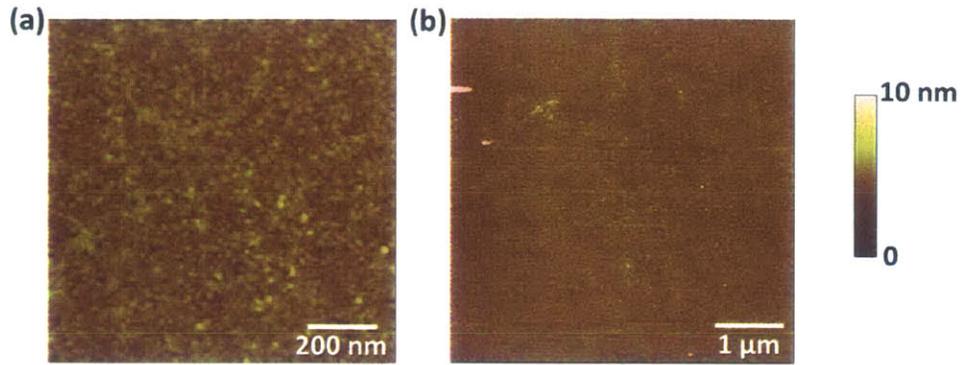
**Figure 42. Typical AFM micrograph of as-deposited 10PCO film surface deposited at 700 °C on a YSZ single crystal substrate for scanned area of $1 \times 1$ µm$^2$ (a) and $5 \times 5$ µm$^2$ (b).**
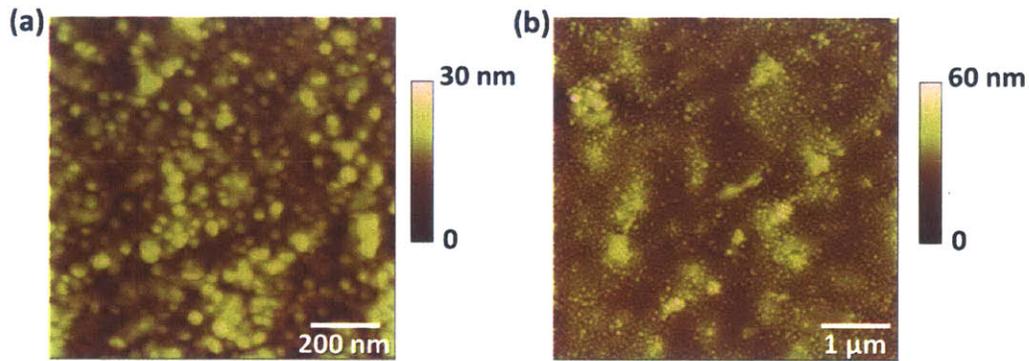


**Figure 43. Typical AFM micrograph of 10PCO film surface of Sample II after annealed during joint *in situ* optical and EIS measurement at 600 °C for scanned area of $1 \times 1$ µm$^2$ (a) and $5 \times 5$ µm$^2$ (b).**
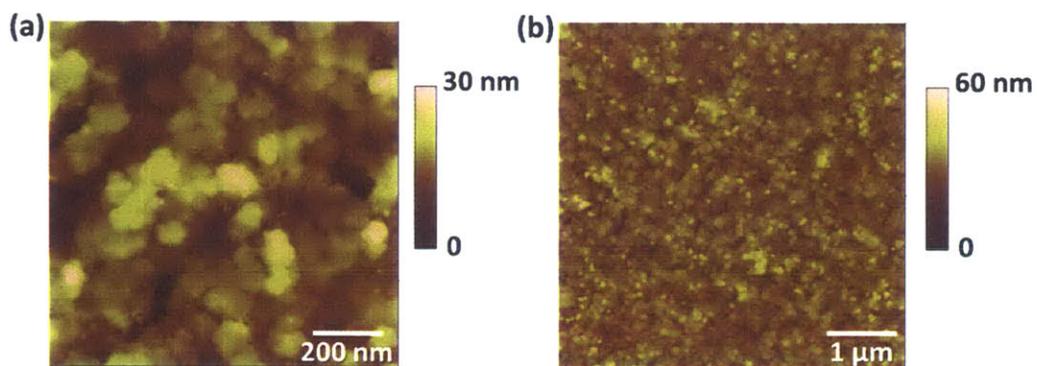


**Figure 44. Typical AFM micrograph of HF etched 10PCO film surface of Sample II, which was used for joint *in situ* optical and EIS measurement at 600 °C, for scanned area of $1 \times 1$ µm$^2$ (a) and $5 \times 5$ µm$^2$ (b).**
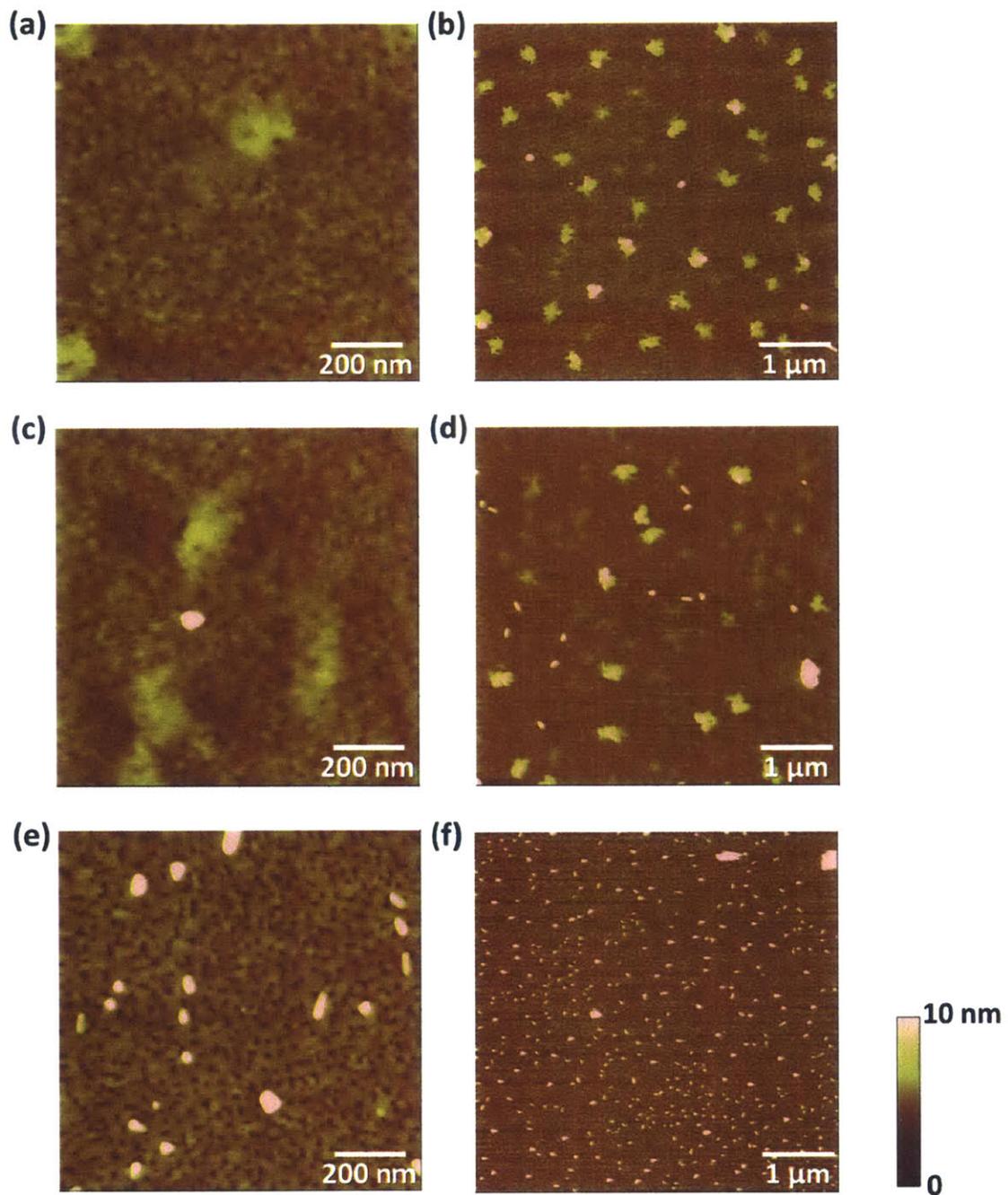
**Figure 45.** AFM micrograph of 10PCO film surface of Sample III after annealed during joint *in situ* optical and EIS measurement at 600 °C for scanned area of $1 \times 1$ μm$^2$ (a, c, e) and $5 \times 5$ μm$^2$ (b, d, f). (a) and (b) are close to Pt paste region, (c) and (d) are center of the opened PCO area, and (e) and (f) are far from Pt paste region.

### 3.4.3 AES results

The chemical composition of particles found at the annealed film surface of Sample III was investigated by Auger Electron Spectroscopy (AES), which is able to quantify atomic concentrations with nm-scale spatial resolution. As indicated in Figure 46, the particle (position 1) and the particle-free surface (position 2) were subject to the Auger spectrum scan. Because the PCO film was not conducting enough, the focus drifted slightly during the AES measurement. As summarized in Table 6, the particle consists mainly of Bi, while the particle-free surface still shows an appreciable concentration of Bi. Small perhaps inadvertent traces of Pr and Ce picked up in the particle may result from beam drift.
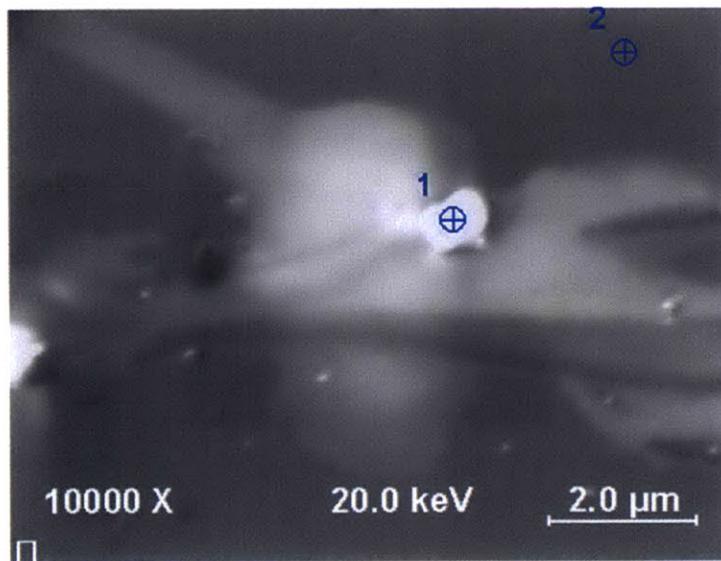


**Figure 46. The SEM image of the region for Auger spectrum scan. Position 1 and 2 indicate the particle and the surface of 10 PCO thin film of Sample III after annealing for joint *in situ* optical and EIS measurement.**

**Table 6. Chemical composition obtained from the particle (point 1) and the surface (point 2) of 10 PCO thin film of Sample III after annealing for joint *in situ* optical and EIS measurement. The unit for atomic concentration is percentage.**

| Point | Ce | Pr | Bi |
|-------|------|------|------|
| 1 | 3.4 | 5.0 | 91.6 |
| 2 | 39.6 | 38.5 | 21.9 |

### 3.4.4 $k_{chem}$ after chemically etching the surface

In order to investigate the impact of surface impurities on the surface exchange reaction kinetics, the optical transmittance relaxation of the Sample II, following etching in HF solution, was monitored during reduction and re-oxidation at 600 °C. In order to be isolated from any contamination from the Pt current collector and ceramic paste, the part of the substrate used for the optical measurement was separated by cutting it from the part used for EIS measurement. As shown in Figure 47, $k_{chem}$ increases by 1 or 2.5 orders of magnitude (depending on pO$_2$) following removal of the impurity layer by etching. Furthermore, a stronger pO$_2$ dependency for $k_{chem}$ is recovered.
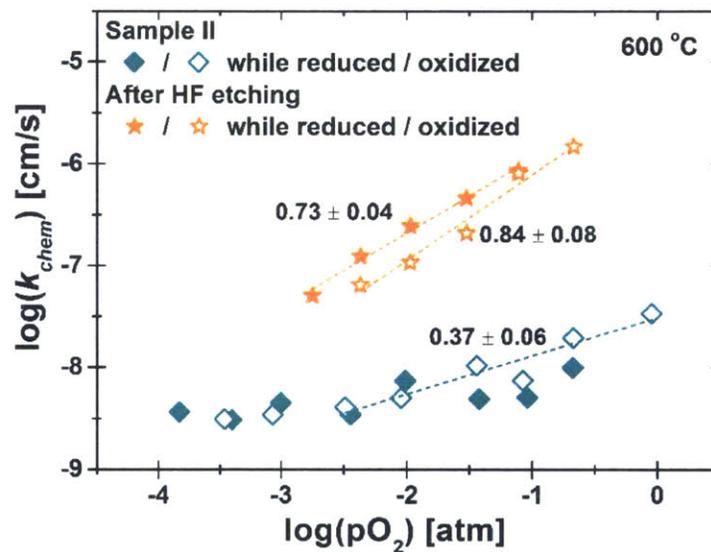


**Figure 47.** $k_{chem}$ **versus pO$_2$ of Sample II at 600 °C during joint** *in situ* **optical and EIS measurement and optical measurement after HF etching (1: 9 = HF : DI water) for 30 seconds.**

## 3.5 Color front motion in PCO thin films

### 3.5.1 Diffusion profile

In this series of experiments, an oxygen-blocking layer of MgO was deposited onto the PCO film to limit oxygen ingress and exit into or out of the film to its edges or at a scratch through the film (see section 2.5.1 for details). In this manner, it becomes possible to monitor the diffusion of oxygen along the film plane by following, for example, the respective color front motion associated with the oxidation. Figure 48 demonstrates the process of extracting oxygen chemical diffusion profiles from the collected optical micrographs.
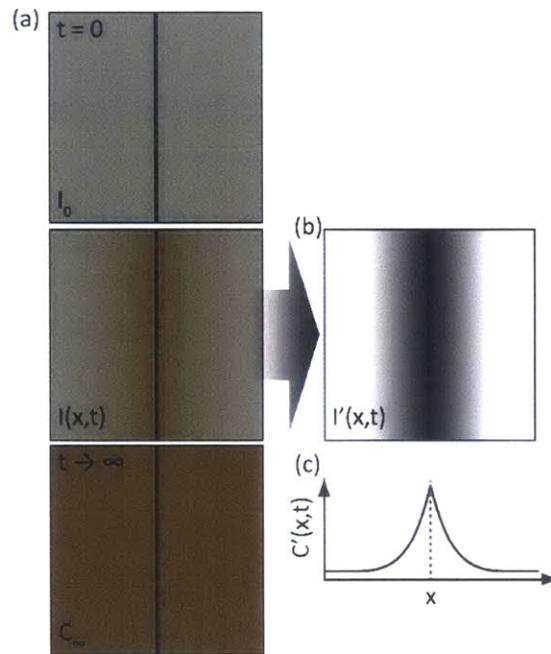


**Figure 48. Schematic representation of an optical micrograph in a region surrounding an exposed area of sample, together with reference micrographs (a) used to isolate the intensity change due to changes in Pr oxidation state (b) and subsequently extract diffusion profiles conforming to a 1D diffusion model (c)**

In order to establish reference equilibrium states in the two gases used, two micrographs were identified to act as reference images, one representing the Pr oxidation state at equilibrium with the conditions prior to the gas change (t = 0) and one to act as the fully equilibrated Pr oxidation state after the gas change (t → ∞), as shown in Figure 48 (a). A linear relationship between pixel intensity and Pr oxidation state was assumed between these points, and each collected micrograph could be used to extract

82

a diffusion profile at time (t) of its collection. The intensity of each pixel ($I(x,t)$ in coordinate space, $x$, and at time, $t$) in the image of interest is converted to a point on this linear relationship as follows:

$$I'(x,t) = \frac{I(x,t) - I_0}{I_\infty - I_0} \qquad (30)$$

where $I_0$ is the intensity of the pixel in the initial reference image ($t = 0$) and $I_\infty$ is the fully equilibrated final intensity ($t \rightarrow \infty$). The resulting images can be represented as difference maps. In order to convert the intensity of each pixel to a spatially resolved oxygen vacancy concentration map, $C(x,t)$, the corresponding concentration at equilibrium with each gas (and therefore present in each reference image) must be known ($C_0$ and $C_\infty$) and is then calculated as follows:

$$C(x,t) = I'(x,t) \times (C_\infty - C_0) + C_0 \qquad (31)$$

In order to identify pertinent information such as the chemical diffusion coefficient ($D_{chem}$) and surface exchange coefficient ($k_{chem}$), diffusion profiles away from the exposed edge are extracted. First the concentration map is rotated such that the edge of the exposed sample region is aligned with one axis and the data is subsequently averaged along that axis. This significantly reduces the noise in the data. The edge of the exposed sample region is identified and set as $x = 0$ and the diffusion profile where $x > 0$ is fitted to the one dimensional solution of the diffusion equation in a semi-infinite medium, as solved by Crank [83]:

$$C(x,t) = \left[\frac{x}{2\sqrt{Dt}}\right] - \left[\exp\left(\frac{kx}{D} + \frac{k^2 t}{D}\right)\right] \times erfc\left(\frac{x}{2\sqrt{Dt}} + k\sqrt{\frac{t}{D}}\right) \qquad (32)$$

The fitting is performed by a custom linear least squares regression script in Matlab with $D$ and $k$ as the fitting parameters.

In some cases, a color front was found to form and grow radially from a point in the film thought to be covered by the MgO blocking layer. These were attributed to the presence of pinholes in the MgO film. In this case the diffusion profile was extracted by an identical method, save the averaging along one axis and the 2-dimensional data sets were fit to a corresponding 2-dimensional solution of the diffusion equation from a point source in a polar coordinate system, as follows [83]:

$$C(x,t) = \frac{A}{\sqrt{4\pi Dt}} \times \exp\left(-\frac{x^2}{4Dt}\right) \tag{33}$$

The fitting was once again performed by a custom linear least squares regression script in Matlab with the scaling factor ($A$), $D$ and the origin of the coordinate system, and hence the location of the pinhole, as fitting parameter. While the surface exchange coefficient, $k$, will control the scaling factor ($A$), the lack of knowledge of the surface area exposed by the pinhole prevents extracting this parameter from the data.
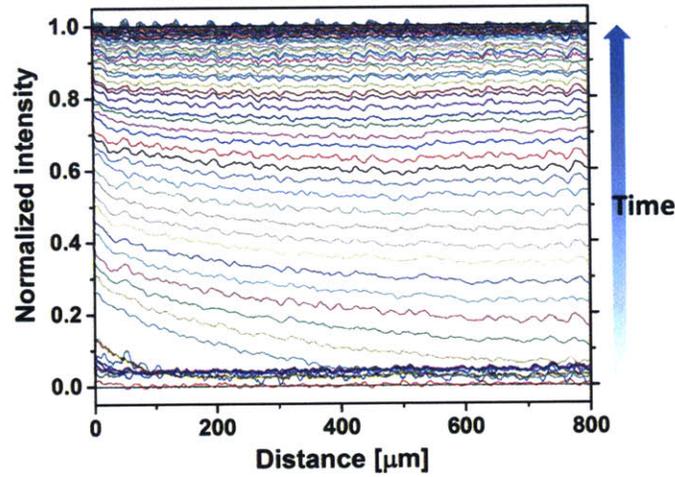


**Figure 49. Plot of normalized intensity vs. distance from the exposed edge (x=0) with time. The measurement was done at 548 °C after changing gas atmosphere from 1000 ppm H$_2$/Ar to O$_2$.**

Figure 49 shows the spatial and time resolved intensity change of color in a 10PCO thin film, obtained by following the method described above. The sample was annealed at 1000 ppm H$_2$/Ar mixture at 548 °C, so it showed no absorption or color due to negligible Pr$^{4+}$ concentration. After switching the gas to O$_2$ (oxidized condition), the exposed edge to the gas atmosphere at x=0 began to show an increase in color intensity due to an increase in [Pr$^{4+}$] resulting from the oxygen surface exchange reaction. After a sufficient time, the film was oxidized along the full sample length, mediated by oxygen diffusion. Figure 50 shows the spatial color intensity profiles in the treated 10PCO thin film at given times at different temperatures. The oxygen transport kinetic parameters, $D_{chem}$ and $k_{chem}$, were extracted by fitting these profiles to the 1-D solution of the diffusion equation applied to a semi-infinite medium (Equation 32). As shown in Figure 50, the color intensity profiles are well represented by the 1-D diffusion profiles.
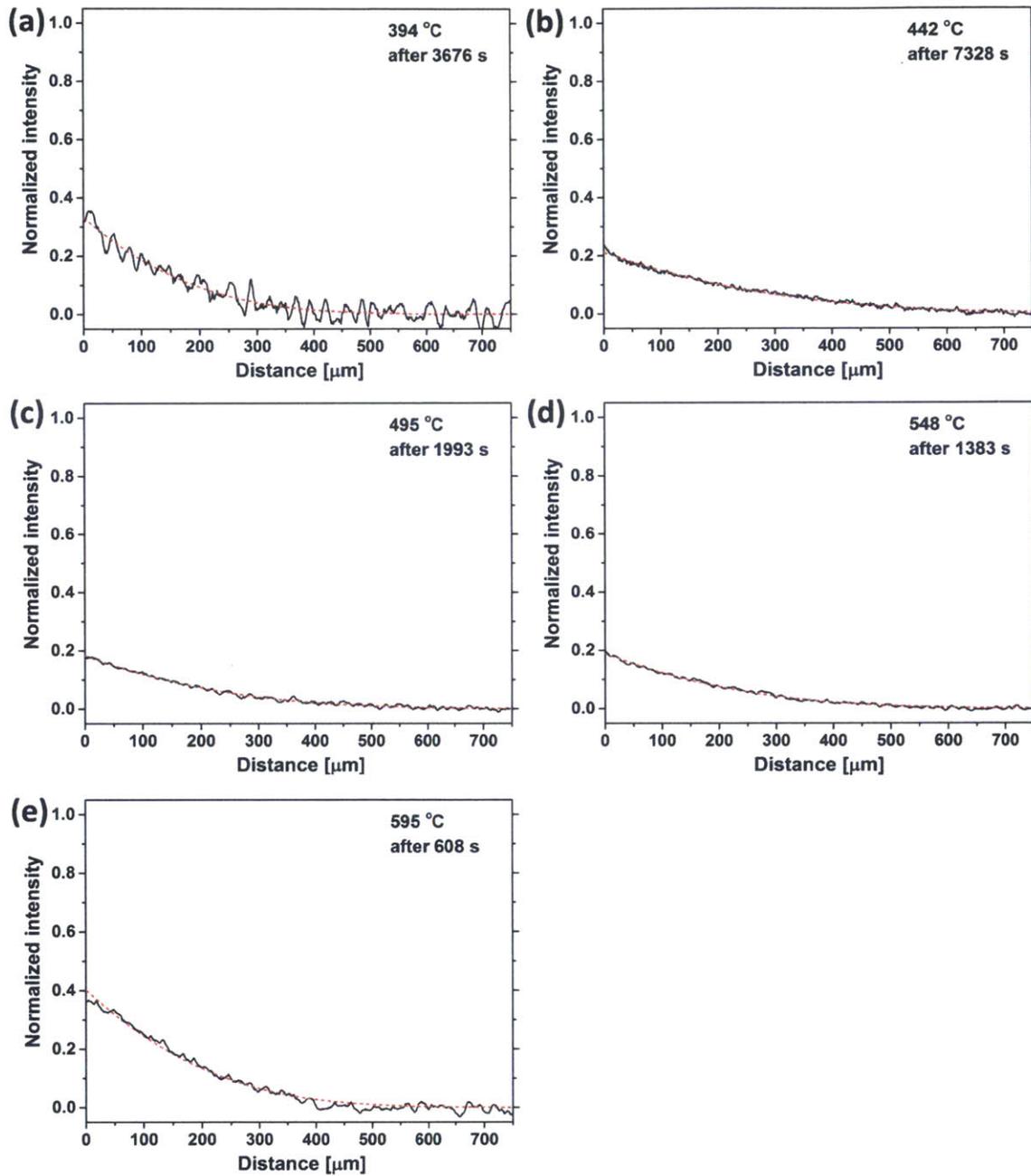
**Figure 50.** Plot of normalized intensity vs. distance from the exposed edge (x=0) with time. The measurement was done at 394 ~ 595 °C (a) ~ (e) after changing gas atmosphere from 1000 ppm $H_2$/Ar to $O_2$. The black solid and the red dotted lines represent experimental data and fitting curves, respectively.

## 3.5.2 Chemical diffusion and surface exchange coefficients

Figure 51 summarizes $D_{chem}$ and $k_{chem}$ values extracted, with the aid of Dr. Stuart N. Cook in our group, from color front motion experiments in 10PCO thin films during an oxidation step (1000 ppm $H_2$/Ar to $O_2$). From these Arrhenius plots, the activation energies of the thermally activated processes could be calculated. The activation energy for chemical diffusion was found to be $0.47 \pm 0.05$ eV. This value is close to that for small polaron hopping through Pr ions ($E_a = 0.56 \pm 0.04$ eV in 10PCO [65]) and suggests that oxygen chemical diffusion in PCO film may be limited by minority electronic transport. While the large $pO_2$ step change imposed during the color front experiment was useful in obtaining a clear and distinctive color contrast between the oxidized and reduced state, this wide oxygen activity jump covered several defect regimes with different possible limiting transport mechanisms. Thus further investigation, utilizing smaller oxygen activity jumps is required to confirm the above hypothesis. The activation energy associated with the chemical surface exchange reaction was calculated to be $0.47 \pm 0.25$ eV. If the $k_{chem}$ value obtained at lowest temperature (394 °C) is considered as an outlier, as it appears to be, the activation energy resulting from fitting with remaining data points becomes $0.89 \pm 0.23$ eV.
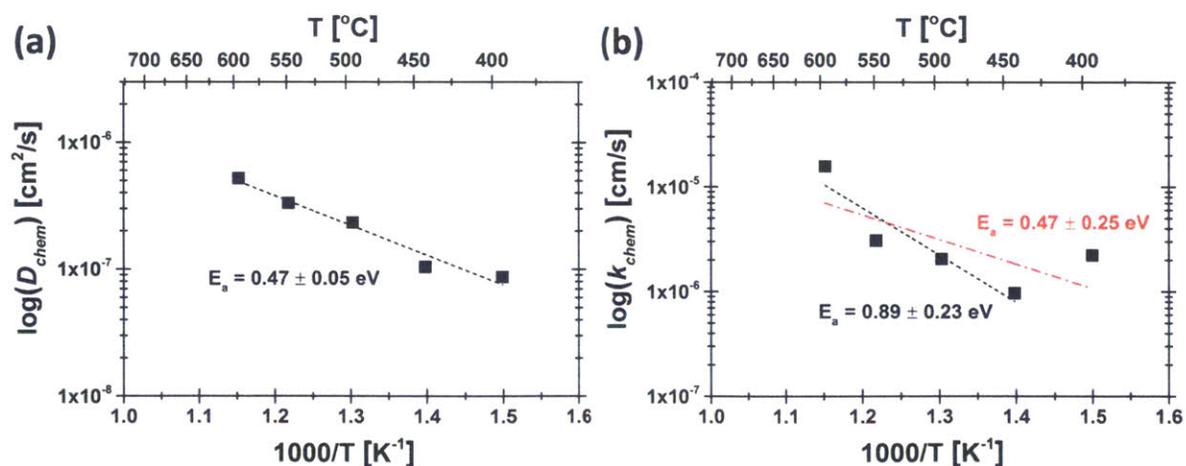


**Figure 51. Arrhenius plots of (a) $D_{chem}$ and (b) $k_{chem}$ obtained from color front motion experiments in 10PCO thin film during oxidation step (1000 ppm $H_2$/Ar to $O_2$).**

# CHAPTER 4. DISCUSSION

## 4.1 Optical characteristics of PCO thin films

The broad absorption at 2.0 ~ 3.3 eV in the visible spectrum of PCO thin films results in a red/orange coloration as shown at Figure 15 and Figure 16. This absorption characteristic of the PCO system can be explained by considering Pr impurity band formation within the ceria optical band gap (~ 3.5 eV [84]) and resultant optical transition [85]. As illustrated in the energy band diagram at the Figure 52 (a), in addition to the valence to conduction band transition at UV wavelengths, optically induced transitions from the ceria valence band with O-2p character to the Pr level with Pr-4f character and from the Pr level to the ceria conduction band, in principle, become possible. The position of the Pr impurity level was derived earlier (from TGA and conductivity measurements) to lie 1.43 ± 0.03 eV below the bottom of the conduction band of ceria [42,65,86], while the thermal band gap of undoped ceria was reported to be 2.1 ~ 3.2 eV [66,87,88]. This places the Pr impurity level 0.67 ~1.77 eV above the upper edge of the valence band. The smaller average energy for the thermal excitation compared to the optical transition is consistent with expectations from the Franck-Condon principle that the vertical optical excitation be greater than the thermal excitation characteristic of the relaxed state [44].

The probability of optical transitions tied to the Pr impurity band can be expected to be $pO_2$ dependent. At sufficiently low $pO_2$, $Pr^{4+}$ is largely reduced to $Pr^{3+}$, thereby localizing electrons in the $Pr^{3+}$ acceptor levels. Under these conditions, the impurity levels are fully occupied, with the transition from valence band to Pr level suppressed (see at the Figure 52 (b)) and leading to the observed absorption change from red to transparent (as shown by Figure 16) [85]. The transition from the Pr band to the ceria conduction band, which should lie in the infra-red, is likely very weak, being an f-f transition and therefore optically forbidden [44].
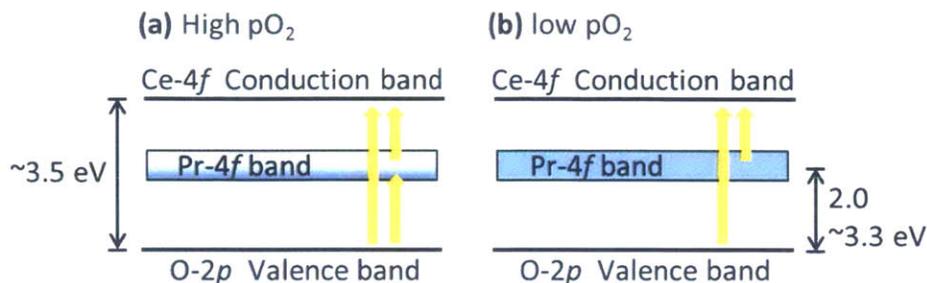
**Figure 52. Energy band diagrams of a 10PCO thin film when the sample is oxidized (a) and is reduced (b). Reprinted from a reference [75].**

In Figure 15, since these films underwent oxidation during the post-PLD anneal step, all PCO films have a large fraction of $Pr^{4+}$, consistent with Equation (10) and therefore a strong absorption of light due to excitation of electrons from the ceria valence band into the empty $Pr^{4+}$ levels. The valence band to Pr band adsorption in 1PCO thin films is difficult to deconvolute from its wavelength dependent transmission spectra due its lower absorptivity and the superposition of oscillating thickness fringes. The strongest absorption is obtained for the 20PCO films given the larger concentration of Pr. Undoped ceria remain transparent under similar conditions, consistent with a lack of optically active impurities. As shown in Figure 16, light absorption in the visible spectrum changes dramatically in 10PCO and 20 PCO films when shifting from oxidized (red) to reduced (transparent) conditions. By cooling the films quickly enough, the degrees of oxygen nonstoichiometry and thereby the absorptivity induced at elevated temperatures can be frozen-in to room temperature. Along with the well understood defect equilibria, these results confirm that optical absorption in PCO arises from carrier excitation from the valence band into empty Pr levels ($Pr^{4+}$) which become blocked once those levels are occupied following reduction.

## 4.2 Investigation of defect chemical properties of PCO thin film

### 4.2.1 Determination of absorption coefficients ($\alpha_{Pr^{4+}}$) associated with the $Pr^{4+}$ color center

The transmission of light by an optical medium with absorption coefficient $\alpha$ is described by

$$I_T = I_0 \exp(-\alpha w) \tag{34}$$

where $I_T$ and $I_0$ are transmitted and incident light intensity, respectively and $w$ is the path length of the propagating light beam (i.e. film thickness) [44].

Assuming no change in reflectivity within the $pO_2$ and temperature range of interest, the transmitted light intensity exiting the sample, $I_2$, can be expressed as

$$I_2 = I_0 \exp(-\alpha_{system} w_{system}) \exp(-\alpha_{Pr^{4+}} w_{PCO}) \tag{35}$$

where $\alpha$ is the absorption coefficient and $w$ is the thickness for the corresponding material. In Equation (35), $\alpha_{system}$ and $w_{system}$ account for the absorption (or reflection) of all sources such as the quartz tube and substrate other than $Pr^{4+}$ centers. Based on the defect equilibrium model of the PCO system [65], nearly all of the Pr ions are reduced to $Pr^{3+}$ at highly reducing conditions ($pO_2 \leq 10^{-16}$), in agreement with the low saturated absorption values at low $pO_2$ values. For example, as shown Figure 17, the oxygen partial pressure was changed from $\sim 10^{-23}$ atm to $\sim 10^{-21}$ atm, but the transmission of PCO film didn't change. Thus, the absorption by $Pr^{4+}$ ions becomes negligible in that regime, leading to

$$I_1 = I_0 \exp(-\alpha_{system} w_{system}) \tag{36}$$

where $I_1$ is the transmitted light intensity when $\alpha_{Pr^{4+}} \approx 0$. This allows one to obtain a value for $I_1$. By substituting Equation (36) into Equation (35), $\alpha_{Pr^{4+}}$ is extracted as follows.

$$I_2 = I_1 \exp(-\alpha_{Pr^{4+}} w_{PCO}) \tag{37}$$

The $Pr^{4+}$ ion absorption coefficients obtained in this manner are shown in Figure 53 as a function of $pO_2$. For Sample I as shown in Figure 53 (a), the sample was reduced and then oxidized in a stepwise manner at 600 °C, with the obtained absorption coefficients showing corresponding reversible changes in magnitude. Samples II were reduced from high $pO_2$ at different temperatures (Figure 53 (b)). As PCO

reduces with increasing temperature and decreasing $pO_2$, correspondingly, the absorption coefficient decrease from 550 °C to 700 °C and from ~1 atm to ~$10^{-4}$ atm $O_2$, respectively.

The absolute values of the absorption coefficient obtained from Samples I and II at the same temperature (600 °C), shown in Figure 54, were found not to be identical, they appear to follow the same $pO_2$ dependence. More specifically, the magnitude of the absorption coefficient of Sample II was about 40 % larger than that of Sample I. The origin of the different values for the absorption coefficients is discussed later (Section 4.2.4).
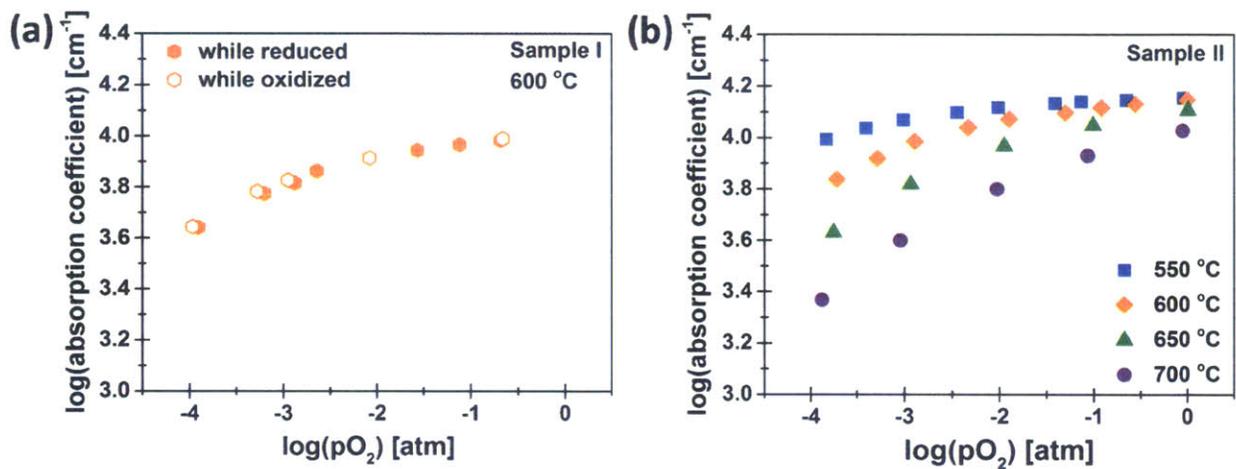


**Figure 53. Plot of the $pO_2$-dependent absorption coefficient for 10PCO for Sample I at 600 °C (a) and for Sample II at 550 °C, 600 °C, 650 °C and 700 °C (b).**
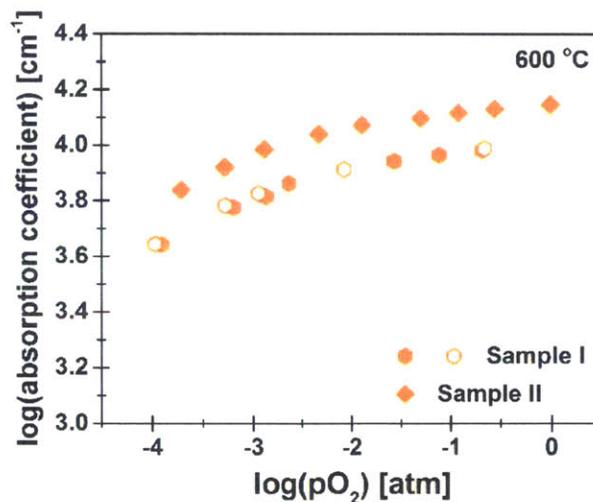


**Figure 54. Plot of the $pO_2$-dependent absorption coefficient for 10PCO for Sample I and Sample II at 600 °C.**

*4.2.2 Determination of extinction coefficient ($\varepsilon_{Pr^{4+}}$) of the $Pr^{4+}$ color center*

Simultaneous measurement of optical absorption and chemical capacitance allows one to derive information about the oxygen nonstoichiometry $\delta$ from both the chemical capacitance and the optical absorption. Since the optical absorptivity depends on the concentration of $Pr^{4+}$, it can be tied to the value of $\delta$ via Equation (28). On the other hand, $\delta$ can be determined from the chemical capacitance by using Equation (15) and (16) given that the absolute $\delta$ value can be derived by Equation (19) and (20). In this work, the absorption coefficient related to the $Pr^{4+}$ ions ($\alpha_{Pr^{4+}}$), obtained from *in situ* optical measurements, was correlated with the concentration of $Pr^{4+}$ ions ($[Pr^{4+}]$) derived from chemical capacitance obtained at the same $pO_2$ values. Following the Beer-Lambert law [44], it follows.

$$\alpha_{Pr^{4+}} = \varepsilon_{Pr^{4+}}[Pr^{4+}] \tag{38}$$

where $\varepsilon_{Pr^{4+}}$ is the molar extinction coefficient of $Pr^{4+}$ ions.
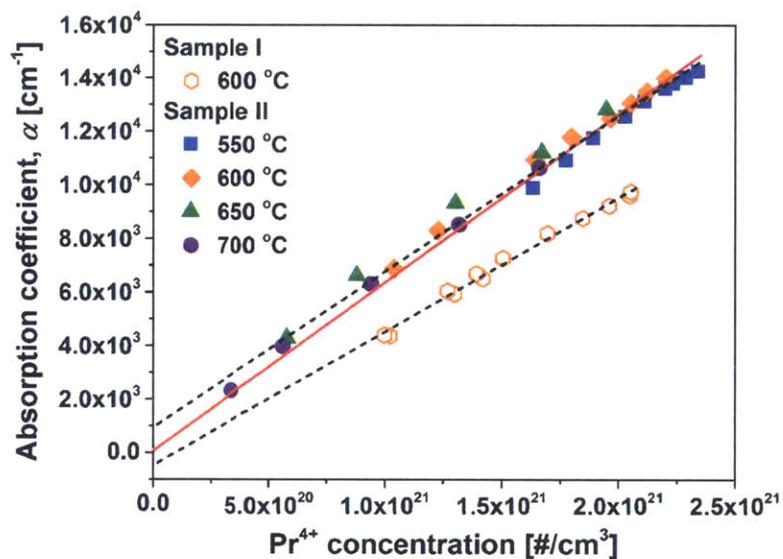


**Figure 55. Plot of experimentally obtained absorption coefficient of 10PCO as a function of $Pr^{4+}$ concentration obtained experimentally from $C_{chem}$ measurement for Sample I at 600 °C and for Sample II at 550 °C, 600 °C, 650 °C and 700 °C. Red solid and black dashed lines represent a linear fit with and without an imposed zero y-axis intercept, respectively.**

The data in Figure 55 show the expected linear relationship between $\alpha_{Pr^{4+}}$ and $[Pr^{4+}]$ for both

Samples I and II. For Sample I, the value of $\varepsilon_{Pr^{4+}}$, derived from the slope of $\alpha_{Pr^{4+}}$ vs $[Pr^{4+}]$ obtained at

600 °C, is $5.01 \pm 0.14 \times 10^{-18}$ cm$^2$, while the intercept to the y-axis shows a small negative offset of

$-474.5 \pm 223.5$ cm$^{-1}$, not far from the expected zero value. For Sample II, measured at four temperatures,

the value of $\varepsilon_{Pr^{4+}}$ and the y-axis intercept are $5.86 \pm 0.12 \times 10^{-18}$ cm$^2$ and $927.5 \pm 207.3$ cm$^{-1}$, respectively,

whose values are close in magnitude to those obtained for Sample I. If the data for Sample II are fitted

under the assumption that the y-axis intercept is zero, the value of $\varepsilon_{Pr^{4+}}$ obtained from the slope is then

$6.37 \pm 0.05 \times 10^{-18}$ cm$^2$. The linear fit under these circumstances is shown as a red solid line in Figure 55.

The discrepancy in $\varepsilon_{Pr^{4+}}$ values between Sample I and II, even though they were obtained for the same

10PCO film composition, results from differences in the measured absorption coefficients, as discussed

later (Section 4.2.4). It is noteworthy that the magnitude of $\varepsilon_{Pr^{4+}}$ is close to the extinction coefficient for

Ce$^{4+}$ ($5.90 \pm 0.02 \times 10^{-18}$ cm$^2$) which we calculated from the reported absorption coefficient at the direct

band gap energy of ceria thin films [89], indicating a similar character of transition from $O_{2p}$ to either $Pr_{4f}$

or $Ce_{4f}$.

Once a reliable value for the extinction coefficient is derived, the value of $\varepsilon_{Pr^{4+}}$ can open up future

opportunities for determining defect concentrations and nonstoichiometry in thin films such as PCO as

functions of temperature and pO$_2$ from optical studies alone. This could be especially important at reduced

temperatures where meaningful $C_{Chem}$ measurements may not be possible. In order to determine which

$\varepsilon_{Pr^{4+}}$ should be used among the values derived by linear fitting with and without a y-axis intercept, the

expected absorption coefficients are calculated by using Equation (38) with Pr$^{4+}$ ion concentration from

the thin film defect model [68] and $\varepsilon_{Pr^{4+}}$ values for each case. As shown in Figure 56, for both cases, the

expected absorption coefficients of Pr$^{4+}$ are well matched with the experimentally obtained ones in the

high pO$_2$ regime, which is reasonable because the two $\varepsilon_{Pr^{4+}}$ values are close to each other. However, in

the low pO$_2$ regime, the use of the $\varepsilon_{Pr^{4+}}$ value ($5.86 \pm 0.12 \times 10^{-18}$ cm$^2$) together with the y-axis intercept

($927.5 \pm 207.3$ cm$^{-1}$) gives an over-estimation of the expected absorption coefficients, while the use of

$\varepsilon_{Pr^{4+}}$ value ($6.37 \pm 0.05 \times 10^{-18}$ cm$^2$) without a y-axis intercept shows reasonably good agreement. This comes from the fact that absorption coefficient values at low pO$_2$ are close to the y-axis intercept value. Therefore, $\varepsilon_{Pr^{4+}}$ values derived without a y-axis intercept should be used when other PCO films are investigated only by optical measurements. It is noteworthy that good agreement between experimentally obtained absorption coefficients and estimated ones with Pr$^{4+}$ concentration from the thin film defect model validates our finding that thin films exhibit a somewhat different defect equilibria than their bulk counterparts.

**(a)**

**(b)**
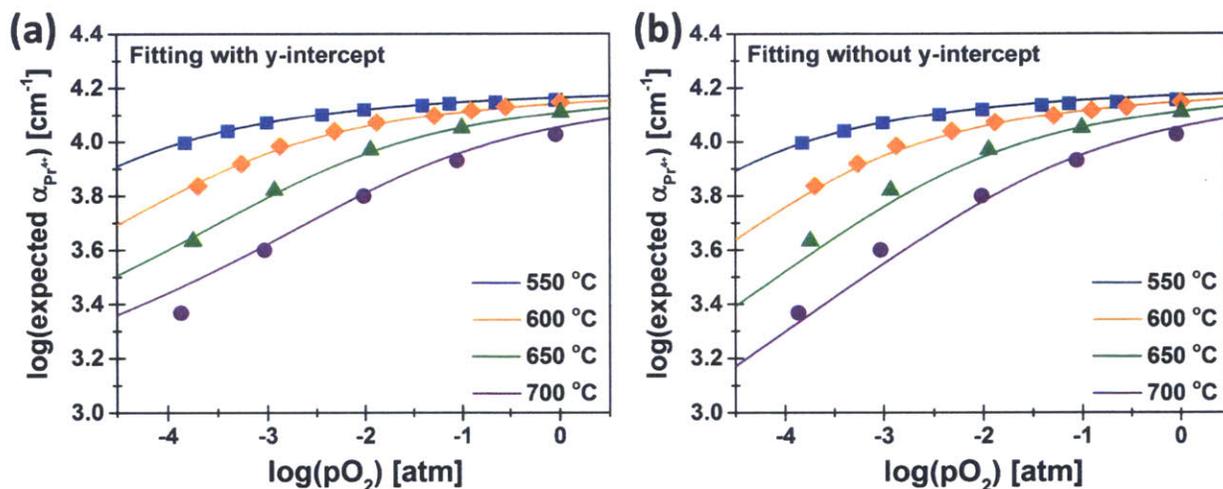
**Figure 56. Plot of the expected absorption coefficient values calculated by using Equation (38) with Pr$^{4+}$ concentration obtained from thin film defect model [68] and the molar extinction coefficient values of Pr$^{4+}$ ions derived from the linear fitting (a) with and (b) without y-intercept for Sample II in Figure 55. The experimentally obtained absorption coefficients of Pr$^{4+}$ for Sample II at 550 °C, 600 °C, 650 °C and 700 °C are presented as dots.**

### 4.2.3 Nonstoichiometry in PCO thin films

Changes in Pr$^{4+}$ concentration can be calculated from the measured absorption coefficient directly by using a reference state, as in the following relationship.

$$[Pr^{4+}]_2 = \frac{\alpha_{PCO,2}}{\alpha_{PCO,1}} [Pr^{4+}]_1 \qquad (39)$$

In equation (39) it is assumed that the extinction coefficient does not change with pO$_2$ at a given temperature, as indicated by Figure 55. Experimentally obtained $\alpha_{Pr^{4+}}$ values from the optical absorption

measurement for Sample I were converted to $Pr^{4+}$ concentrations using a reference value of $[Pr^{4+}]$ chosen at the highest $pO_2$ from either the thin film defect model derived from EIS measurements [68] or the bulk defect model derived from TGA measurements on bulk 10PCO [65]. As shown in Figure 57, the resulting $[Pr^{4+}]$ values exhibit trends more consistent with the thin film model. This result confirms that thin films exhibit different defect formation energies as compared to the bulk, in agreement with Chen et al.'s study [68], and can conceivably be obtained without performing simultaneous optical and chemical capacitance measurements, opening the door to complete determination of defect chemistry only by optical methods.
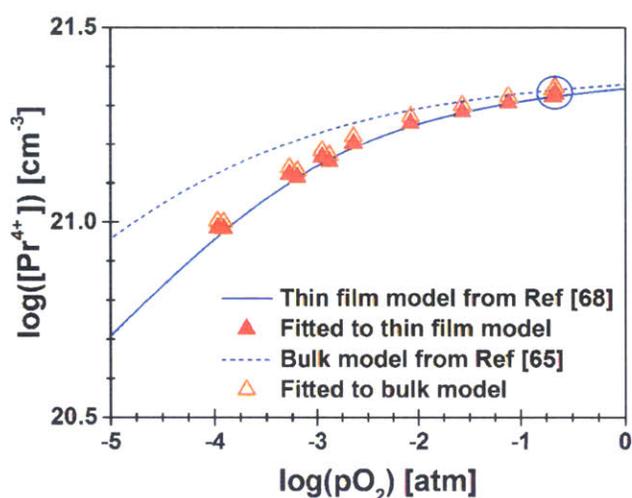


**Figure 57.** $Pr^{4+}$ concentration derived from $\alpha_{Pr^{4+}}$ by use of Equation (39) with the reference $Pr^{4+}$ concentration (indicated by blue open circle) equated to either the thin film model from EIS measurement [68] or bulk model from TGA measurement [65].

While chemical capacitance has proven to be a useful tool in quantifying the defect concentrations in thin films of ceria based materials [68,90], conflicting results have been observed in other systems, such as $(La,Sr)CoO_3$ (LSC). For example, some authors conclude, based on chemical capacitance measurements performed on LSC films, that nonstoichiometry is greater in films than in bulk specimens, while in other studies, the reverse is reported [73,91]. In this study, the optical absorption measurements were able to confirm that trends in defect-induced absorption were indeed in excellent agreement with chemical capacitance measurements performed on this ceria-based model system.

## 4.2.4 Other factors needed to be considered

_Effect of interference fringe on determination of absorption coefficients_

Transmission through a sample comprised of the active thin film and transparent substrate is characterized by an oscillating spectrum, called the interference fringe, which is created by reflection at the interfaces. By analyzing the maximal and minimal transmittance values in the fringes and the wavelength spacing between them with the envelope method, both the refractive index $n(\lambda)$ and thin film thickness can be determined [78]. The transmission, $T$, for the sample with interference fringe can be expressed by the following equations [78].

$$T = \frac{Ax}{B - Cx + Dx^2} \tag{40}$$

$$A = 16s(n^2 + k^2) \tag{40a}$$

$$B = [(n + 1)^2 + k^2][(n + 1)(n + s^2) + k^2] \tag{40b}$$

$$C = [(n^2 - 1 + k^2)(n^2 - s^2 + k^2) - 2k^2(s^2 + 1)] \cdot 2cos\emptyset$$
$$-k[2(n^2 - s^2 + k^2) + (s^2 + 1)(n^2 - 1 + k^2)] \cdot 2sin\emptyset \tag{40c}$$

$$D = [(n - 1)^2 + k^2][(n - 1)(n - s^2) + k^2] \tag{40d}$$

$$x = \exp(-\alpha d) \tag{40e}$$

$$\alpha = \frac{4\pi k}{\lambda} \tag{40f}$$

$$\emptyset = \frac{4\pi n d}{\lambda} \tag{40g}$$

where $n$ and $k$ are the refractive index and the extinction coefficient, respectively, in the complex refractive index of the thin film, $s$ is the refractive index of the transparent substrate ($k$ for the substrate assumed to be zero in the visible range) and $d$ is the thin film thickness. In Equation (40f), $\alpha$ is the absorption coefficient.

The interference fringe was observed in the transmittance spectra for the undoped ceria and PCO thin films on transparent substrates, as shown in Figure 15. The higher frequency of oscillation in a given

wavelength range for the thicker 10PCO confirms this feature to be the interference fringe (Figure 58). In order to avoid the contribution from the absorption of $Pr^{4+}$ ions, 10PCO samples with different thicknesses were reduced under 0.1% $CO/CO_2$ atmosphere at 600 °C ($pO_2 \approx 10^{-19}$ atm) for 8-10 hours and rapidly quenched to room temperature.

Figure 59 (a) shows the modeled transmittance spectra of an undoped ceria thin film on sapphire substrate with different thickness by using Equation (40). Because there is no reported refractive index values of Pr doped ceria, $n(\lambda)$ of undoped ceria dense thin films, reported by Oh et al [92], was used, while $s(\lambda)$ of the sapphire substrate was extracted by measuring transmittance. Only the 400 to 700 nm wavelength range was modeled because the analytical expression for the transmittance spectra is more applicable in the transparent regime. As shown Figure 59 (a), thicker film gives more frequent oscillations, consistent with the experimentally measured spectra (Figure 58). The modeled spectra of undoped ceria with 420 nm thickness is compared with one measured from 10PCO thin film with the same thickness in Figure 59 (b). The frequency and the maximum position of the interference fringe show good agreement. The difference in the actual transmittance value can be originated from the difference in materials' refractive index, any inhomogeneity in film density/porosity, thickness and surface roughness.
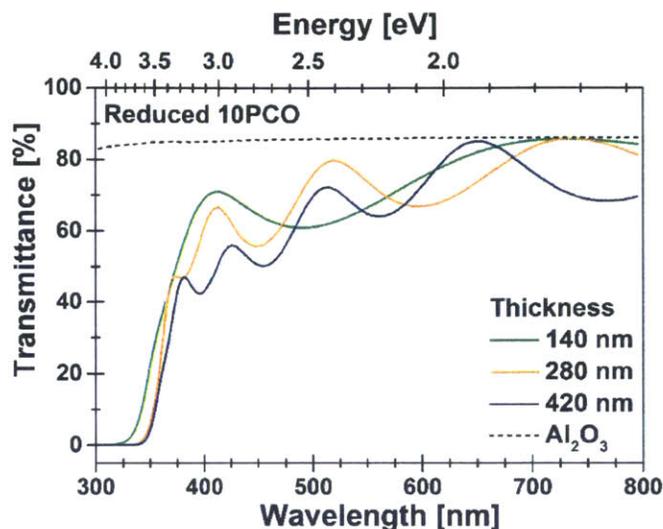
**Figure 58. Transmittance spectra of reduced 10PCO thin films with different thickness on sapphire substrate. The films were reduced in a 0.1% $CO/CO_2$ atmosphere at 600 °C ($pO_2 \approx 10^{-19}$ atm) for 8-10 hours, followed by rapid quenching to room temperature.**
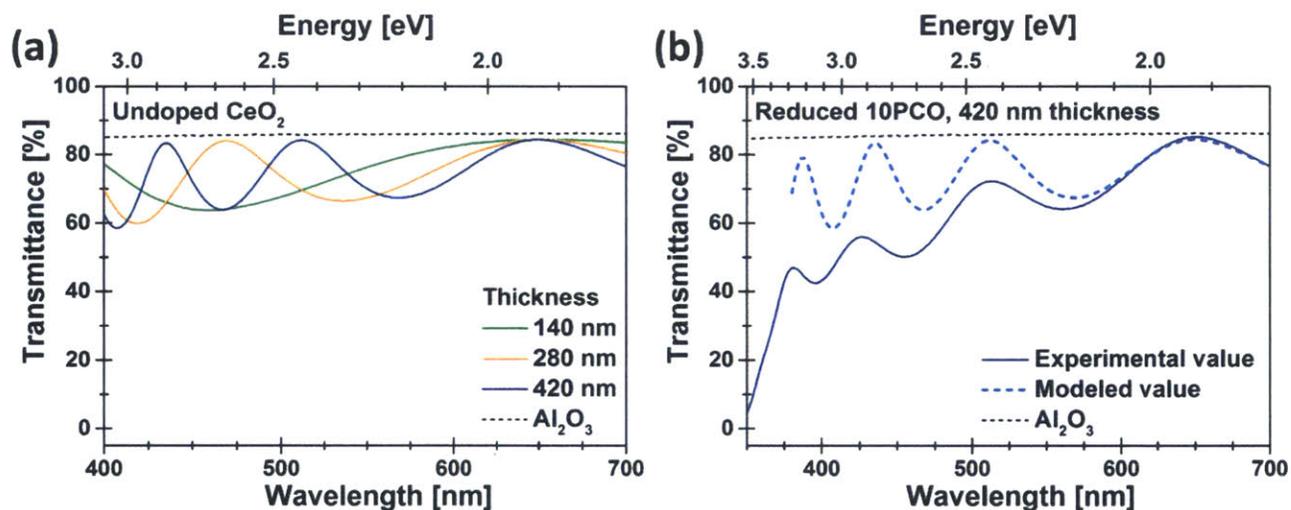


**Figure 59. (a) Modeled transmittance spectra of undoped ceria thin films with different thickness on sapphire substrate. (b) Comparison of experimentally obtained transmittance spectra of 10PCO thin film with modeled one for undoped ceria thin film with the same thickness, 420 nm.**

Figure 60 (a) shows transmittance spectra of Sample II recorded at different $pO_2$ and at the same temperature, 650 °C, during joint *in situ* optical and EIS measurements. Each spectrum was recorded after the transmittance reached a new equilibrium state following a $pO_2$ change. Spectra in the 420 nm – 560 nm range of wavelengths was selected considering the transparent window of the bandpass filter (FGB37, 335-610 nm). In the wavelengths of interest, the film is more absorbing (more $[Pr^{4+}]$) when oxidized. At

a highly reduced condition (pO$_2$ = ~10$^{-21}$ atm), interference fringes are clearly observed. However, the amplitude of oscillation decreases as pO$_2$ increases and thus absorption by Pr$^{4+}$ ions increases. Because Pr$^{4+}$ ions induce absorption in a broad range of wavelengths, any wavelength in this regime can, in principle, be used to extract the absorption coefficient of Pr$^{4+}$ ions. However, as shown in Figure 60 (b), the absorption coefficient depends on wavelength. For example, the absorption coefficient calculated at 450 nm, where the oscillation reaches a maximum, is higher in magnitude (~28%) than ones at 532 nm, even though the pO$_2$ dependency of the absorption coefficient at the different wavelengths is identical. This wavelength dependence of the absorption coefficients results in different values of extinction coefficient as calculated from Equation (38).
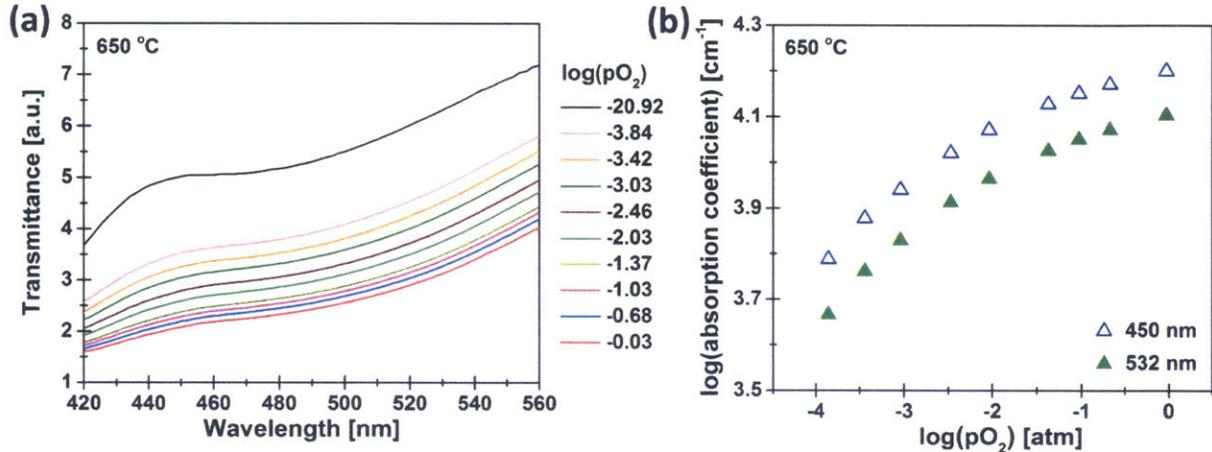


**Figure 60. (a) pO$_2$ dependent transmittance spectra of Sample II at 650 °C during joint *in situ* optical and EIS measurement (b) Comparison of absorption coefficients calculated at different wavelength.**

The difference in values of absorption coefficients and corresponding extinction coefficients for Sample I and Sample II at the same temperature (Figure 54 and Figure 55, respectively) can be explained by this wavelength dependence, originated from the oscillating spectra based on interference fringe. Even though the same wavelength, 532 nm, was used for Sample I and II during *in situ* optical measurements, the spectral shape of two samples can be different due to, for example, difference in thickness. Indeed, the transmittance spectra of Samples I and II, reduced and quenched, show different oscillations as shown in Figure 61 (a). The measured thickness difference between two samples ranges from 4 nm to 20 nm,

98

considering the standard deviation of measured values. As shown in Figure 61 (b), even 5 nm difference in thickness results in a considerable shift of the transmittance spectra.

Therefore, careful attention is required when applying the absorption and extinction coefficients obtained from one sample in the analysis of another sample. The interference-free spectra, which can be calculated from the interference fringe given that optical parameters such as $n(\lambda)$ and optical band gap energy at temperature and $pO_2$ of interest are fully known [78], may be used for direct comparison between samples.
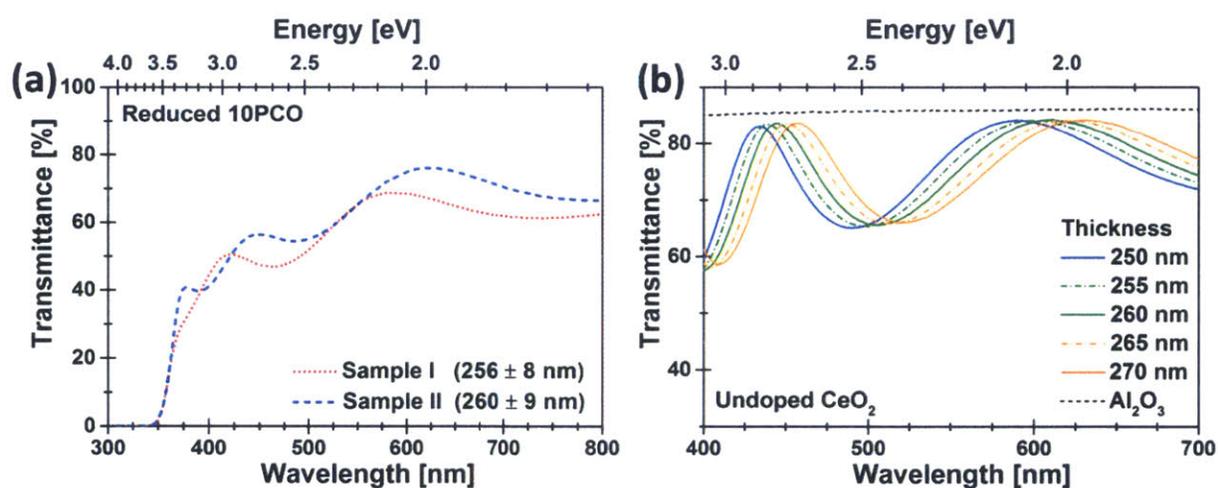


**Figure 61.** (a) Transmittance spectra of Sample I and II used for joint *in situ* optical and EIS measurement. The films were reduced at 1000 ppm $H_2$/Ar atmosphere at 600 °C ($pO_2 \approx 10^{-23}$ atm) for 8 hours, followed by rapid quenching to room temperature. (b) Modeled transmittance spectra of undoped ceria thin films grown on sapphire substrates with different thickness.

*Sample cracking due to chemical expansion*

The PCO system exhibits oxygen non-stoichiometry induced chemical expansion ($\varepsilon_C$) at elevated temperatures and reducing environments. An understanding of this phenomenon is needed in order to be in a position to enhance the mechanical integrity of SOFCs [93,94]. The chemical expansion of PCO system results from the superposition of two contributions, namely lattice expansion due to the increase in radius of Pr cations upon reduction ($Pr^{4+}$ to $Pr^{3+}$) and lattice contraction due to relaxation around oxygen vacancies [95]. Similar to the thermal coefficient of expansion, the chemical coefficient of expansion ($\alpha_C$) is defined as follows.

$$\varepsilon_C = \frac{\Delta l_c}{l_0} = \alpha_C(\delta - \delta_{ref}) \tag{41}$$

where $\Delta l_c$ and $l_0$ are isothermal change in the sample length upon $pO_2$ change and the sample length at a reference condition, respectively, and $\delta$ and $\delta_{ref}$ is the non-stoichiometry of interest and at a reference condition, respectively. For 10PCO, the value of $\alpha_C$ was reported by Bishop et al. as 0.087 ± 0.005, for the conditions of 650 ~ 900 °C and $10^{-16}$ ~ 1 atm $pO_2$ [94]. In the case of a thin film supported by a significantly thicker substrate, assuming that the film is clamped to the substrate, the film is under in-plane stress and expands out-of-plane upon a decrease in $pO_2$. The isothermal in-plane stress change ($\Delta\sigma$) and corresponding out-of-plane strain ($\varepsilon_{C,z}$) can be calculated using the following equations [96].

$$\Delta\sigma = -\Delta\varepsilon_C \frac{E}{1-v} \tag{42}$$

$$\varepsilon_{C,z} \cong \Delta\varepsilon_C \left(\frac{1+v}{1-v}\right) - \frac{2v\sigma_0}{E} \tag{43}$$

where $\Delta\varepsilon_C$ is the change in strain, $E$ is Young's modulus, $v$ is Poisson's ratio (usually 0.33) and $\sigma_0$ is the stress in the film in the reference state. From *in situ* wafer curvature measurements on 10PCO thin films deposited on sapphire substrates, it was found that the change in in-plane stress from a reference condition reached to ~380 MPa upon reduction under $10^{-5}$ atm $pO_2$ at 750 °C [96]. This in-plane stress induced by chemical expansion can cause cracking in the films during deposition, as shown in Figure 62.

This chemical expansion induced in-plane stress can also impact the optical transmittance measurements performed on PCO films. As discussed above, 10PCO films were annealed at highly reducing condition ($pO_2 \leq 10^{-16}$) in order to reach the condition that far majority of the Pr ions exist as $Pr^{3+}$. This reduction step occasionally caused cracking of the sample. As shown in Figure 63, initially crack-free films were found to be severely cracked with sections of the film lost due to delamination following annealing at 800 °C and $10^{-21}$ atm $pO_2$. The value of transmittance measured in $pO_2$ = 0.21 atm, before and after this annealing step, increased by approximately 6.0 % (from 5.83 to 6.17 in arbitrary unit), indicating that either more light was transmitted through the cracks or the light absorbing material was decreased.

The increased transmitted light intensity due to cracks induced by chemical expansion can affect the determination of the optical absorption coefficients. Figure 64 (a) shows absorption coefficients obtained from a 10PCO thin film found to be cracked after completion of the experiment at 650 °C (Figure 64 (b)). The sample was reduced starting from high pO$_2$ and finally annealed at $10^{-21}$ atm pO$_2$ for joint *in situ* optical and EIS measurement. The absorption coefficients were obtained from the recorded transmitted light intensities by using the method discussed in the Section 4.2.1, and the expected values were calculated from Equation (38) by choosing the value of $\varepsilon_{Pr^{4+}}$ (6.45 × $10^{-18}$ cm$^2$), which makes the experimentally obtained value at the highest pO$_2$ to be matched with the expected value, and by using the Pr$^{4+}$ ion concentration from the thin film defect model [68]. As shown Figure 64 (a), the sample cracking introduces an over-estimation of the absorption coefficients, especially for ones in the lower pO$_2$ regime. Assuming that the sample is cracked at the lowest pO$_2$ ($10^{-21}$ atm pO$_2$ for this sample) so that the corresponding transmitted light intensity, $I_l$, in the Equation (37) is only affected by cracking, the absorption coefficients can be re-calculated as shown Figure 64 (a). By decreasing only $I_l$ by approximately 11%, the absorption coefficients decrease at all pO$_2$ regimes and become consistent with the expected values (5.29 × $10^{-18}$ cm$^2$ of $\varepsilon_{Pr^{4+}}$ is used). On the other hand, the experimentally obtained volume-specific $C_{chem}$ values for the cracked film agree well with non-cracked film from Sample II (Figure 65), which indicates, as expected, that the cracking does not affect the thermodynamic properties of the film.
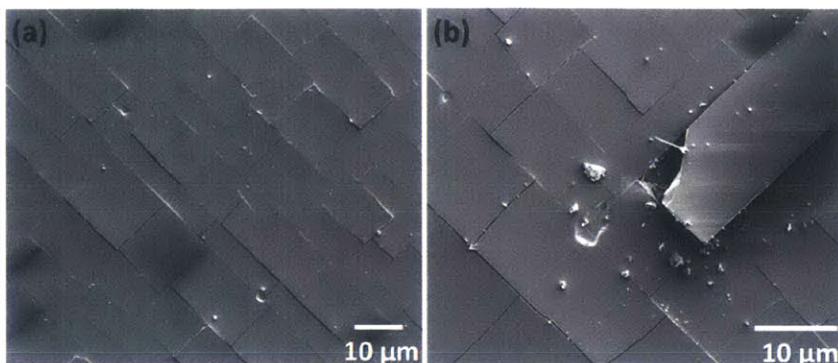
**Figure 62.** The SEM image of a cracked 10PCO film on YSZ substrate. The film was found to be cracked after deposition.
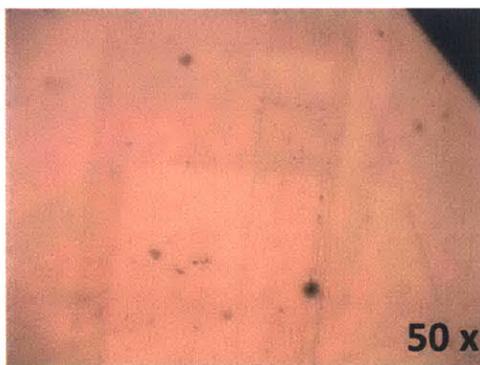


**Figure 63.** An optical microscope image showing micro-cracking in the film after being annealed at below $10^{-21}$ atm $pO_2$ and 800 °C. Cracks at this magnification are difficult to see by eye. See Figure 62 for higher magnification.
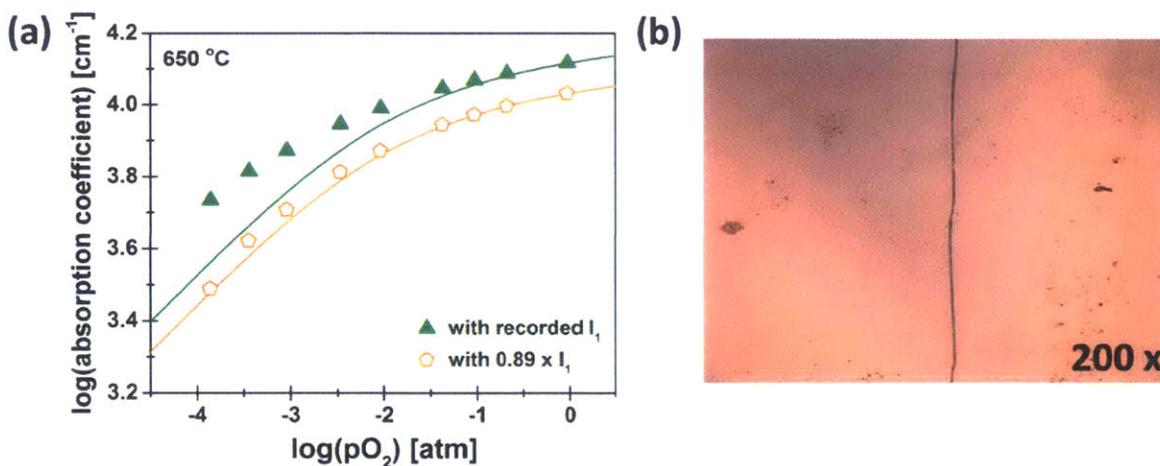


**Figure 64.** (a) Plot of the $pO_2$-dependent absorption coefficient for the $Pr^{4+}$ color center from the film with and without crack. The solid lines are the expected absorption coefficients calculated from Equation (38). The used extinction coefficients of $Pr^{4+}$ ions are indicated in the text. (b) The optical microscope image of a crack found in the film used for extracting absorption coefficients of the cracked film in (a). The sample went through a reduction step under $10^{-21}$ atm $pO_2$ at 650 °C.
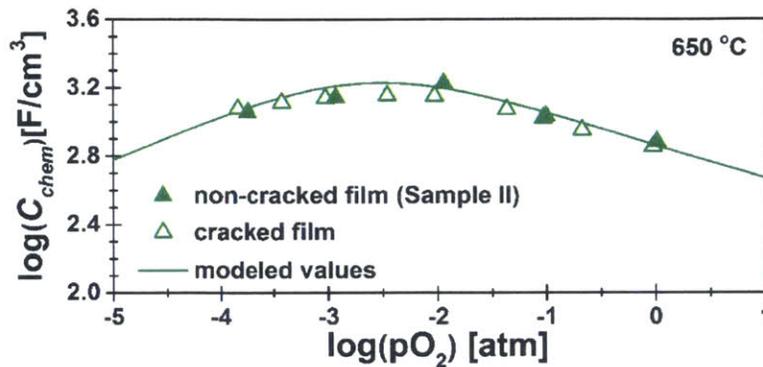
**Figure 65. Isothermal dependence of volume-specific $C_{chem}$ on pO$_2$ for non-cracked 10PCO thin film (Sample II) and cracked 10PCO thin film at 650 °C.**

## 4.3 Investigation of surface exchange kinetics of PCO thin film

### 4.3.1 Reaction mechanism of chemical oxygen surface exchange reaction

As discussed briefly in section 1.3, oxygen partial pressure changes act as the driving force for oxygen incorporation during optical transmittance relaxation measurements. Electrons, to be transferred to adsorbed oxygen species ($O_{x,ad}$), are supplied by the PCO electrode. Figure 66 (a) and (b) show macroscopic reaction pathways for the oxygen reduction and oxidation reactions, respectively. Both reactions consist of many elementary steps. For example, the oxygen reduction reaction includes oxygen adsorption, dissociation, electron charge transfer and ion incorporation into the oxide lattice. One (or several) of the elementary steps limits the overall reaction and is therefore called the rate determining step (RDS).



**(a)** $\frac{1}{2}O_{2,gas} + 2e' + V_O^{\cdot\cdot} \rightarrow O_O^\times$     **(b)** $O_O^\times \rightarrow \frac{1}{2}O_{2,gas} + 2e' + V_O^{\cdot\cdot}$
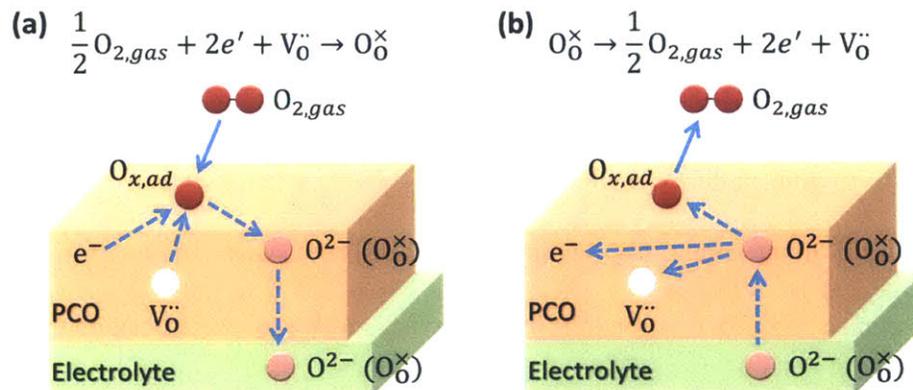
**Figure 66. Macroscopic reaction pathways for (a) chemical oxygen reduction reaction (PCO is oxidized) and (b) chemical oxygen oxidation reaction (PCO is reduced).**

In order to further clarify the reaction kinetics, the microscopic reaction pathways can be considered. Figure 67 illustrates two plausible pathways for the oxygen reduction reaction with (a) neutral $O_{ad}$ atoms and (b) superoxide and peroxide ad-ions [97]. The forward reaction for the case of (a) can be constructed as follows:

$$O_{2,gas} \rightarrow O_{2,ad} \qquad\qquad \text{adsorption} \qquad\qquad (44a)$$

$$O_{2,ad} \rightarrow 2O_{ad} \qquad\qquad \text{dissociation} \qquad\qquad (44b)$$

$$e^-_{bulk} \rightarrow e^-_{surface} \qquad\qquad \text{electronic conduction} \qquad (44c)$$

$$O_{ad} + e^-_{surface} \rightarrow O^-_{ad} \qquad\qquad \text{charge transfer} \qquad\qquad (44d)$$

$$V^{..}_{bulk} \rightarrow V^{..}_{surface} \qquad\qquad \text{ionic conduction} \qquad\qquad (44e)$$

$$O^-_{ad} + V^{..}_{surface} \rightarrow O^-_{surface} \qquad\qquad \text{incorporation} \qquad\qquad (44f)$$

$$O^-_{surface} + e^-_{surface} \rightarrow O^{2-}_{surface} \qquad\qquad \text{charge transfer} \qquad\qquad (44g)$$

$$O^{2-}_{surface} \rightarrow O^{2-}_{bulk} \qquad\qquad \text{ionic conduction} \qquad\qquad (44h)$$
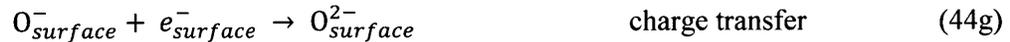
After an $O_2$ gas molecule adsorbs on the surface of the MIEC electrode, dissociation into $O_{ad}$ atoms occurs first, and then the charge transfer reaction with electrons transported from the electrode bulk follows. This charged adsorbed ion ($O^-_{ad}$) is incorporated into an oxygen vacancy site on the electrode surface. Full ionization of $O^-$ to $O^{2-}$ can occur while or right after being incorporated. It is noteworthy that dissociation of an adsorbed oxygen gas molecule into $O_{ad}$ atoms can be considered, even though it requires very high energy (> 5 eV), because it can be driven by entropic driving forces [98,99]. In a similar context, the reaction pathway, including the dissociative adsorption ($^1/_2 O_{2,gas} \rightarrow O_{ad}$), was also suggested [100]. In the case of (b), the formation of adsorbed superoxide ions ($O^-_{2,ad}$) and peroxide ions ($O^{2-}_{2,ad}$), accompanied with electron transfer reactions, is followed by dissociation into $O^-_{ad}$. Then, like the case of (a), ion transfer of $O^-_{ad}$ into the oxide lattice and final ionization occurs.
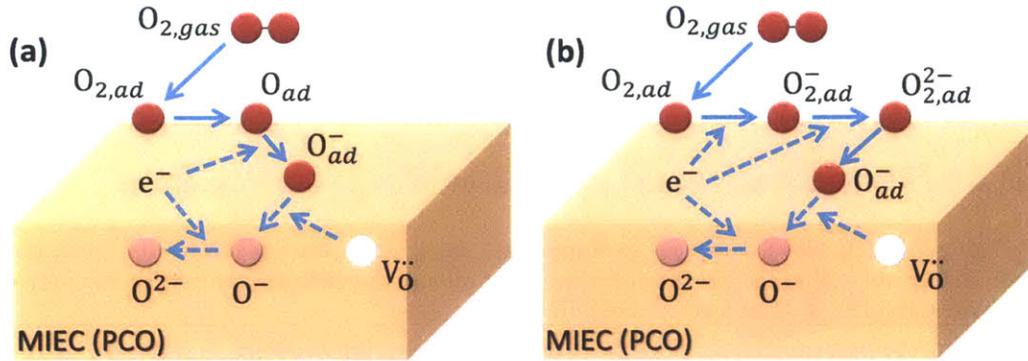
**Figure 67. Possible microscopic reaction pathways for chemical oxygen reduction reaction via (a) neutral atomic oxygen adsorbate ($O_{ad}$) and (b) superoxide and peroxide adsorbed ions.**

With an assumption that one reaction step among the reaction pathway is the RDS (in other words, other reaction steps are fast and in quasi-equilibrium), the dependence of the reaction rate constant on the activities of reactants and products in the overall reaction can be established by considering 1) the kinetic rate equations for concentration contributions in forward and backward reactions of the RDS and 2) the electron/ion transfer reaction across electrical/thermal energy barriers [30,97–103]. Chueh et al calculated the dependence of the oxygen exchange rate constant on the activities of species participating in the oxygen reduction reaction such as oxygen gas molecules, oxygen vacancy and electronic defects (electron and hole), classifying the situation with how many species are transferred before, during, or after the RDS and how many such reaction needs to occur in the net reaction [103]. The dependence of the oxygen exchange rate constant on the oxygen partial pressure for various situations is summarized in Table 7. The results indicate that MIEC electrodes with $m \geq \frac{1}{2}$ in a $p_{O_2}^m$ dependence of the exchange rate constant most likely involve at least one oxygen diatomic molecule (either uncharged or charged) in the RDS whereas those with $m \leq \frac{1}{4}$ most likely involve oxygen atomic species (either uncharged or charged) in the RDS. On the other hand, De Souza found the below empirical expression (Equation 45) for the isotope surface exchange coefficients ($k_{tracer}$) of acceptor-doped perovskite ($La_{0.6}Sr_{0.4}Co_{0.2}Fe_{0.8}O_{3-\delta}$, $SrTi_{0.9987}Fe_{0.0013}O_{3-\delta}$, $CaZr_{0.9}In_{0.1}O_{2.95}$, $La_{0.9}Sr_{0.1}Ga_{0.8}Mg_{0.2}O_{2.85}$) and fluorite oxides ($Ce_{0.8}Gd_{0.2}O_{1.9}$) [100].

$$m = \frac{\partial lnk_{tracer}}{\partial lnpO_2} = \frac{1}{4} - \frac{1}{2}\frac{\partial lnc_{V_O^{\cdot\cdot}}}{\partial lnpO_2} \tag{45}$$

From this universal finding, charge transfer reactions with atomic oxygen species (Equation 44d) was

proposed as the RDS, which is consistent with the result of Chueh et al's calculation.

**Table 7. The dependence of the oxygen exchange rate constant on the oxygen partial pressure for various situations. It does not include indirect oxygen partial pressure dependence via oxygen vacancy or electronic defect activities. Reprinted from a reference [103].**

| $O_{2,gas}$ adsorbed | Type of oxygen intermediate in the RDS | |
|---|---|---|
| | Atomic oxygen | At least one diatomic oxygen |
| Before RDS | $pO_2^{1/4}$ | $pO_2^{1/2}$ |
| During RDS | $pO_2^{1/2}$ | $pO_2^{1/2}$ |

In this study, $k_{chem}$ showed different pO$_2$ dependence between samples and also sometimes changed

during reduction-oxidation cycles in a given sample. This will be discussed later while considering the

correlation of reaction kinetics with surface chemistry change. Given that Sample III maintained a similar

pO$_2$ dependence of $k_{chem}$ and its $k_{chem}$ values did degraded little during 5 reduction-oxidation cycles (Figure

34), its value of $m = 0.44 \sim 0.61$ can be considered to best reflect the chemical oxygen surface exchange

reaction mechanism on PCO electrodes. First of all, the supply of electronic and ionic species (Equation

44c and 44e) is not likely to be the RDS, because electronic (by small polaron hopping) and ionic

conductivities of PCO show pO$_2^{-1/6}$ or weaker dependency on pO$_2$ under conditions of interest (1~10$^{-4}$ atm

pO$_2$ and 550~700 °C), as shown in Figure 68. And, as explained above, an $m$ value of ½ or above strongly

indicates that molecular oxygen species are involved in the RDS. Therefore, adsorption and dissociation

(Equation 44a and 44b) can be considered as the RDS in the case of Figure 67 (a). For the case of Figure

67 (b), adsorption of oxygen molecules, formation and dissociation of adsorbed superoxide ions ($O_{2,ad}^-$)

and peroxide ions ($O_{2,ad}^{2-}$) can be considered.

However, it may be somewhat dangerous to conclude the rate determining step simply by

examining the pO$_2$ dependence of $k_{chem}$ and applying it to the suggested models. Models, in the most of

the literature, were developed based on simple mass action rate expressions, which are only valid under a

dilute solution approximation. It is questionable that 10PCO (10 mol% Pr doped ceria) can safely be viewed as a dilute system. In addition, it was further assumed that the surface defect properties are the same as the bulk ones in terms of their concentration and pO$_2$ dependence. However, there are several experimental observations and computational predictions that the absolute concentration and pO$_2$ dependence of defects at the surface differ, often substantially, from those in the bulk [104–106]. In this study, Pr is found to preferentially segregate to the film surface (section 3.4.1). Higher surface Pr concentrations can be expected to lead to higher oxygen vacancy and electronic carrier concentrations at the surface. Additional exchange experiments, following surface chemical etching, could be used to test this hypothesis. However, temperatures would need to be sufficiently low to minimize further Pr segregation [107].
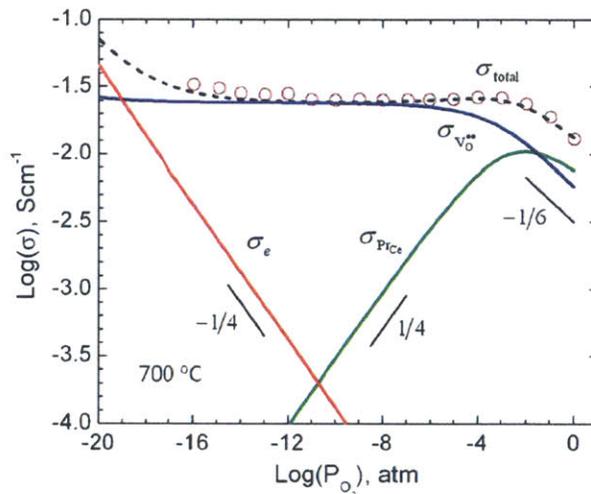


**Figure 68. Conductivity of 10PCO at 700 °C. Solid lines represent predicted contributions of oxygen vacancies ($\sigma_{V_O^{\bullet\bullet}}$), Pr small polarons ($\sigma_{Pr_{Ce}}$) and electrons in the ceria conduction band ($\sigma_e$) to the total conductivity (dashed line). Open circles are experimentally obtained data. Error is smaller than the data points. Reprinted from a reference [65].**

*4.3.2 Correlation between oxygen exchange kinetics and surface chemistry/morphology*

Figure 69 compares the values of $k_{chem}$ derived for Sample I, II and III upon reduction (a) and upon oxidation (b). Even though all 10PCO thin films were deposited under the same conditions within the same PLD chamber from the same PLD target (section 2.1.2 and 2.4.2), the electrochemical reaction activity of the samples show large variations. Specifically, $k_{chem}$ values of Sample III are larger than ones

obtained for Sample II; 1~2 orders of magnitude for the reduction step and 1.5~2.5 orders of magnitude for the oxidation step depending on $pO_2$. In addition, Sample III shows a stronger $pO_2$ dependence of $k_{chem}$ ($m = 0.50 \sim 0.55$) than Sample II ($m = \sim0.37$) at high $pO_2$ ($\geq 10^{-2.5}$ atm). Interestingly, in contrast to what was found for $k_{chem}$, values of $k_{elec}$ for Samples II and III are comparable and show similar $pO_2$ dependences to each other (although distinctly different from that for $k_{chem}$), as shown in Figure 70.
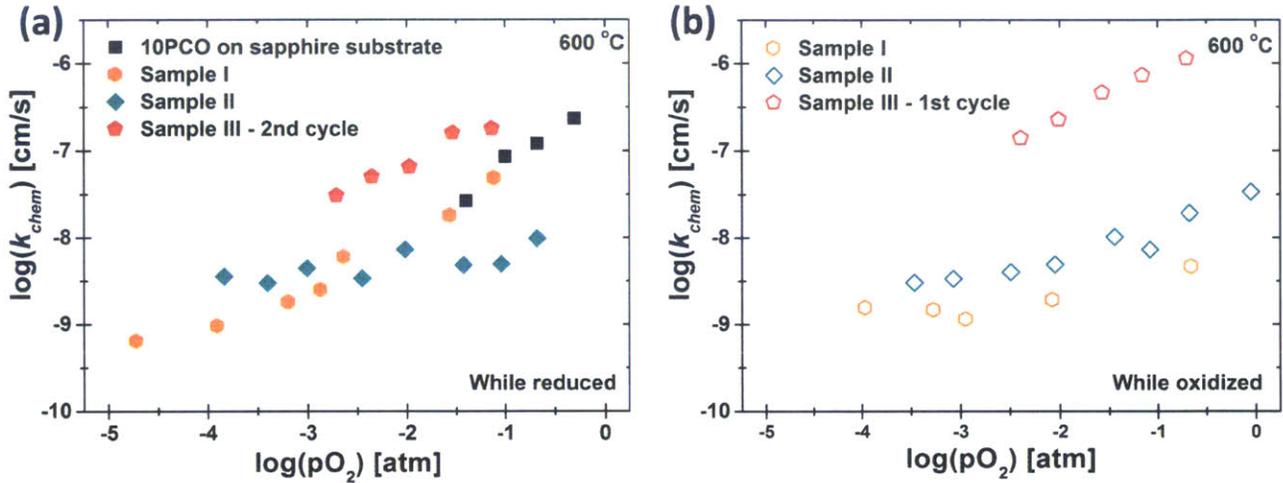


**Figure 69. Plot of $k_{chem}$ from optical relaxation versus $pO_2$ for Sample I, II and III at 600 °C obtained while reduced (a) and oxidized (b). $k_{chem}$ values are plotted using the final $pO_2$ value for each relaxation step. For Sample III, values from 2nd cycle are plotted for the reduction step, while the ones from 1st cycle are plotted for the oxidation step. The values for 10PCO on sapphire substrate are from reference [108].**
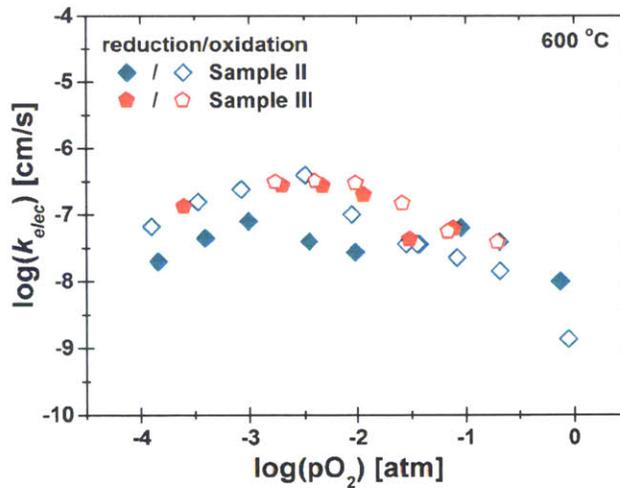


**Figure 70. Plot of $k_{elec}$ from EIS measurement versus $pO_2$ for Sample II and III at 600 °C obtained while reduced (closed symbols) and oxidized (open symbols). For Sample III, values from 1st cycle are plotted.**

This different reaction activity can be explained by changes in surface chemistry and morphology during measurements. During joint *in situ* optical and EIS measurement, as shown in Figure 9, one half of the sample remains open to monitor changes in transmittance, while the other half is covered with a porous Pt layer for electrochemical measurement. This contact metal-free surface may be more susceptible to outside contamination. Indeed, from XPS measurements (section 3.4.1), it was found that the surfaces of the PCO thin films, used in the optical relaxation measurements, were contaminated by impurities such as Bi, Na, Si and Ca. In addition, from secondary ion mass spectrometry (SIMS) measurement, significant concentrations of Si, K, Na and Ca were observed to accumulate on the 10PCO film surface following optical absorption measurements (Figure 71) [109]. This impurity contamination can be the primary source for degradation and the huge variation in the surface exchange reaction activity from one specimen to the next. The insensitivity of $k_{elec}$ to outside surface impurities can be rationalized if the reaction kinetics are governed by other process not sensitively related to PCO's surface characteristics, as discussed later (section 4.3.3).
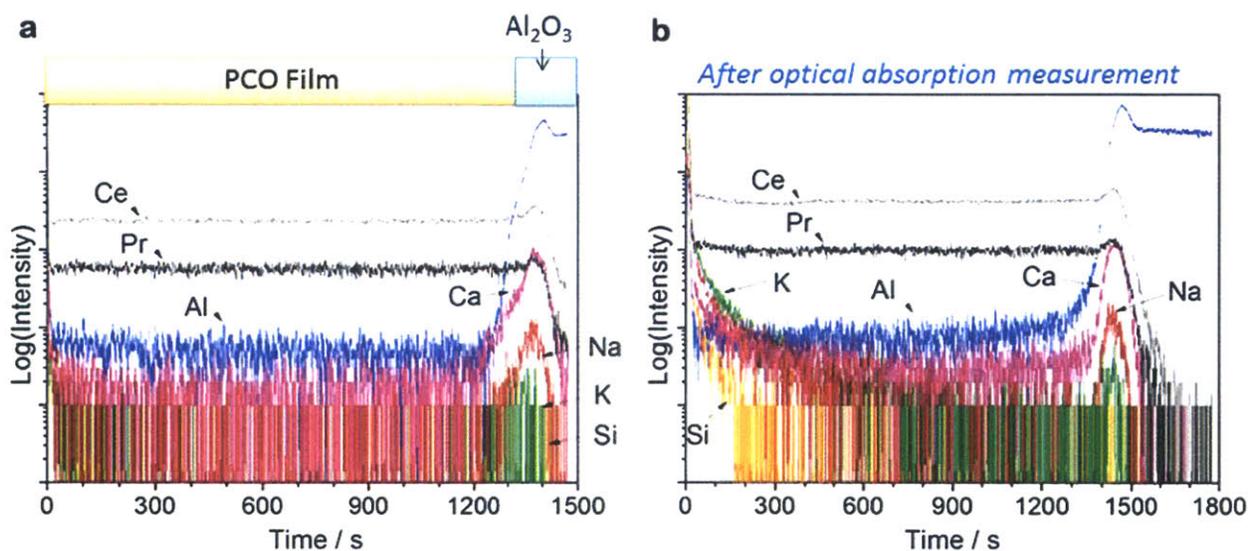


**Figure 71. SIMS depth profiles for an as-deposited (a) and post-optical measurement PCO thin film (b). The approximate positions of the film and sapphire substrate are indicated in 2a. Reprinted from a reference [109].**

As shown in Table 3, Sample III had only Bi as a contaminant on the surface. The origin of Bi was found to be the Pt paste used as a current collector for EIS measurement (section 3.4.1 to 3.4.3). Sample

I and II showed Bi contamination as well, though Bi on the Sample II surface was revealed by removing other major impurities by HCl etching (Table 5). In addition to that, the Bi peak was found at the XPS spectra for Pt paste (Figure 39 and Table 4), and the position dependent Bi composition profile across the sample confirmed that Bi diffused from the Pt paste source (Figure 40 (b)). The different surface morphology in the area near the Pt paste to a position far from the Pt paste is believed to be due to Bi diffusion and subsequent agglomeration (Figure 45). From $k_{chem}$ results of Sample III, one finds that a Bi rich surface layer and resultant Bi containing particles lead to a decrease in $k_{chem}$ by a factor of 5 (Figure 34). Furthermore, the $pO_2$ dependence of $k_{chem}$ did not show noticeable change, meaning that the reaction mechanism was maintained.

However, Sample I and II had Si, Na and Ca, in addition to Bi, as surface impurities, and these caused considerable degradation in the reaction kinetics, as noted above. Not only did they induce a significant decrease in $k_{chem}$ values, the reaction mechanism changed as well. Specifically, for Sample I, the strong $pO_2$ dependency of $k_{chem}$ ($m = 0.66 \pm 0.06$) during the reduction step became weaker ($m = 0.27 \pm 0.00$) following re-oxidation, accompanied with decrease in magnitude (Figure 21). This transition also appeared for Sample II at 550 °C; $m = 0.49 \pm 0.11$ for the reduction step to insensitive to $pO_2$ for the re-oxidation step (Figure 22 (a)), and it is believed to have originated from time-dependent surface contamination during measurement. On the other hand, $k_{chem}$ at the reduction step for Sample II at 600 °C and 650 °C is only weakly dependent on $pO_2$, while $k_{chem}$ at the oxidation steps for these temperatures showed weaker $pO_2$ dependence ($m = \sim 0.37$) compared to Sample III ($m = 0.50 \sim 0.55$) (Figure 22 (b) and (c)). These weaker or insensitive $pO_2$ dependences indicate that the oxygen species in the RDS changes from diatomic to atomic oxygen species or the RDS becomes a charge transfer dominant process.

It is well known that Si, suspected to come from refractories or glass tubing, significantly decreases oxygen ion grain boundary conductivity and as well blocks oxygen exchange at the surface [110]. CaO surface coverage has also been shown to have a deleterious effect on surface oxygen exchange in yttria stabilized zirconia, and has previously been observed on ceria based oxide surfaces [111,112]. The source of Na is generally known to be from manual handling or due to contact with a dirty surface such as lab

bench. Because Sample III did not show Si contamination (Table 3) and the observed impurity concentration profile from SIMS measurement extended from the gas interface into the bulk (Figure 71), gas transport from outside (e.g. furnace insulation composed of minerals often containing Si, K, Na, and Ca) is more likely to be the source of contamination rather than bulk diffusion from the substrate. Trace amounts of the contaminants can be introduced into the measuring chamber, and under high temperature (and over many days), became volatile and deposited on the film surface. Quartz tubing, used as the measuring chamber, can be considered as well. Because the main ingredients of the ceramic paste are found, from its material safety data sheet (MSDS), to be $Al_2O_3$, sodium silicate, $SiO_2$ and water, it can also be considered as a potential source. But, this is less likely since Sample I showed Si contamination without use of the ceramic paste while Sample III did not show it even with the ceramic paste used in the assembly.

The negative impact of impurities (Si, Na and Ca) on the reaction kinetics was clearly confirmed by reexamining specimens following surface etching. For example, $k_{chem}$ of Sample II was enhanced by 1 ~ 2.5 orders of magnitude depending on $pO_2$ after HF etching (Table 5 and Figure 47). Figure 72 shows that $k_{chem}$ of etched Sample II reaches close to or above values obtained for Sample III which are believed to be close to ones expected for uncontaminated PCO surfaces. The $pO_2$ dependence of $k_{chem}$ recovered to a power law of $m = 0.73 \sim 0.84$, which is even stronger than Sample III ($m = 0.50 \sim 0.55$). It is worthwhile noting that the surface roughness changed little due to HF etching (from $4.13 \pm 1.38$ nm to $3.77 \pm 0.13$ nm, Figure 43 and Figure 44) so that enhancement in $k_{chem}$ cannot be due to an increase in surface area.
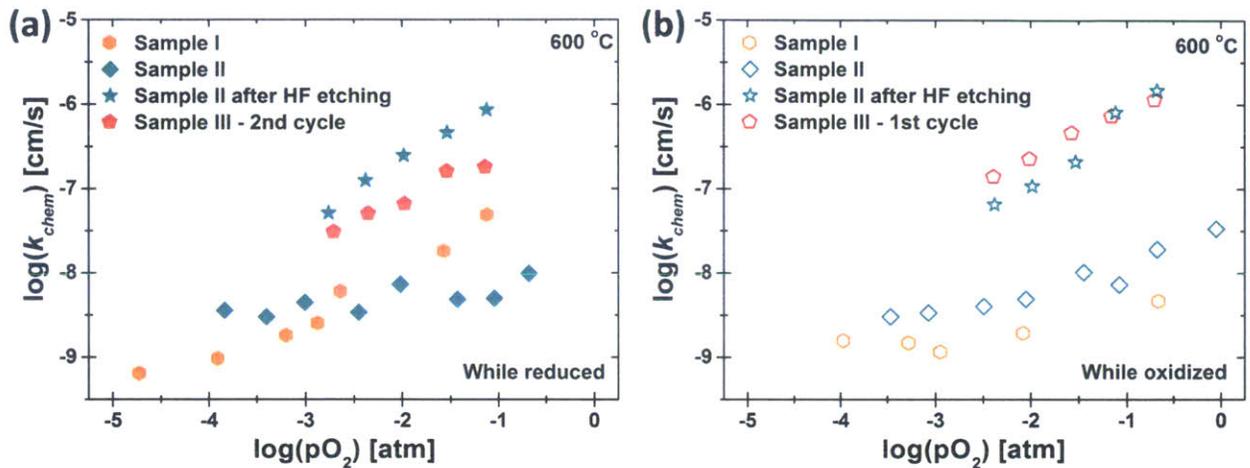
**Figure 72.** Plot of $k_{chem}$ from optical relaxation versus $pO_2$ for Sample I, II and III at 600 °C obtained while reduced (a) and oxidized (b). $k_{chem}$ for HF etched Sample II are added to Figure 69. $k_{chem}$ values are plotted using the final $pO_2$ value for each relaxation step. For Sample III, values from 1st cycle are plotted.

### 4.3.3 Electrochemical oxygen surface exchange reaction mechanisms

Contrary to strictly chemically-driven oxygen incorporation reactions, electrochemical reactions include electrical potentials as a driving force, as monitored during EIS measurements. In this case, electrons are supplied by the metal current collectors, even though electron transfer to the oxygen adsorbates can actually occur at the electrode surface. Figure 73 illustrates the reaction pathways for the electrochemical oxygen reduction reaction at a structure in which PCO is placed between the porous Pt current collector and the electrolyte. Two possible pathways can be considered. As shown in Figure 73 (a), one pathway can involve oxygen incorporation across the PCO electrode - gas atmosphere interface, assuming that Pt does not have any catalytic effect for charge transfer or provide preferential adsorption sites. In this case, the Pt metal offers a means for imposing an electrical potential and to supply electrons from the external circuit. Electrons are transported to the actual reaction site by electronic conduction through PCO rather than through the Pt. On the other hand, in Figure 73 (b) it is assumed that electron transfer to the oxygen adsorbates can be enhanced by the catalytic activity of Pt. Here oxygen incorporation is largely constricted to the triple phase boundaries, where the gas, the Pt current collector and PCO electrode meet together. In this case, adsorption and surface diffusion on Pt and PCO can

112

compete with each other. Because PCO is a MIEC electrode and all of the surface area of PCO can be active to the oxygen exchange reaction [69], the triple phase boundaries between the gas, PCO electrode and the electrolyte are generally not considered as the preferred reaction site. On the other hand, the electronic conductivity in PCO is much lower than that in the more well-known MIECs such as LSC or LSF and so the triple phase boundary at the Pt/PCO/air interface may be playing a more important role than initially expected.
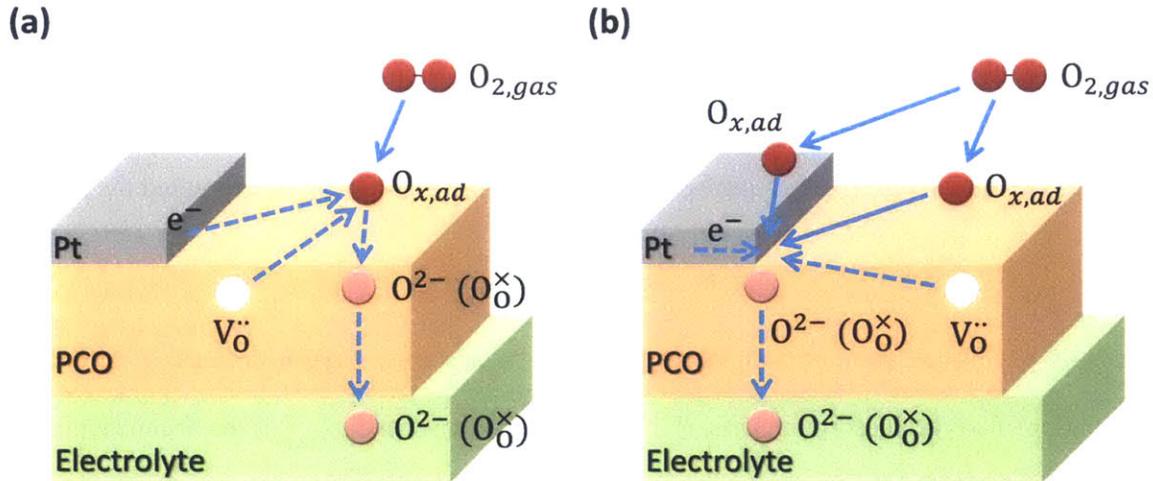


**Figure 73. Macroscopic reaction pathways involving (a) the boundary between PCO electrode and the gas atmosphere and (b) the triple phase boundaries between the gas, the Pt current collector and PCO electrode.**

As shown in Figure 31 and Figure 32, log ($k_{elec} \propto 1/ASR$) vs. log ($pO_2$) of Sample II and III go through maxima at $pO_2 = 10^{-2} \sim 10^{-3}$ atm, with a negative $pO_2$ dependence in the high $pO_2$ regime ($m = -0.64 \sim -0.94$) and a positive $pO_2$ dependence in the low $pO_2$ regime ($m = 0.39 \sim 0.65$), while $k_{chem}$ for the same samples did not exhibit maxima. A maximum in log ($k_{elec}$) – log ($pO_2$) plot is not usually found for other MIEC cathode materials. Generally, $k_{elec}$ shows a monotonic positive $pO_2$ dependency at high $pO_2$ regime [103]. On the other hand, in theoretical considerations by Fleig et al [97], they show that the effective $k$ ($\propto 1/ASR$) can exhibit a maximum in log($k$) – log($pO_2$) if the surface coverage ($\theta$) of the adsorbed oxygen species plays a key role in the overall reaction. Under these circumstances, $k_{elec}$ can be expected to follow a Langmuir-type isotherm, i.e. $\theta/(1-\theta) \approx pO_2^n$ as well.

An alternative explanation is that the Pt current collector takes part in the reaction kinetics. (Figure 73 (b)). In fact, it is well known that the log (1/electrode resistance) vs. log (pO2) plot for Pt/YSZ and Pt/doped ceria systems goes through a maximum, when surface diffusion of adsorbed oxygen species on the Pt surface is the RDS [113–115]. As shown in Figure 74, the electrode conductivity shows a maximum at higher temperatures ($\geq 500$ °C), which can be explained by the availability of adsorbed oxygen species supplied by surface diffusion to the reaction sites (TPB region of gas, Pt and electrolyte), and its maximum shifts toward lower pO2 when temperature decreases. In addition, the activation energy for the conductance at the low pO2 side of the maximum is smaller than that of the high pO2 side. At lower temperatures, the governing reaction switches to the dissociative adsorption of oxygen molecules on the Pt surface. The flux of adsorbed oxygen species by surface diffusion, $j$, can be expressed by

$$j = -\lambda c\theta(1-\theta)\frac{\partial \mu_{O_{x,ad}}}{\partial x} \tag{46}$$

where $\lambda$ is a constant proportional to the mobility of adsorbed oxygen species, $c$ is the surface concentration of oxygen adsorption sites, $\theta$ is the surface coverage and $\mu_{O_{x,ad}}$ is the chemical potential of adsorbed oxygen species on the surface, respectively. Assuming that the surface coverage ($\theta$) of adsorbed oxygen species follows the Langmuir-type isotherm and their surface diffusion on the Pt surface is the RDS, the following relationships between the electrode conductivity $\sigma_E$ and pO2 can be derived for atomic oxygen adsorbed species ($a_O = \sqrt{pO_2}$, Equation 47(a)) and for diatomic oxygen adsorbed species ($a_{O_2} = pO_2$, Equation 47(b)), respectively [114].

$$\sigma_E = 4\sigma_E^{\circ}\frac{a_O^{\circ} \cdot \sqrt{pO_2}}{\left(a_O^{\circ} + \sqrt{pO_2}\right)^2} \tag{47a}$$

$$\sigma_E = 4\sigma_E^{\circ}\frac{a_{O_2}^{\circ} \cdot pO_2}{\left(a_{O_2}^{\circ} + pO_2\right)^2} \tag{47b}$$

where $a_O^{\circ}$ and $a_{O_2}^{\circ}$ are the activity of the adsorbed oxygen species at the optimal pO2 when $\theta = \frac{1}{2}$ and $\sigma_E$ reaches its maximum value, $\sigma_E^{\circ}$.

114
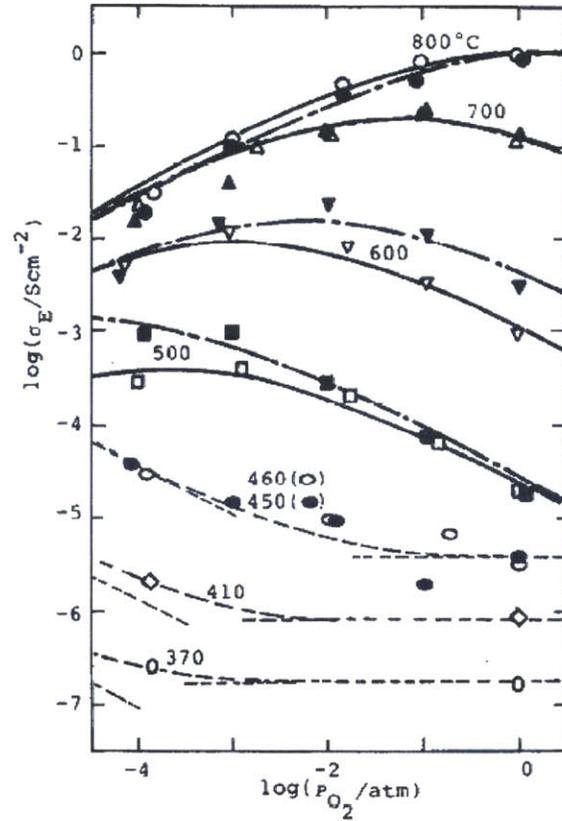
**Figure 74.** pO₂ and temperature changes of $\sigma_E$ (electrode conductivity) for Pt/YSZ samples with various preparation procedure (Details can be found in the reference [113]). Fitting curves for experimental data (dots) for above 500 °C are derived from surface diffusion controlled kinetics (Equation 47(a) in this thesis), while ones for lower temperatures are derived from oxygen dissociative adsorption controlled kinetics. Reprinted from reference [113].
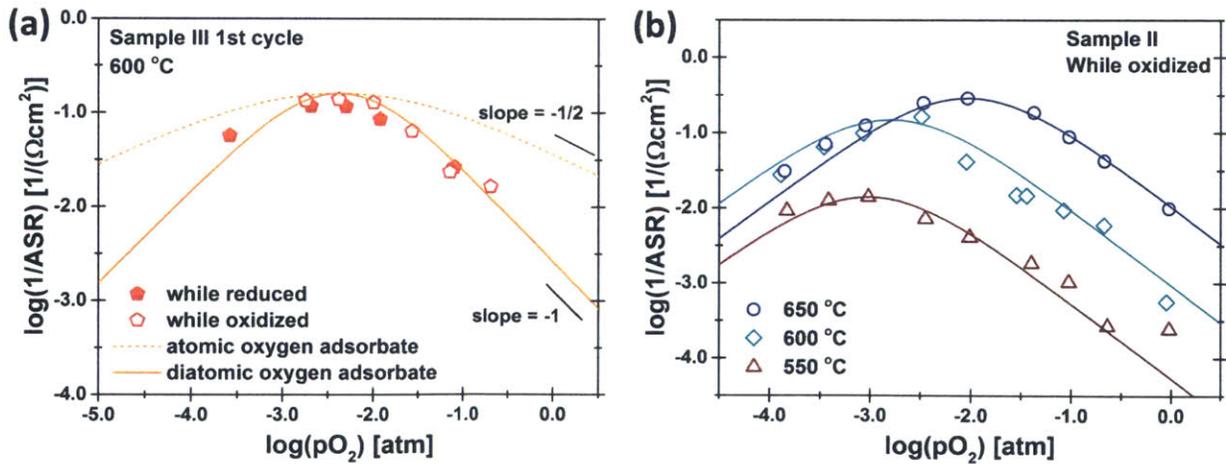


**Figure 75.** Plot of 1/ASR from EIS measurement versus pO₂ for (a) Sample III at 600 °C and (b) Sample II at 550 - 650 °C. Dotted and solid lines are fitting curves derived from surface diffusion controlled kinetics of atomic and diatomic oxygen adsorbates (Equation 47), respectively.

Figure 75 (a) shows log (1/ASR) vs. log (pO₂) of Sample III derived from EIS measurements. The experimental data show a better fit with the model derived with diatomic oxygen adsorbed species (Equation 47(b)), characterized by a slope of ± 1, apart from the maximum, than the one with atomic oxygen adsorbed species (Equation 47(a), slope = ± ½). Furthermore, (1/ASR) data from Sample II at various temperatures fit well to Equation 47(b), and the temperature dependence of the $pO_2$ at the maximum and smaller activation energy at low $pO_2$ side agree with the trend found in the literature (Figure 74). This is consistent with the hypothesis that surface diffusion of diatomic oxygen adsorbates to the gas/Pt/PCO TPB region becomes the RDS in the Pt/PCO/YSZ system (Figure 76 (a)). On the other hand, as proposed by Hertz in his Ph.D. thesis [116], the oxygen exchange reaction at the TPB region can also be considered as the RDS. Similar to the diffusion process on the Pt surface, the exchange reaction at the TPB involves the breaking of a Pt-O bond and following migration of the freed O to a neighboring vacant site (Figure 76 (b) and Equation (48)), and its $pO_2$ dependence would follow Langmuir-type $\theta /(1 - \theta)$ isotherm as well. Given that the impedance spectra from Pt/PCO/YSZ cells in this study did not show a linear feature with a 45° slope to the real axis, associated with a diffusion process [67], the latter explanation would be more reasonable. In order to confirm which process is more dominant, electrode resistance characteristics can be investigated by varying the surface area of the Pt current collector with fixed TPB length.

$$O_{x,ad}^{\delta-}(Pt, TPB) + V_O^{..}(PCO, TPB) \leftrightarrow V_{ad}(Pt, TPB) + O_O^{x}(PCO, TPB) \qquad (48)$$
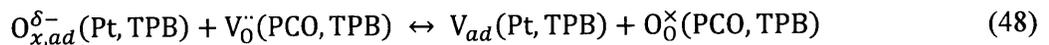
Changes in the controlling reaction kinetics, as characterized by EIS vs optical relaxation measurements, may explain why $k_{elec}$ is less sensitive to surface impurities than $k_{chem}$. Because oxygen is supplied by surface diffusion of adsorbates on the Pt current collector, the surface characteristics of the PCO surface play more of a minor role as long as the TPB region is not substantially blocked by surface impurities.
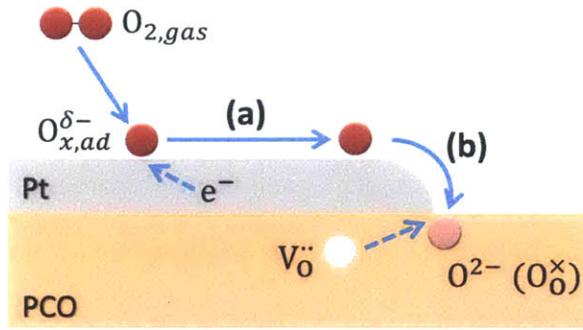
**Figure 76. Macroscopic reaction pathway when the Pt current collector takes part in the reaction. Possible rate determining steps (RDS) are (a) the surface diffusion of oxygen adsorbates on Pt current collector to the triple phase boundaries (TPB) between the gas, the Pt current collector and PCO electrode and (b) the oxygen exchange reaction at the TPB region.**

The activation energy for surface diffusion of diatomic oxygen adsorbates can be estimated by plotting log $(\sigma_E^\circ)$ vs. $1/T$, because the temperature dependence of concentration term is not included for $\sigma_E^\circ$ at $\theta = \frac{1}{2}$. From the slope of the plot for Sample II in Figure 75 (b), the activation energy for diatomic oxygen species diffusion is estimated to be $1.99 \pm 0.57$ eV (Figure 77 (a)), in reasonable agreement with reported values of $1.52 \sim 1.78$ eV for atomic oxygen diffusion on Pt [113]. The Langmuir adsorption of diatomic oxygen adsorbates ($O_{2,gas} + V_{ad} \leftrightarrow O_{2,ad(Pt)}$) and the equilibrium constant ($K$) of the reaction can be expressed as below.

$$\theta/(1 - \theta) = K \cdot pO_2 \tag{49}$$

$$K = K_0 \, exp\left(-H_{ad}/kT\right) \tag{50}$$

where $K_0$ is a pre-exponential constant and $H_{ad}$ is the adsorption enthalpy of diatomic oxygen adsorbates on the Pt surface, respectively. Combining Equation 49 and 50, $pO_2$ at $\theta = \frac{1}{2}$ can be given by

$$pO_2^* \, (at \, \theta \, = \, \frac{1}{2}) \, = K_0^{-1} exp\left(H_{ad}/kT\right) \tag{51}$$

Therefore, from the slope of the log $(pO_2^*)$ vs. $1/T$, a value of $1.47 \pm 0.52$ eV of $H_{ad}$ can be derived (Figure 77 (b)). The reported values for the adsorption enthalpy of oxygen adsorbate on Pt are $1.95 \sim 2.30$ eV [113]. The activation energies of diffusion and adsorption can vary depending on characteristics of

adsorption (chemi- or physi-sorption), adsorbates (molecular or dissociative / charged or uncharged) and surface chemistry (nature of impurities and/or oxidation state of Pt, i.e. $PtO_x$ or Pt).

Interestingly, Sample I shows only a positive $pO_2$ dependence of $k_{elec}$; $m = 1.01 \pm 0.06$ ($< 10^{-3}$ atm $pO_2$) and $m = 0.29 \pm 0.03$ ($> 10^{-2}$ atm $pO_2$), even though a porous Pt current collector was used as for Sample II and III (Figure 29 (b)). This might have originated from low adsorption coverage, implying that $\theta$ did not reach a value of ½ even at high $pO_2$. One could hypothesize that this could be due to heavier surface contamination of Sample I (highest Si composition among samples in Table 3). Alternatively, the difference may be related to the different annealing history of two specimens.
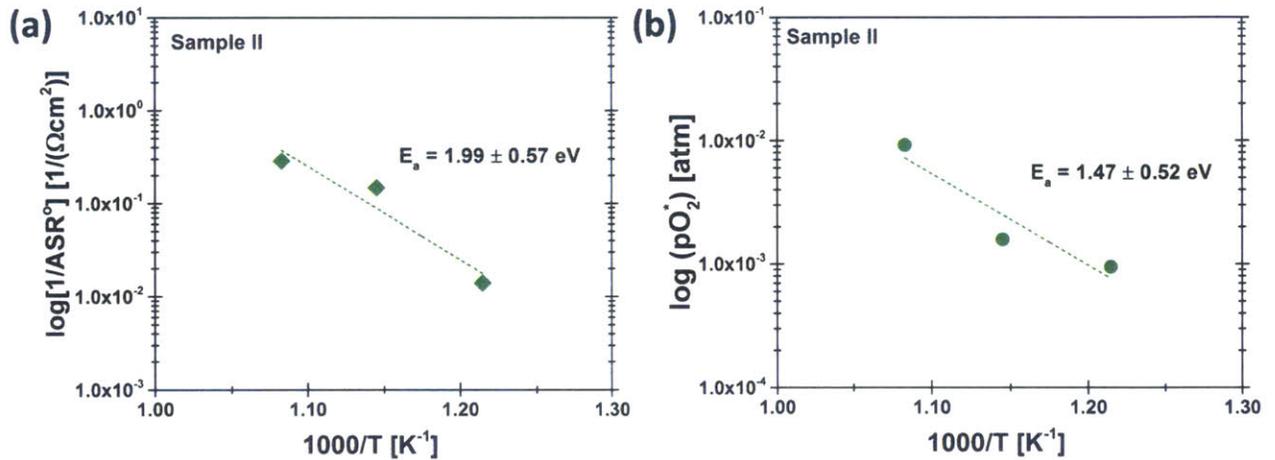


**Figure 77. Temperature dependence of (a) $1/ASR^o$, i.e. $\sigma_E^\circ$, and (b) $pO_2^*$ at $\theta = $ ½ for Sample II from Figure 75 (b).**

### 4.3.4 Comparison of $k_{chem}$ with $k_{elec}$

The thermodynamic factor $w$ derived by Weppner et al [117], for the case of a system dominated by one electronic and one ionic species is given by

$$w = t_e \frac{\partial \ln a_{i^*}}{\partial \ln c_{i^*}} \tag{52}$$

where $t_e$, $a_{i^*}$ and $c_{i^*}$ represent the electron transference number ($\sigma_e/\sigma_{total}$), activity and the concentration of neutral $i$ species ($i^*$), respectively. Utilizing this thermodynamic factor, the oxygen

surface exchange rate constants derived by chemical and electrical routes ($k_{chem}$ and $k_{elec}$, respectively) can be correlated to each other, as long as the same reaction mechanism operates [29,30].

$$k_{chem} = t_e \frac{\partial \ln a_O}{\partial \ln c_O} k_{elec} = t_e \frac{1}{2} \frac{d \ln(pO_2)}{d \ln([O_O^\times])} k_{elec} \tag{53}$$

where $[O_O^\times]$ is molar oxygen concentration computed from a previously derived thin film defect equilibria model [68]. Assuming that electronic conduction through the conduction band is negligible in the $pO_2$ range of interest in this study (1 atm – $10^{-5}$ atm) [65], $t_e$ can be calculated by considering only the contributions of oxygen vacancies ($\sigma_{V_O^{..}}$) and Pr small polarons ($\sigma_{Pr_{Ce}}$) (Figure 78 (a)). In the calculation, all defect concentration are derived from the thin film defect model [68], while parameters for mobilities are obtained from an analysis of bulk transport properties of PCO [65].
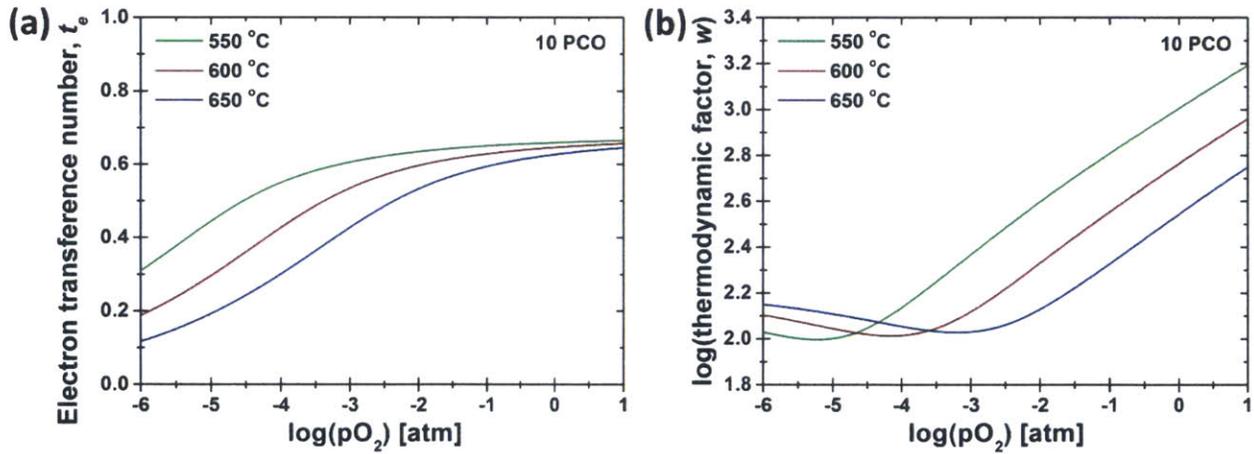


**Figure 78. (a) The electron transference number derived from the PCO thin film defect model. (b) thermodynamic factor, $w$, calculated based on parameters derived from the defect model.**

Figure 79 to Figure 81 summarize all the surface exchange coefficients obtained in this study from Sample I, II and III, respectively; $k_{chem}$ from optical relaxation, $k_{elec}$ from EIS measurement and estimated $k_{chem}$ from $k_{elec}$ and the thermodynamic factor $w$ using Equation (53). In the case of $k_{chem}$, values are plotted based on the final $pO_2$ values reached following each relaxation step. For all samples, we find that $k_{chem}$, estimated from $k_{elec}$ and $w$, are a factor of ten to a hundred larger than $k_{chem}$ extracted from the optical relaxation measurements.

Three possible origins of this discrepancy between $k_{chem}$ and $k_{elec}$ can be considered as follows. First of all, $k_{chem}$ measured from optical relaxation measurement were found often to be degraded from the values obtained for "clean" materials. The presence of surface contamination on the exposed PCO surface used in the optical transmission measurements, and their negative impact on the oxygen exchange reaction, were discussed above. Second, the potential catalytic activity of the Pt current collector could be another potential source for the larger $k_{chem}$ values derived from ASR measurements in addition to changes in the RDS of the reaction kinetics. Lastly, the validity of the use of Equation (53) and of the derivation of the thermodynamic factor in the equation is questionable. Equation (53) is derived under an assumption that $k_{chem}$ and $k_{elec}$ share the same reaction mechanism, i.e. the same RDS [118]. However, the different $pO_2$ dependence of $k_{chem}$ and $k_{elec}$ in this study indicates that the oxygen exchange reaction is governed by different elementary steps for these experiments. In addition, defect concentrations used to calculate the thermodynamic factor, which were obtained from the defect model for the film bulk, may not represent the surface characteristics of the thin films. The defect chemistry at the film surface can be different from that characteristics of the film bulk. For example, as found from XPS measurement (Figure 41), Pr concentrations near the film surface (0.26 ~ 0.32) were higher than that in the film bulk (~0.10). For a comparison of the potential impact of different Pr concentration on the thermodynamic factor, calculations of $w$ for 20PCO based on the 20PCO bulk defect model [66] are shown in Figure 82 (a). A smaller $w$ is found in the high $pO_2$ regime that would cause up to a 50% decrease in $k_{chem}$ extracted from $k_{elec}$ and $w$, as illustrated in Figure 82 (b). Even though this modification is still smaller than the discrepancy between derived $k_{chem}$ values, its impact goes in the right direction (by decreasing the discrepancy) and it may be larger when higher Pr concentrations on the surface are considered.
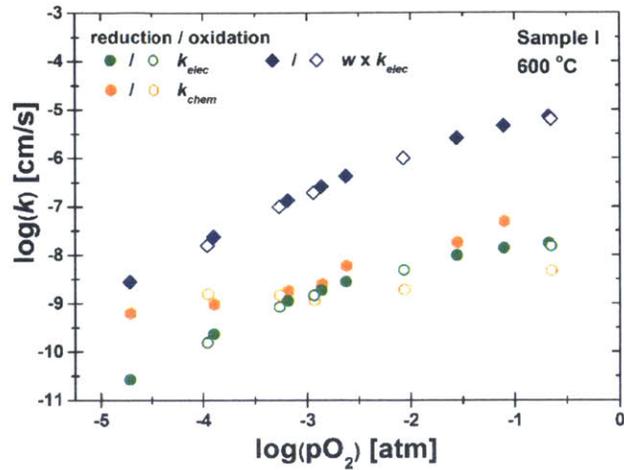
**Figure 79. Plot of $k_{chem}$ from optical relaxation, $k_{elec}$ from EIS measurement and estimated $k_{chem}$ derived from $k_{elec}$ (with aid of thermodynamic factor, $w$) versus $pO_2$ from Sample I. $k_{chem}$ from optical relaxation is plotted using the final $pO_2$ value for each relaxation step.**
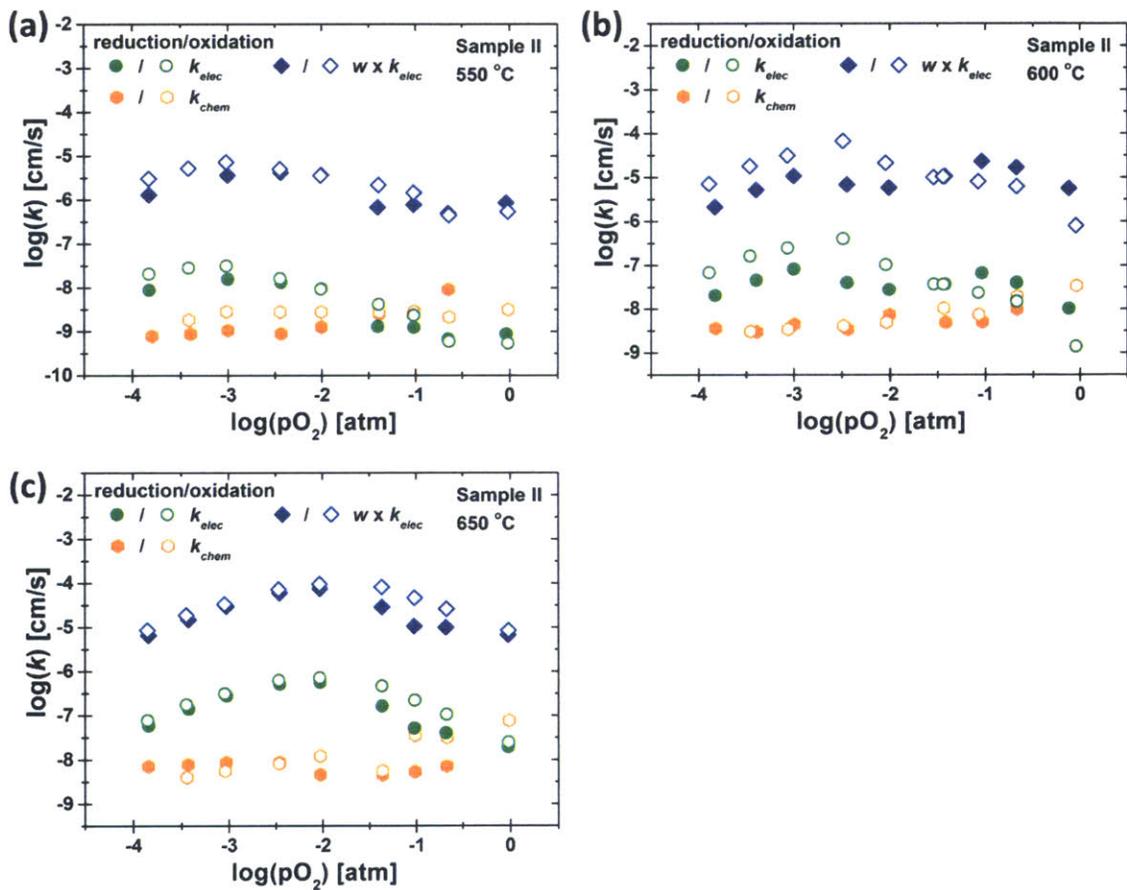


**Figure 80. Plot of $k_{chem}$ from optical relaxation, $k_{elec}$ from EIS measurement and estimated $k_{chem}$ derived from $k_{elec}$ (with aid of thermodynamic factor, $w$) versus $pO_2$ from Sample II at 550 °C (a), 600 °C (b) and 650 °C (c). $k_{chem}$ from optical relaxation is plotted using the final $pO_2$ value for each relaxation step.**
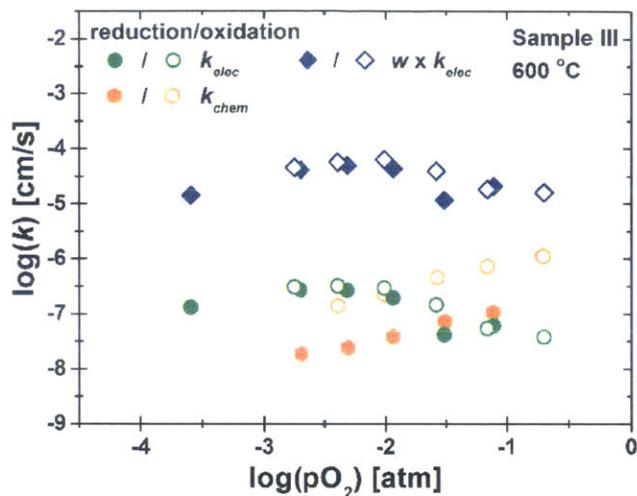
**Figure 81.** Plot of $k_{chem}$ from optical relaxation, $k_{elec}$ from EIS measurement and estimated $k_{chem}$ derived from $k_{elec}$ (with aid of thermodynamic factor, $w$) versus pO$_2$ from Sample III (1$^{st}$ cycle of reduction-oxidation). $k_{chem}$ from optical relaxation is plotted using the final pO$_2$ value for each relaxation step.
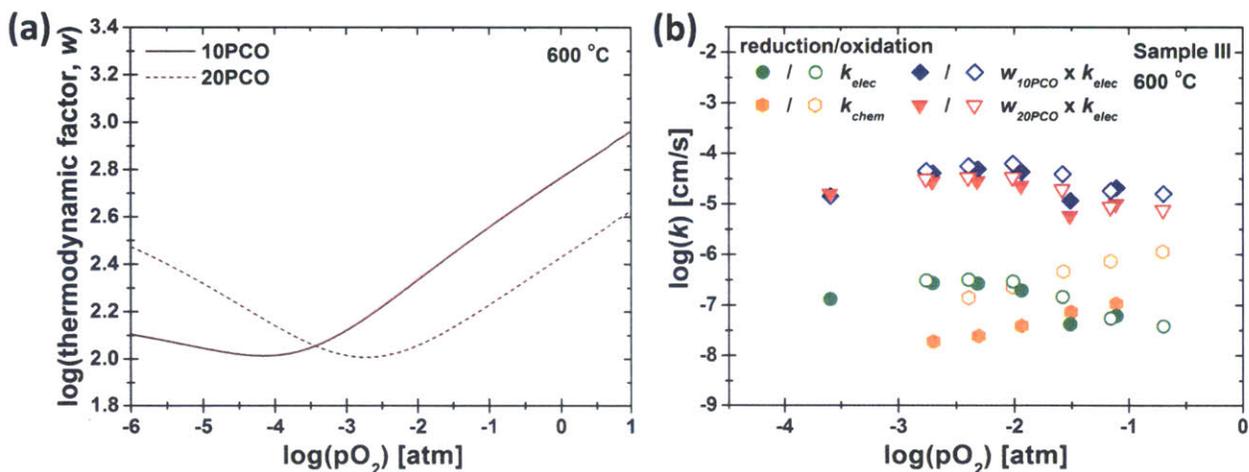


**Figure 82.** (a) Thermodynamic factor ($w$) for 10PCO and 20PCO calculated based on parameters derived from the defect model. (b) Plot of $k_{chem}$ from optical relaxation, $k_{elec}$ from EIS measurement and estimated $k_{chem}$ derived from $k_{elec}$ (with aid of thermodynamic factor, $w$, *from 10PCO and 20PCO*) versus pO$_2$ from Sample III (1$^{st}$ cycle of reduction-oxidation). $k_{chem}$ from optical relaxation is plotted using the final pO$_2$ value for each relaxation step.

## 4.4 Investigation of oxygen chemical diffusion via color front motion

The reaction kinetics in thin film structures are generally limited by the surface exchange reaction because of the short diffusion lengths in films coupled with quite high oxygen diffusivities. Indeed, as discussed above (section 1.6.2), diffusion-control should become relevant only above the critical length $(L_C = D/k)$; for PCO, $\sim 10^3$ $\mu$m at 550 - 670 °C. However, by limiting the exchange reaction to occur only at a confined regions or edges and blocking oxygen exchange over most of the area of the film, the diffusion kinetics can be studied by monitoring lateral color front motion along the length of the film from the access point to some distance away from that point. With a special cell structure designed to extend the oxygen diffusion pathway (Figure 11), this study demonstrates that oxygen chemical diffusion in MIEC oxide thin film can be investigated with the aid of color absorbing centers which change their absorptivity with a corresponding change in oxidation state as is the case for Pr in $CeO_2$. While the isotope exchange experiment that uses SIMS to determine the tracer diffusion profile can be used for this purpose, it requires costly instrumentation, is *ex situ* and destructive to the specimen. In contrast, optical color front motion experiments can be done *in situ, reversibly* and more rapidly. Furthermore, additional variables such as electrical potential and catalyst decoration can be easily and even locally accommodated.

# CHAPTER 5. CONCLUSION

## 5.1 Summary

This dissertation described research into methods for investigating the defect chemical thermodynamics and surface exchange kinetics in oxide thin film structures. This was achieved by developing a novel characterization apparatus, enabling joint *in situ* and *in operando* optical absorption and electrochemical impedance spectroscopy (EIS) measurements and spatially resolved color front motion studies. The characterization techniques and the information achieved in this research are essential for the design of more efficient and stable electrodes, key components of solid oxide fuel cells (SOFCs) [6,7], solid oxide electrolysis cells (SOECs) [119], water-splitting devices [120–122], and metal-air batteries [123,124] given the central role played by the oxygen reduction reaction in all of these devices.

Dramatic changes in the optical absorptivity of $Pr_xCe_{1-x}O_{2-\delta}$ (PCO) thin films, resulting both from variations in Pr concentration and oxidizing/reducing treatments, were observed and correlated to the electronic structure and oxidation state of Pr within the material. The Pr impurity levels allow for sub-band gap optical transitions (2.0 – 3.3 eV), leading to the red coloration of oxidized PCO. By exposing PCO to reducing conditions, the optical transitions are suppressed due to the conversion of $Pr^{4+}$ to $Pr^{3+}$ (i.e. filled impurity levels).

A novel investigation method for simultaneously performing *in situ* and *in operando* optical absorption and EIS measurements was developed in this study and utilized, *for the first time*, at elevated temperatures and controlled atmospheres, on metal oxide thin films (PCO) exhibiting variable oxygen nonstoichiometry ($\delta$). Conventional characterization methods are often severely limited when applied to thin films due to their inherent high aspect ratio and low mass. On the contrary, this novel arrangement allows one to investigate the thermodynamics and reaction kinetics of oxide thin films, which often differ from those of bulk materials, and could be influenced by other factors such as metal contacts, strain and thermal history.

The absorption coefficient of the $Pr^{4+}$ color center, extracted from optical absorption measurements, was found to exhibit an expected linear dependence on $Pr^{4+}$ concentration, as correlated with $\delta$ values obtained independently by chemical capacitance measurements, within the experimental conditions of this study (550 – 700 °C and $10^{-4}$ – 1 atm $pO_2$). This allowed for the derivation of the extinction coefficient for $Pr^{4+}$ ($\varepsilon_{Pr^{4+}} = 6.37 \pm 0.05 \times 10^{-18}$ cm$^2$), thereby opening up future opportunities for investigating defect concentrations and nonstoichiometry in PCO and other appropriate thin films from optical studies alone. This could be especially important at reduced temperatures where meaningful $C_{chem}$ measurements may not be possible. In addition, $Pr^{4+}$ concentrations estimated only from optical measurement were found to be consistent with ones derived from chemical capacitance measurements, validating the thin film defect model for 10PCO.

The non-contact optical relaxation measurement provides an important means for investigating the surface exchange reaction kinetics of the "innate" surface of a material. Surface sensitive measurements like XPS and AES revealed that the surfaces of the PCO thin films were susceptible to contamination with elements such as Bi, Na, Si and Ca, introduced during sample preparation and high temperature measurements and/or treatments. This change in surface chemistry was found to have significant impact on reaction kinetics with changes in oxygen surface reaction constants ($k_{chem}$) of up to two order of magnitude. Therefore, in order to keep the electrode surface active, an impurity tolerant electrode needs to be designed, for example, by introducing additives capable of reacting and thereby neutralizing the impurities [125]. Pr was also found to segregate to the surface of the PCO films, of potential benefit for the surface exchange reaction, by creating a higher oxygen vacancy and electronic carrier concentration at the surface.

The presence of the Pt current collector at the PCO surface was found to significantly alter the oxygen surface exchange kinetics, in some cases showing an unexpected maximum in the log ($k_{elec}$) – log ($pO_2$) dependence believed to be due to a Langmuir-type adsorption isotherm. Based on this observation, surface diffusion of diatomic oxygen adsorbates to the gas/Pt/PCO triple phase boundary region was proposed as the RDS. The activation energy for diatomic oxygen species diffusion was estimated to be

2.07 ± 0.57 eV, while the adsorption enthalpy was calculated to be 1.47 ± 0.52 eV. This suggests that the surface coverage and migration of oxygen adsorbates on metal contacts should be considered when evaluating the reaction kinetics of MIEC electrodes by electrical and electrochemical measurements, and ultimately designing the SOFC cell structure for better performance.

Given that the defect model for PCO thin films was validated by our $C_{chem}$ and optical measurements, the thermodynamic factor, $w$, could be calculated from the model. Because the oxygen surface exchange rate constants, derived by chemical and electrical routes ($k_{chem}$ and $k_{elec}$, respectively), were obtained for the same sample under the same environmental condition, they could be correlated to each other, in princliple, with the aid of $w$, allowing a unique opportunity to test the validity of the use of $w$. $k_{chem}$ measured by optical relaxation measurements was found to be smaller than $k_{chem}$ derived from an analysis of $k_{elec}$ and $w$. The origin of this discrepancy in derived $k_{chem}$ values was proposed to be due to a deterioration in $k_{chem}$ caused by impurity contaminated surface and potentially enhanced $k_{elec}$ due to catalytic effects coming from the Pt contact. In addition, the validity of defect concentrations used for the calculation of the thermodynamic factor need re-consideration given that the defect chemistry at the film surface can deviate significantly from that of the film bulk. Therefore, comparison and/or conversion between $k_{chem}$ and $k_{elec}$ with the aid of $w$ may not be valid in general.

Color front motion in surface passivated PCO films was used to investigate diffusion kinetics within the plane of the films. This was enabled by a special cell structure designed to extend the oxygen diffusion pathway and the use of a heater stick enabling the close approach of the microscope lens. Optical color front motion experiments can be done *in situ* and faster than common alternative methods such as SIMS following exposure to an $^{18}O$ tracer. In addition, it allows one to have a spatially resolved map of a material's properties.

In this dissertation, the *in situ* optical measurement technique was introduced as a versatile tool for investigating the defect chemical ($\delta$) and the reaction kinetic properties ($k$, $D$) of oxide thin film structure, information essential to predicting enhanced performance of oxide-based devices. Specifically optical absorption associated with the Pr oxidation state in PCO model dense thin films was studied for this

purpose. The use of this technique can be extended to other oxide thin films which have proper absorbing centers for example, $Fe^{4+}$ in $Sr(Ti,Fe)O_{3-\delta}$. Furthermore, even if there is no color center, other oxide thin films can be investigated by preparing a multilayer structure composed of the interested oxide as the top layer and the PCO film at the bottom as a color indicator. In addition, the local nature of optical measurement can provide the ability to investigate spatially resolved material's properties. Therefore, the combination of high throughput combinatorial fabrication methods [122,126,127], with *in situ* optical measurements can serve as a rapid screening technique, thereby realizing efficient development of highly performing devices.

## 5.2 Recommendations for future works

There are a number of questions raised by this work. The followings are some of the more promising avenues that are recommended for future study:

- Investigate optical band-gap energy change of PCO thin film as a function of temperature.

- Apply an electrical potential across the YSZ support to vary the oxidation state of the PCO thin film and monitor change in its optical absorption.

- Investigate the chemical diffusion in PCO thin films; color front motion with electrical potential and catalyst decoration.

- Investigate reaction kinetics of other materials by using optical changes of PCO thin films as an indicator.

# REFERENCES

[1]     B. C. H. Steele, A. Heinzel, Nature 414 (2001) 345–52.

[2]     S. M. Haile, Acta Mater. 51 (2003) 5981–6000.

[3]     A. Bieberle-Hütter, D. Beckel, A. Infortuna, U. P. Muecke, J. L. M. Rupp, L. J. Gauckler, et al., J. Power Sources 177 (2008) 123–130.

[4]     A. Kundu, J. H. Jang, J. H. Gil, C. R. Jung, H. R. Lee, S. H. Kim, et al., J. Power Sources 170 (2007) 67–78.

[5]     D. J. L. Brett, A. Atkinson, N. P. Brandon, S. J. Skinner, Chem. Soc. Rev. 37 (2008) 1568–1578.

[6]     E. D. Wachsman, K. T. Lee, Science 334 (2011) 935–9.

[7]     E. D. Wachsman, T. Ishihara, J. Kilner, MRS Bull. 39 (2014) 773–779.

[8]     E. Ivers-Tiffée, A. Weber, D. Herbstritt, J. Eur. Ceram. Soc. 21 (2001) 1805–1811.

[9]     M. Mogensen, K. Kammer, Annu. Rev. Mater. Res. 33 (2003) 321–331.

[10]    J. Richter, P. Holtappels, T. Graule, T. Nakamura, L. J. Gauckler, Monatshefte Fur Chemie. 140 (2009) 985–999.

[11]    R. J. Gorte, J. M. Vohs, Annu. Rev. Chem. Biomol. Eng. 2 (2011) 9–30.

[12]    E. Baur, H. Preis, Zeitschrift Für Elektrochemie Und Angew. Phys. Chemie. 43 (1937) 727.

[13]    N. P. Brandon, S. Skinner, B. C. H. Steele, Annu. Rev. Mater. Res. 33 (2003) 183–213.

[14]    A. Evans, A. Bieberle-Hütter, J. L. M. Rupp, L. J. Gauckler, J. Power Sources 194 (2009) 119–129.

[15]    L. Wang, R. Merkle, J. Maier, J. Electrochem. Soc. 157 (2010) B1802.

[16]    J. Fleig, Annu. Rev. Mater. Res. 33 (2003) 361–382.

[17]    S. B. Adler, J. Electrochem. Soc. 143 (1996) 3554.

[18]    S. P. Jiang, Solid State Ionics 146 (2002) 1–22.

[19]    H. Kamata, A. Hosaka, J. Mizusaki, H. Tagawa, Solid State Ionics 106 (1998) 237–245.

[20]    M. Petitjean, G. Caboche, E. Siebert, L. Dessemond, L.C. Dufour, J. Eur. Ceram. Soc. 25 (2005) 2651–2654.

[21]    A. Petric, P. Huang, F. Tietz, Solid State Ionics 135 (2000) 719–725.

[22]    H. Uchida, S. Arisaka, M. Watanabe, Solid State Ionics 135 (2000) 347–351.

[23]    A. Petric, P. Huang, F. Tietz, Solid State Ionics 135 (2000) 719–725.

[24]    Y. Teraoka, T. Nobunaga, K. Okamoto, N. Miura, N. Yamazoe, Solid State Ionics 48 (1991) 207–212.

[25]    Z. Shao, S. M. Haile, Nature 431 (2004) 170–173.

[26]    Z. Shao, W. Yang, Y. Cong, H. Dong, J. Tong, G. Xiong, J. Memb. Sci. 172 (2000) 177–188.

[27]    S. Švarcová, K. Wiik, J. Tolchard, H. J. M. Bouwmeester, T. Grande, Solid State Ionics 178 (2008) 1787–1791.

[28]    A. Yan, M. Cheng, Y. Dong, W. Yang, V. Maragou, S. Song, et al., Appl. Catal. B Environ. 66 (2006) 64–71.

[29]    J. Maier, Physical Chemistry of Ionic Materials, John Wiley & Sons, Chichester, 2004.

[30]    J. Maier, Solid State Ionics 112 (1998) 197–228.

[31]    J. Fleig, F. S. Baumann, V. Brichzin, H. R. Kim, J. Jamnik, G. Cristiani, et al., Fuel Cells 6 (2006) 284–292.

[32]    W. Jung, H. L. Tuller, J. Electrochem. Soc. 155 (2008) B1194.

[33]    H. L. Tuller, S. J. Litzelman, W. Jung, Phys. Chem. Chem. Phys. 11 (2009) 3023–3034.

[34]    M. Tsuchiya, B. K. Lai, S. Ramanathan, Nat. Nanotechnol. 6 (2011) 282–6.

[35]    I. D. Kim, A. Rothschild, H. L. Tuller, Acta Mater. 61 (2013) 974–1000.

[36]    J. J. Yang, D. B. Strukov, D. R. Stewart, Nat. Nanotechnol. 8 (2013) 13–24.

[37]    D. Dijkkamp, T. Venkatesan, X. D. Wu, S. A. Shaheen, N. Jisrawi, Y. H. Min-Lee, et al., Appl. Phys. Lett. 51 (1987) 619–621.

[38]    D. B. Chrisey, Pulsed Laser Deposition of Thin Films, John Wiley & Sons, 1994.

[39]    T. Venkatesan, J. Phys. D. Appl. Phys. 47 (2014) 034001.

[40]    D. H. Kim, L. Bi, N. M. Aimon, P. Jiang, G. F. Dionne, C. A. Ross, ACS Comb. Sci. 14 (2012) 179–90.

[41]    W. Lai, S. M. Haile, J. Am. Ceram. Soc. 88 (2005) 2979–2997.

[42]    H. L. Tuller, S. R. Bishop, Annu. Rev. Mater. Res. 41 (2011) 369–398.

[43]    K. D. Becker, Solid State Ionics 141-142 (2001) 21–30.

[44]    M. Fox, Optical Properties of Solids, Oxford University Press, New York, 2008.

[45]    S. Gutzov, A. Börger, K. D. Becker, Phys. Chem. Chem. Phys. 9 (2007) 491–6.

[46]    O. Buryy, S. Ubizskii, I. I. Syvorotka, K. D. Becker, Acta Phys. Pol. A. 117 (2010) 184–188.

[47]    M. Kreye, K. D. Becker, Phys. Chem. Chem. Phys. 5 (2003) 2283.

[48]    J. Shi, S. Dlugocz, S. Ganschow, S. G. Ebbinghaus, K. D. Becker, Zeitschrift Für Krist. 226 (2011) 89–92.

[49]    J. Shi, S. G. Ebbinghaus, K. D. Becker, Phys. Chem. Miner. 35 (2007) 1–9.

[50]    J. Shi, S. Ganschow, D. Klimm, K. Simon, R. Bertram, K. D. Becker, J. Phys. Chem. C. 113 (2009) 6267–6274.

[51]    T. He, K. D. Becker, Solid State Ionics 101-103 (1997) 337–342.

[52]    D. Sugak, Y. Zhydachevskii, Y. Sugak, O. Buryy, S. Ubizskii, I. Solskii, et al., J. Phys. Condens. Matter. 19 (2007) 086211.

[53]    D. Sugak, Y. Zhydachevskii, O. Buryy, S. Ubizskii, A. Börger, M. Schrader, et al., Acta Mater. 56 (2008) 6310–6318.

[54]    T. Bieger, J. Maier, R. Waser, Sensors Actuators B. 7 (1992) 763–768.

[55]    M. Leonhardt, R. A. De Souza, J. Claus, J. Maier, J. Electrochem. Soc. 149 (2002) J19 – J26.

[56]    R. Merkle, J. Maier, K. D. Becker, M. Kreye, Phys. Chem. Chem. Phys. 6 (2004) 3633–3638.

[57]    M. Leonhardt, J. Jamnik, J. Maier, Electrochem. Solid State Lett. 2 (1999) 333–335.

[58]    T. Bieger, J. Maier, R. Waser, Solid State Ionics 53-56 (1992) 578–582.

[59]    J. H. Yu, J. S. Lee, J. Maier, Angew. Chem. Int. Ed. 46 (2007) 8992–4.

[60]    F. N. Ingrid Denk, J. Maier, J. Am. Ceram. Soc. 80 (1997) 279–285.

[61]    K. Sasaki, J. Maier, Solid State Ionics 161 (2003) 145–154.

[62]    K. Sasaki, J. Maier, Solid State Ionics 134 (2000) 303–321.

[63]    Y. Zhydachevskii, O. Buryy, D. Sugak, S. Ubizskii, A. Börger, K. D. Becker, et al., J. Phys. Condens. Matter. 21 (2009) 175411.

131

[64] S. K. Mohapatra, S. Wagner, J. Appl. Phys. 50 (1979) 5001–5006.

[65] S. R. Bishop, T. S. Stefanik, H. L. Tuller, Phys. Chem. Chem. Phys. 13 (2011) 10165–10173.

[66] S. R. Bishop, T. S. Stefanik, H. L. Tuller, J. Mater. Res. 27 (2012) 2009–2016.

[67] S. B. Adler, Chem. Rev. 104 (2004) 4791–4843.

[68] D. Chen, S. R. Bishop, H. L. Tuller, Adv. Funct. Mater. 23 (2013) 2168–2174.

[69] D. Chen, S. R. Bishop, H. L. Tuller, J. Electroceramics 28 (2012) 62–69.

[70] B. C. H. Steele, Solid State Ionics 75 (1995) 157–165.

[71] F. S. Baumann, J. Fleig, G. Cristiani, B. Stuhlhofer, H. U. Habermeier, J. Maier, J. Electrochem. Soc. 154 (2007) B931.

[72] J. Jamnik, J. Maier, Phys. Chem. Chem. Phys. 3 (2001) 1668–1678.

[73] T. Kawada, J. Suzuki, M. Sase, A. Kaimai, K. Yashiro, Y. Nigara, et al., J. Electrochem. Soc. 149 (2002) E252.

[74] M. Kakihana, M. Yoshimura, Bull. Chem. Soc. Jpn. 72 (1999) 1427–1443.

[75] J. J. Kim, S. R. Bishop, N. J. Thompson, D. Chen, H. L. Tuller, Chem. Mater. 26 (2014) 1374–1379.

[76] W. Jung, J. J. Kim, H. L. Tuller, J. Power Sources 275 (2015) 860–865.

[77] D. Chen, A. Groß, D. C. Bono, J. Kita, R. Moos, H. L. Tuller, Solid State Ionics 262 (2014) 914–917.

[78] R. Swanepoel, J. Phys. E Sci. Instrum. 16 (1983) 1214–1222.

[79] L. Chen, C. L. Chen, A. J. Jacobson, IEEE Trans. Appl. Supercond. 13 (2003) 2882–2885.

[80] J. Fleig, Solid State Ionics 150 (2002) 181–193.

[81] J. Van Herle, A. J. Mcevov, J. Phys. Chem. Solids 55 (1994) 339–347.

[82] S. Kohiki, T. Ohmura, K. Kusao, J. Electron Spectros. Relat. Phenomena. 31 (1983) 85–90.

[83] J. Crank, The mathematics of diffusion, 2nd ed., Oxford University Press, Oxford, 1983.

[84] C. Mansilla, Solid State Sci. 11 (2009) 1456–1464.

[85] J. J. Kim, S. R. Bishop, N. Thompson, Y. Kuru, H. L. Tuller, Solid State Ionics 225 (2012) 198–200.

[86] T. S. Stefanik, Ph.D. Thesis, Massachusetts Institute of Technology, 2004.

[87] M. Panhans, R. Blumenthal, Solid State Ionics 60 (1993) 279–298.

[88] Y. P. Xiong, H. Kishimoto, K. Yamaji, M. Yoshinaga, T. Horita, M. E. Brito, et al., Solid State Ionics 192 (2011) 476–479.

[89] T. Suzuki, I. Kosacki, H. U. Anderson, Solid State Ionics 151 (2002) 111–121.

[90] W. C. Chueh, S. M. Haile, Phys. Chem. Chem. Phys. 11 (2009) 8144–8.

[91] G. J. la O', S. J. Ahn, E. Crumlin, Y. Orikasa, M. D. Biegalski, H. M. Christen, et al., Angew. Chem. Int. Ed. 49 (2010) 5344–7.

[92] T. S. Oh, Y. S. Tokpanov, Y. Hao, W. Jung, S. M. Haile, J. Appl. Phys. 112 (2012) 103535.

[93] Y. Kuru, S. R. Bishop, J. J. Kim, B. Yildiz, H. L. Tuller, Solid State Ionics 193 (2011) 1–4.

[94] S. R. Bishop, H. L. Tuller, Y. Kuru, B. Yildiz, J. Eur. Ceram. Soc. 31 (2011) 2351–2356.

[95] D. Marrocchelli, S. R. Bishop, H. L. Tuller, B. Yildiz, Adv. Funct. Mater. 22 (2012) 1958–1965.

[96] S. R. Bishop, D. Chen, J. Sheth, S. T. Misture, B. W. Sheldon, J. J. Kim, et al., ECS Trans. 61 (2014) 31–36.

[97] J. Fleig, R. Merkle, J. Maier, Phys. Chem. Chem. Phys. 9 (2007) 2713–2723.

[98] S. B. Adler, X. Y. Chen, J. R. Wilson, J. Catal. 245 (2007) 91–109.

[99] R. Merkle, J. Maier, Phys. Chem. Chem. Phys. 4 (2002) 4140–4148.

[100] R. A. De Souza, Phys. Chem. Chem. Phys. 8 (2006) 890–897.

[101] L. Wang, R. Merkle, Y. A. Mastrikov, E. A. Kotomin, J. Maier, J. Mater. Res. 27 (2012) 2000–2008.

[102] Y. A. Mastrikov, R. Merkle, E. Heifets, E. A. Kotomin, J. Maier, J. Phys. Chem. C. 114 (2010) 3017–3027.

[103] W. C. Chueh, S. M. Haile, Annu. Rev. Chem. Biomol. Eng. 3 (2012) 313–341.

[104] E. Heifets, R. Eglitis, E. Kotomin, J. Maier, G. Borstel, Surf. Sci. 513 (2002) 211–220.

[105] J. Nowotny, T. Bak, C. C. Sorrell, Adv. Appl. Ceram. 104 (2005) 174–180.

[106] Z. A. Feng, F. El Gabaly, X. Ye, Z. X. Shen, W. C. Chueh, Nat. Commun. 5 (2014) 1–9.

[107] W. Jung, H. L. Tuller, Energy Environ. Sci. 5 (2012) 5370.

[108] S. R. Bishop, J. J. Kim, N. Thompson, H. L. Tuller, ECS Trans. 45 (2012) 491–495.

[109] S. R. Bishop, J. Druce, J. J. Kim, J. Kilner, H. L. Tuller, ECS Trans. 50 (2013) 35–38.

[110] J. Bae, B. C. H. Steele, Solid State Ionics 106 (1998) 247–253.

[111] M. De Ridder, A. G. J. Vervoort, R. G. Van Welzenis, H. H. Brongersma, Solid State Ionics 156 (2003) 255–262.

[112] P. J. Scanlon, R. A. M. Bink, F. P. F. van Berkel, G. M. Christie, L. J. van IJzendoorn, H. H. Brongersma, et al., Solid State Ionics 112 (1998) 123–130.

[113] J. Mizusaki, K. Amano, S. Yamauchi, K. Fuekl, Solid State Ionics 22 (1987) 323–330.

[114] J. Mizusaki, K. Amano, S. Yamauchi, K. Fuekl, Solid State Ionics 22 (1987) 313–322.

[115] J. Van Herle, A. J. McEvoy, Berichte Der Bunsengesellschaft Für Phys. Chemie. 97 (1993) 470–474.

[116] J. L. Hertz, Ph.D. Thesis, Massachusetts Institute of Technology, 2006.

[117] W. Weppner, R. A. Huggins, J. Electrochem. Soc. 124 (1977) 1569–1578.

[118] J. Maier, Solid State Ionics 135 (2000) 575–588.

[119] S. Park, Y. Shao, J. Liu, Y. Wang, Energy Environ. Sci. 5 (2012) 9331.

[120] N. S. Lewis, D. G. Nocera, Proc. Natl. Acad. Sci. 103 (2006) 15729–15735.

[121] M. W. Kanan, D. G. Nocera, Science 321 (2008) 1072–1075.

[122] J. E. Katz, T. R. Gingrich, E. A. Santori, N. S. Lewis, Energy Environ. Sci. 2 (2009) 103.

[123] Y. C. Lu, Z. Xu, H. A. Gasteiger, S. Chen, K. Hamad-Schifferli, Y. Shao-Horn, J. Am. Chem. Soc. 132 (2010) 12170–1.

[124] J. Suntivich, H. A. Gasteiger, N. Yabuuchi, H. Nakanishi, J. B. Goodenough, Y. Shao-Horn, Nat. Chem. 3 (2011) 546–50.

[125] L. Zhao, N. H. Perry, T. Daio, K. Sasaki, S. R. Bishop, Chem. Mater. 27 (2015) 3065–3070.

[126] A. Borgschulte, W. Lohstroh, R. J. Westerwaal, H. Schreuders, J. H. Rector, B. Dam, et al., J. Alloys Compd. 404-406 (2005) 699–705.

[127] B. Dam, R. Gremaud, C. Broedersz, R. Griessen, Scr. Mater. 56 (2007) 853–858.